REPUBLIQUE DU CAMEROUN
Paix-Travail-Patrie
****

UNIVERSITE DE YAOUNDE I

****

CENTRE DE RECHERCHE ET DE
FORMATION DOCTORALE EN SCIENCES,
TECHNOLOGIES ET GEOSCIENCES
****

UNITE DE RECHERCHE ET DE
FORMATION DOCTORALE EN PHYSIQUE
ET APPLICATIONS
****

B.P 812 Yaoundé
Email : crfd_stg@uy1.uninet.cm

REPUBLIC OF CAMEROON
Peace-Work-Fatherland
****

UNIVERSITY OF YAOUNDE I

****

POSTGRADUATE SCHOOL OF
SCIENCES, TECHNOLOGY AND
GEOSCIENCES
****

RESEARCH AND POSTGRADUATE
TRAINING UNIT FOR PHYSICS
AND APPLICATIONS
****

P.O. Box 812 Yaoundé
Email : crfd_stg@uy1.uninet.cm

FACULTY OF SCIENCE
FACULTE DES SCIENCES
DEPARTMENT OF PHYSICS
DEPARTEMENT DE PHYSIQUE
LABORATORY OF MECHANICS, MATERIALS AND STRUCTURE

LABORATOIRE DE MECANIQUE, MATERIAUX ET STRUCTURE

THEORETICAL AND EXPERIMENTAL STUDY OF THE OPTOELECTRONIC OSCILLATORS CASCADED BY NONLINEAR ELECTRONIC COMPONENTS.

Thesis submitted in partial fulfillment of the requirements for the award of the degree of Doctor of Philosophy (Ph.D.) in Physics,

Option: *Fundamental mechanics and complex systems*

By

MBOYO KOUAYEP René

Registration Number: **12U0472**

Master of Science in physics

Under the supervisions of

TALLA MBE Jimmi Hervé
Associate Professor, University of
Dschang (Cameroon)

WOAFO Paul
Professor, University of
Yaounde I (Cameroon)

Academic Year 2022/2023

University of Yaounde I

Faculty of Science

Department of Physics

THEORETICAL AND EXPERIMENTAL STUDY OF THE OPTOELECTRONIC OSCILLATORS CASCADED BY NONLINEAR ELECTRONIC COMPONENTS.

Submitted and defended in fulfillment of the requirements for the degree of Doctor of Philosophy / Ph.D in Physics

Option: Fundamental mechanics and complex systems

By
MBOYO KOUAYEP René
Registration number: **12U0472**
Master in physics

Supervisors,

Prof. TALLA MBE Jimmi Hervé
Associate Professor, University of Dschang (Cameroon)

Prof. WOAFO Paul
Professor, University of Yaoundé I (Cameroon)

Laboratory of Mechanics, Materials and Structure

kouayepmboyo@yahoo.fr

Academic Year 2022/2023

UNIVERSITÉ DE YAOUNDÉ I
THE UNIVERSITY OF YAOUNDE I

FACULTÉ DES SCIENCES
FACULTY OF SCIENCES

DÉPARTEMENT DE PHYSIQUE
DEPARTMENT OF PHYSICS
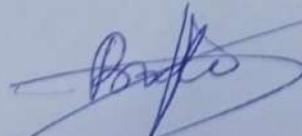
ATTESTATION DE CORRECTION DE LA THÈSE DE DOCTORAT/Ph.D

Nous, Professeur **BODO Bertrand** et Professeur **ESSIMBI ZOBO Bernard**, respectivement Examinateur et Président du jury de la Thèse de Doctorat/PhD de Monsieur **MBOYO KOUAYEP René**, Matricule 12U0472, préparée sous la direction des Professeurs **WOAFO Paul** (Université de Yaoundé 1) et **TALLA MBE Jimmi Hervé** (Université de Dschang), intitulée : « **Theoretical and experimental study of the optoelectronic oscillators cascaded by nonlinear electronic components** », soutenue le Vendredi, **22 Décembre 2023**, en vue de l'obtention du grade de Docteur/PhD en Physique, Spécialité **Mécanique, Matériaux et Structures,** option **Mécanique Fondamentale et Systèmes Complexes** attestons que toutes les corrections demandées par le jury de soutenance ont été effectuées.
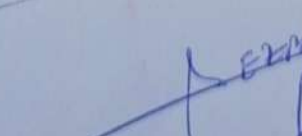
En foi de quoi, la présente attestation lui est délivrée pour servir et valoir ce que de droit.

Fait à Yaoundé, le **15 FEV 2024**

Examinateur   Le Président du jury   Le Chef de Département de Physique

Le Chef de
Département

Pr BODO Bertrand   Pr ESSIMBI ZOBO Bernard   Pr NDJAKA Jean-Marie

Dedication

This Work is dedicated to:

- My Lord God for all he has done for me so far and continues to do so.
- Especially to my mother **TCHAMOU Marie Thérèse.**

Acknowledgements

The research works during these years at the Department of Physics Faculty of science, University of Yaounde I was a scientific and human adventure very rich in emotions. It had its moments of joy, and excitement, but also its moments of hesitation and doubt.

The accomplishment of this thesis would not be possible without the assistance and the help of several people to, whom I would like to express my sincere gratitude and special my appreciation to:

♣ My supervisor Professor **WOAFO Paul**, Head of the Laboratory of Modelling and Simulation in Engineering, Biomimetics and Prototypes at the University of Yaounde I, for his great human qualities, his advice, and constant support during this research work through the regular seminars and training sessions that he organizes, as well as his great availability to discuss science in general. I cannot simply describe in a few lines all the good that I think of you, but I know that it has been a real pleasure and honor working with you.

♣ My supervisor Professor **TALLA MBE Jimmi Hervé**, for the motivating discussions and great time we had during my thesis and my dissertation. Despite huge academic and administrative duties at the University of Dschang, he always found time to discuss with me and answer my queries when the time arose. Thank you very much for everything, Doctor.

♣ The whole members of the **Jury** for having accepted to evaluate this work. Without you, this defense would not have taken place. Thank you very much.

♣ The **Postgraduate School** for having agreed to do examine this work through the experts and to authorise the public defence of this work.

♣ Professor **NDJAKA Jean Marie Bienvenu**, head of the Department of Physics at the Faculty of Science of the University of Yaoundé I, who contributed to my academic training through his teachings and advice.

♣ Professor **ESSIMBI ZOBO Bernard**, for reading this document, discussing it and giving advice on how to improve this work.

♣ Professor **SIFEU TAKOUGANG Kingni**, for his advice and discussions.

♣ Doctor **TALLA Alain Francis**, for his constant availability to discuss, his advice, and his sympathy since my Master thesis with the milestones of experiment that you have set in me. Always in a good mood, Doctor, I thank you sincerely.

♣ All the Teachers of the Department of Physics at the Faculty of Sciences of the University of Yaoundé I for the lectures and practical works during my academic training. Please accept my sincere gratitude.

♣ All the seniors, the Ph.D. students, and also the students of the Master cycle of the Laboratory for the edifying exchanges that we had and that allowed me to carry out this work; but also, especially for the climate of conviviality, the friendly atmosphere, and more. To all those who have not yet finished, I wish them good luck with the continuation of their work.

♣ Cameroon Physical Society (**CPS**) for organizing several scientific conferences in which I participated. It was an unforgettable experience that allowed me to discuss and learn about the scientific works of other research being done elsewhere.

♣ The different student Chapters of the University of Yaounde I, namely *the Institute of Electrical and Electronics Engineers* (**I.E.E.E**), **OPTICA**, and *Society of Photo-Optical Instrumentation Engineers* (**SPIE**) Student Chapters for their funding to the groups which enabled to carry out some projects and participate in several technological trainings. It helped me a lot to become familiar with electronic and optical components on a practical level.

♣ My Mother **TCHAMOU Marie Thérèse** for her moral and material support, her encouragement, and her advice but also and above all her prayers. I cannot find words to express my joy and my gratitude. Thank you for believing in me Mother.

♣ My other Mother **KAIMBA Adeline Emilda** for his blessings and prayers without which I would not be able to reach this level; I really don't know which words to use to express my thanks.

♣ All those from near and far who have participated in the completion and construction of this work and whose names have not been mentioned here, for their encouragement and advice.

Table of contents

v

Chapter 3 : Results and discussion

List of Figures

x

List of Tables

List of abbreviations

CNBPF: *Cubic Nonlinear Band Pass Filter.*

CN-OEO: *Cubic Nonlinear Optoelectronic Oscillator.*

CNT: *Cubic Nonlinear Terms.*

dB: *Decibel.*

DBR: *Distributed Bragg Reflector.*

DC: *Direct Current.*

DDE: *Delay Differential Equation.*

DFB: *Distributed Feedback.*

FSR: *Free Spectral Range.*

FORTRAN: *FORmula TRANslator*

LASER: *Light Amplification by Stimulated Emission of Radiation.*

LD: *Laser Diode.*

MFC: *Microwave Frequency Combs.*

MMO: *Mixed-Mode Oscillation.*

MZM: *Mach-Zehnder Modulator.*

ODE: *Ordinary Differential Equation.*

OEO: *Optoelectronic Oscillator.*

PD: *Photo Diode.*

RF: *Radio-Frequency.*

RK: *Runge Kutta.*

SRL: *Semiconductor Ring Laser.*

VCSEL: *Vertical Cavity Surface-Emitting Laser.*

Vdp: *Van Der Pol.*

Abstract

This thesis aims at the theoretical and experimental study of optoelectronic oscillators cascaded by nonlinear electronic components. For this purpose, two (02) nonlinear electronics components have been used, namely: the self-sustained Colpitts oscillator and the nonlinear filter. We first study numerically and experimentally the self-sustained Colpitts oscillator which generates an electrical signal at high frequency and exhibits dynamic behaviors such as periodic, bursting, and mixed-mode oscillations which can be obtained using a potentiometer contained in the electronic circuit of the oscillator. Subsequently, this Colpitts oscillator is inserted into the electronic part of the optoelectronic oscillator (*Colpitts-OEO*). In this way, we put forward the interaction between optical nonlinearity and electronic nonlinearity to obtain also complex dynamic behaviors of the system thus constituted. It is shown that a wide variety of periodic and chaotic states can be excited and that there is an amplification of the signal frequencies. The temporal dynamics of the *Colpitts-OEO* system with and without delay is studied experimentally. In addition, we make an analytical and numerical study of the optoelectronic oscillator cascaded by a nonlinear filter (*CN-OEO*). This nonlinear filter is designed from a non-linear capacitor and a coil. We thus provide a spectral analysis of the phenomena of multi-periodicity, crenelated, mixed-mode oscillations, and chaos when the bandwidth and the cubic nonlinear term of the filter vary in the *CN-OEO*. On the one hand, when the high and low cut-off frequencies are sufficiently far apart, it is both analytically and numerically proved that the presence of the cubic nonlinear term (*CNT*) reveals the frequency combs generation with a free spectral range equal to the inverse of the time delay. Likewise, the width of the central peak narrows with the increase of the *CNT*, showing that the system becomes more and more selective in terms of oscillation frequencies. On the other hand, when the cut-off frequencies are sufficiently close, harmonic and sub-harmonic frequencies are recorded. In either case, *CN-OEO* displays oscillations whose frequencies remain greater than those of a standard optoelectronic oscillator.

Keywords: Optoelectronic oscillator, Colpitts oscillator, nonlinear filter, time-delay system, bursting oscillation, mixed-mode oscillation, chaotic pulse-package, power spectrum, frequency combs.

Résumé

Cette thèse a pour objet l'étude théorique et expérimentale des oscillateurs optoélectroniques cascadés par des composants électroniques non linéaires. Pour cela, deux (02) composants électroniques non linéaire ont été utilisés à savoir : l'oscillateur auto-entretenu de Colpitts et le filtre non linéaire. Nous étudions tout d'abord numériquement et expérimentalement l'oscillateur auto-entretenu de Colpitts qui génère un signal électrique à haute fréquence et exhibe des comportements dynamiques tels que des oscillations périodiques, des oscillations de battements et des oscillations à modes mixtes qui peuvent être obtenues en utilisant un potentiomètre contenu dans le circuit électronique de l'oscillateur. Par la suite, cet oscillateur de Colpitts est inséré dans la partie électronique de l'oscillateur optoélectronique (*Colpitts-OEO*). Nous mettons ainsi en exergue, l'interaction entre la non linéarité optique et la non linéarité électronique afin d'obtenir d'autres comportements dynamiques complexes du système ainsi constitué. Il est montré qu'une grande variété des états périodiques et chaotiques peuvent être excités et aussi une amplification des fréquences du signal. La dynamique temporelle du système *Colpitts-OEO* avec et sans délai est étudiée expérimentalement. De plus nous faisons une étude analytique et numérique de l'oscillateur optoélectronique cascadé par un filtre non linéaire (*CN-OEO : cubic nonlinear OEO*). Ce filtre non linéaire est conçu à partir d'un condensateur non linéaire et d'une bobine. Nous fournissons ainsi une analyse spectrale des phénomènes de multi périodicité, des oscillations crénelées, des oscillations à modes mixtes et des oscillations chaotiques lorsque la largeur de la bande passante et le terme non linéaire cubique du filtre varient dans le *CN-OEO*. D'une part, lorsque les deux fréquences de coupure sont suffisamment éloignés, il est prouvé analytiquement et numériquement que la présence du terme non linéaire cubique révèle la génération des peignes de fréquences avec une plage spectrale libre égale à l'inverse de la valeur du délai. De même, la largeur du pic central se rétrécit avec l'augmentation du terme cubique non linéaire, montrant que le système devient de plus en plus sélectif en termes de fréquences d'oscillation. D'autre part, lorsque les fréquences de coupure sont suffisamment proches, les fréquences harmoniques et sous-harmoniques sont enregistrées. Dans les deux cas, le *CN-OEO* affiche des oscillations dont les fréquences restent supérieures à celles d'un oscillateur optoélectronique standard.

Mots-clés : Oscillateur optoélectronique, oscillateur de Colpitts, filtre non linéaire, système avec délai, oscillations de battements, oscillations à modes mixtes, paquets d'impulsion chaotiques, Spectre de puissance, peignes de fréquences.

General introduction

Electronics experienced a major boom at the end of the 19th century. Already in 1897, the Italian physicist Guglielmo Marconi invented the first form of the radio and obtained a patent. He also used "Antenna" for the transmission of radio waves. Thereafter Jagadish Chandra Bose also worked on radio, microwave optics, and wireless signaling. He was the first to use semiconductor junctions to detect radio signals in 1899 [1]-[3]. Thus, at the beginning of the 20th century, with the assembly of electronic components, circuits such as electronic oscillators, filters, amplifiers, and many others came into being. For example, in 1915 and 1918, the scientists Hartley and Colpitts invented patented and oscillators that bear their names respectively [4]-[5]. Colpitts and Hartley electronics oscillator became very popular both in industries and academia due to their simplicity, ease of operation, and superior stability. In early literature, these circuits were already referred to as Colpitts and Hartley oscillators [6] and were widely used in audio and communication applications [7]-[11]. This vast field that is electronics continues to this day to achieve remarkable achievements in terms of its applications in everyday life, which the world can no longer do without.

The progress of science imposes new choices and new strategies that are very different from those used in the past, such as the use of new systems or new techniques. In recent years, a great effort has been made to miniaturize devices for photonic applications based on the study of light-matter interaction [12]-[13]. Optics is therefore the science that studies light and its properties, its production, propagation and diffusion, its manipulation, and its applications. Nonlinear optics is the study of phenomena that occur as a consequence of the modification of the optical properties of a material system by the presence of light. In other words, it is the behavior of light in non-linear media and all-optical phenomena and systems described by non-linear equations [14]-[15]. It is all this that has led scientists working in this field to prophesy that optics will be in the 21st century what electronics was in the 20th century. This dream is becoming a reality with guided optics, which is now emerging as one of the most important technologies in the context of optical telecommunications, which is a revolution compared with telecommunications by radio waves [16]-[19].

The invention of the laser in 1960 by Theodore Maiman [20] and the discovery of the optical fiber four years later by Charles Kao and Georges Hockman [21], revolutionized the world of oscillators because it became possible to link optics and electronics: this is Optoelectronics which can in some circumstance incorporate time-delay.

Delay differential systems are ubiquitous since they are encountered in relevant fundamental and applied fields such as chemical kinetics, fluid dynamics, electronics, biology, optics and photonics, and so on [22]-[26]. Particularly in the optical domain, a wide variety of time-delayed electro-optical systems was modeled using the so-called Ikeda's equation [27]-[28]. Examples are optoelectronic oscillators (*OEOs*).

Optoelectronic oscillators (*OEOs*) were first proposed by Neyer and Voges in 1982 [27], but it was not until 1994 that Yao and Maleki of the *JPL* (*Jet Propulsion Laboratory*) first studied these oscillators for microwave generation [29]. The main advantage of *OEOs* compared to other oscillators is related to their time scales. The time scale versatility is possible because the system is built with ultra-fast optical and electronic devices, with bandwidths up to 100 GHz [30]. As a result, the nonlinear dynamics of *OEOs* can span several orders of magnitude, and over the past three decades, research on various *OEO* architectures has demonstrated that they can be particularly fruitful systems for both basic and applied science.

In general, in *OEOs*, the nonlinearity of the system comes from the optical path, while the electrical path is considered to be linear. *OEOs* are autonomous systems in which a signal is alternatively converted into the optical and electrical domains in a closed-loop configuration. In other words, *OEOs* offer the advantage of generating both electrical and optical signals for a more wide range of applications [31]-[33]. In their standard configuration, *OEOs* have two sub-families depending on the bandwidth of the electrical path in the feedback loop When the filter is narrow, the system displays ultra-stable microwave signals with applications in the fields such as aerospace engineering [34], sensing [35]-[36], time-frequency metrology [37]-[38], and pulse generation in optical fiber networks [39]-[40]. On the other hand, when the filter is broad, *OEOs* can output other complex optical microwave signals such as breathers, bursting, chaos [41]-[42] that are applied in optical chaos communications [22],[43], random bit generation [44]-[45], and neuromorphic computing [46]-[47]. These systems with delayed feedback have been the focus of intense research activities in recent years and were shown to be excellent platforms to investigate the interaction between the complexity induced by nonlinearity and the infinite dimensionality inherent to the time-delay [48]-[50].

From the discovery of frequency combs with the construction of the first mode-blocked laser [51], various configurations, including optoelectronic feedback [52], optical

injection [53], and optical feedback [54] have been developed and analyzed for the generation of microwave frequency combs (*MFCs*). It is important to clarify that *OEOs* were also used to display microwave frequency combs (*MFCs*) [55]-[56]. Microwave frequency combs (*MFCs*) [57]-[58] are spectral structures characterized by a discrete and regularly spaced succession of lines and found a multitude of applications in a wide range of fields such as metrology [59]-[60], modern instrumentation [61]-[62], spectroscopy [63], and radar [64], to name just a few.

In the architectures of *OEOs* used for most applications cited above, the nonlinear conversion between the electrical and the optical signals is performed by a phase or an intensity modulator with a sinusoidal transfer function. On the other hand, it was demonstrated that other electro-optic components can be used to achieve such nonlinear conversion [65]-[66]. These authors exploited the seeding laser diode (*LD*) itself as an electrical-to-optical converter through its power-intensity transfer function which offers an advantage in congestion. **For instance, such an idea was carried out with a Van der Pol oscillator in the electrical path Chaotic and limit-cycle oscillations were generated experimentally, but at frequencies up to some *kHz* imposed by the Van der Pol oscillator. Moreover, this Van Der Pol oscillator used is not an oscillator that generates complex electrical signals. It would be therefore interesting to explore the case of oscillation featuring complex signal such as the Colpitts oscillator.**

Among these novel architectures of *OEOs*, the one with the nonlinear capacitor and called the cubic-nonlinear *OEO* (*CN-OEO*) was investigated both theoretically and experimentally with and without the Mach-Zehnder modulator. **It came out that compared to a standard *OEO* (that is the one with a standard band-pass filter in the electrical path), the *CN-OEO* can display chaos for lower feedback gain. Moreover, it routes to chaos through a large region of limit-cycle oscillations of higher frequencies followed by a narrow window of crenelated oscillations instead of breathers as is usually the case [67]-[69]. However, the power spectrum analysis of the system was not addressed as well as a study according to the width of the bandwidth. Power spectrum analysis is one of the main tools to explore the characteristics of oscillation properties of *CN-OEO*, notably when some parameters evolve such as the bandwidth of the electrical filter and the characteristic parameter of the nonlinear capacitor. It is in this perspective that we have set ourselves another objective of this thesis to study numerically and experimentally the dynamics and the spectrum of *OEOs* cascaded by nonlinear electronic components.**

3

This thesis is divided into three chapters:

In chapter 1, we will review the literature on the progress of work on optoelectronic oscillators. In this chapter, we will introduce the basics necessary for a good understanding of this field, while also highlighting the problem of the thesis.

Chapter 2 will be devoted to the methodology. We will explain the mathematical techniques used to describe the nonlinear and *OEO* circuits used in this thesis as well as the numerical analysis methods to solve the differential equations. The optical and electronic materials used in the experiments will also be presented.

In chapter 3, we present the obtained results. This chapter is divided into two parts. First, we make a numerical and experimental study of the dynamics of the Colpitts oscillator. The quantities characterizing it such as its amplitude, its period, and its waveform are examined. This study shows a perfect agreement between the numerical part and the experimental part. Then it is a question of making an experimental study of the dynamics of the *Colpitts-OEO* system with and without delay. In the second part, we study the power spectrum analysis of time-delayed optoelectronic oscillators with wide and narrow nonlinear filters. We are thus interested in two parameters of the system, namely: the effects of the coil and the *CNT*. For this, a study of the dynamics and the frequency of *CN-OEO* are carried out. The case where $L=10\,\mu H$ and $L=10\,mH$ corresponding to the wide and narrow band of the nonlinear filter are considered.

We will end our work with a general conclusion and perspectives, in which we will summarize the results and indicate new interesting problems identified at the end of this thesis.

Chapter 1

Literature review

1.1 Introduction

Oscillators are an integral part of our lives and are increasingly used in fields such as telecommunications, computing, and embedded systems, especially in aeronautics and space. These are essential elements at the level of transmitters and receivers for the transmission and suitable restitution of information. The world of oscillators has been turned upside down with the discovery of laser and fiber optics with the advent of a new oscillator called optoelectronic oscillators (*OEOs*). *OEOs* are systems that open up a wide advantage with the generation of electrical and/or optical signals and become an excellent means for the generation of high-purity radio frequency and microwave signals in the civil and military fields. In this chapter, it is a question for us of making a review of the literature on oscillators and optoelectronic oscillators in particular in order to better understand the necessary bases as well as the possibilities of studies and applications for the good understanding of this field and to identify the problem of this thesis.

1.2 The oscillators

1.2.1 Description

In general, an oscillator is a system that moves back and forth more or less long and more or less stable around an equilibrium position. In other words, the constituted system produces oscillations that can be periodic or not. To produce these oscillations, the oscillators need a source of energy that is either internal or external to the system: we then speak of self-sustaining oscillators or forced oscillators, respectively.

The oscillation frequency is fixed by the external excitation in the case of the forced oscillators. With regard to the self-sustaining oscillators; the oscillator itself has a source of internal energy necessary to maintain its own oscillations appearing in the form of a looped system or of feedback. In their configuration, self-sustaining oscillators are made up of two main media, namely a resonant milieu which makes it possible to select the oscillation frequencies, and an amplifying milieu which compensates the losses of the resonator to maintain oscillations. This configuration is given in **figure 1.1**.
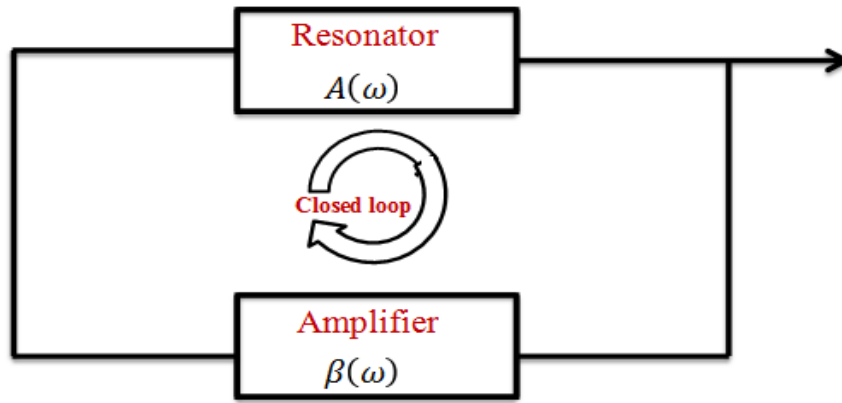
Figure 1.1: Configuration of a self-sustaining oscillator.

In the Fourier domain, if we consider $\mathrm{A}(\omega)$ as the transfer function of the resonator and $\beta(\omega)$ as that of the amplitude, the transfer function of the oscillator $H(\omega)$ will be defined by the relation:

$$H(\omega) = \frac{\mathrm{A}(\omega)}{1 + \mathrm{A}(\omega)\beta(\omega)} \tag{1.1}$$

The conditions of instabilities which are the limiting conditions of starting of oscillations of Barkhausen are defined by the system of equations:

$$\begin{cases} |\mathrm{A}(\omega)\beta(\omega)| = 1 \\ \arg\left[\mathrm{A}(\omega)\right] + \arg\left[\beta(\omega)\right] = 2k\pi \end{cases} \tag{1.2}$$

where k is an integer. The first equation of the system is the condition on the oscillation amplitude and the second equation is the phase condition. The system will only oscillate when the transfer function of **equation (1.1)** is infinite, i.e. when the denominator is equal to zero.

1.2.2 Colpitts oscillator

a) History, definition, and circuit

The Colpitts oscillator invented by the American engineer Edwin Colpitts in 1918 is one of the many possible configurations of an electronic oscillator [70]. Its strengths lie in its simple construction and robustness. This oscillator is an amplifier with positive feedback and it converts the *DC* input signal into an *AC* output waveform with a certain variable frequency

drive and certain shape of output waveform by using the positive feedback instead of the input signal.

Oscillators that utilize the inductor L and capacitor C in their circuit are called LC oscillators which is a type of linear oscillator. The Colpitts oscillator consists of a tank circuit which is an LC resonance sub-circuit made of two series capacitors connected in parallel to an inductor and the frequency of oscillations can be determined by using the values of these capacitors and inductor of the tank circuit [71]. The Colpitts oscillator is one of the well-known and most commonly used electronic oscillators for generating sinusoidal waves at radio frequencies [72]. However, this oscillator is shown to exhibit chaos for some special sets of its parameters [73]-[75]. Compared to its low-frequency counterparts (e.g. Chua's circuit [76]), the Colpitts oscillator presents some interesting features:

❖The operation frequency can vary from a few Hertz up to the microwave region;

❖The relative simplicity of its electronic circuit;

❖The oscillator can exhibit rich and complex (chaotic) dynamical behavior at various operating frequencies.

These attractive properties justify the potential utility of the Colpitts oscillator for chaos-based secure communication applications [77]. **Figure 1.2** shows a typical Colpitts oscillator with a tank circuit. An inductor L is connected parallel to the serial combination of capacitors C_1 and C_2 (shown by the red enclosure). The process starts with the charging of two capacitors C_1 and C_2. Then inside the tank circuit, these two series capacitors discharge into the parallel inductor L and the stored energy in the capacitor is transferred to the inductor. Due to the capacitor being connected in parallel, the inductor is now discharged by the two capacitors and the capacitors start to charge again. These charging and discharging in both of the components continues and thus provide an oscillation signal across it.

The oscillation is highly dependent on the capacitors and the inductor's value. The below formula is to determine the oscillation frequency:

$$f = \frac{1}{2\pi\sqrt{LC}}$$
(1.3)

where f is the frequency and L is inductor, C is the total equivalent capacitance. The equivalent capacitance of the two capacitors can be determined using

$$C = \frac{C_1 \times C_2}{C_1 + C_2} \qquad (1.4)$$

So the oscillation frequency is finally given by:

$$f = \frac{1}{2\pi} \sqrt{\frac{C_1 \times C_2}{C_1 + C_2}} \qquad (1.5)$$

During this oscillation phase in the tank circuit, some energy loss occur. To compensate for this lost energy and to sustain the oscillation inside the tank circuit, a gain device is required. There are many different types of gain devices are used to compensate for the loss of energy inside the tank circuit. The most common gain devices are transistors and operational amplifiers.

The oscillation of the transistor-based Colpitts oscillator circuit is depended on the phase shift. This is well known as the Barkhausen criterion for the oscillator. As per the Barkhausen Criterion, the loop gain should be slightly greater than the unity and the phase shift around the loop needs to be 360 degrees or 0 degrees. So, during this case, to provide the oscillation across the output, the total circuit needs 0 degrees or a 360-degree phase shift. The transistor configuration as a common emitter provides a 180-degree phase shift whereas the tank circuit also contributes an additional 180-degree phase shift. By combining these two-phase shifts the total circuitry achieves a 360-degree phase shift which is responsible for the oscillation.
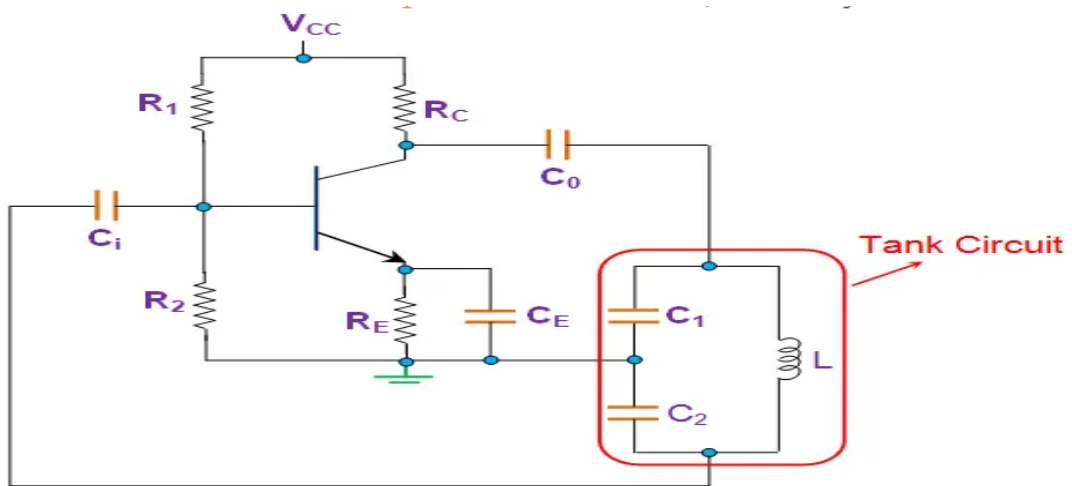
Figure 1.2: Colpitts oscillator circuit [71].

Other components in the circuit of **figure 1.2** are the same as that found in the case of common-emitter CE, which is biased using a voltage divider network, i.e., R_C is the collector

resistor, R_E is the emitter resistor which is used to stabilize the circuit, and the resistors R_1 and R_2 form the voltage divider bias network.

Here, as the power supply is switched ON, the transistor starts to conduct, increasing the collector current Ic due to which the capacitors C_1 and C_2 get charged. On acquiring the maximum charge feasible, they start to discharge via the inductor L.

b) Some application of the Colpitts oscillator circuit

The Colpitts oscillator has much more to offer in electronics and therefore has many applications, but we can mention among others [73,78]:

❖Due to the difficulties in a smooth variation of inductor and capacitor, the Colpitts oscillator is mainly used for fixed frequency generation.

❖The main use of the Colpitts oscillator is in mobile or other radio frequency-controlled communications devices.

❖In high-frequency oscillation, the Colpitts oscillator is an excellent choice. Thus high-frequency oscillator-based devices use Colpitts oscillator.

❖For those applications which need a wide range of frequencies with minimum noise-induced.

❖Various types of metal detectors use the Colpitts oscillator.

❖Frequency modulation related radio frequency transmitter use Colpitts oscillator.

❖In microwave applications, signal masking related chaotic circuits also required Colpitts oscillator in the different frequency range. To name just a few.

1.3 Nonlinear capacitor

Nonlinear capacitors are important components in electronic systems, from both the fundamental and technological points of view. They are used in circuits for power electronics and can operate at high frequencies. They can also be used to implement nonlinear resistors and inductances. For these reasons, they are commonly used as a source of nonlinearity in several physical systems [79]-[80].

In general, a nonlinear capacitor can be made of an ideal operational amplifier, four diodes, two linear capacitors, and one linear resistor as depicted in **figure 1.3.** The charge-voltage characteristics of the nonlinear capacitor is a nonlinear function of the instantaneous electrical charge and which can be modeled by a constitutive relation of the form [81,82]:

$$V_C(q) = \frac{q}{C_1} + 2V_0 Sinh^{-1}\left(-\frac{q}{2I_0 R_1 C_2}\right) \tag{1.6}$$

where V_0 and I_0 are the characteristics voltage and current, respectively.

A two terms Taylor expansion of *sinh* function gives:

$$V_C(q) = \left[\frac{1}{C_1} - \frac{V_0}{I_0 R_1 C_2}\right]q + \frac{V_0}{24(I_0 R_1 C_2)^3}q^3 \tag{1.7}$$

Using Maple software, this equation will be plotted in the next chapter.
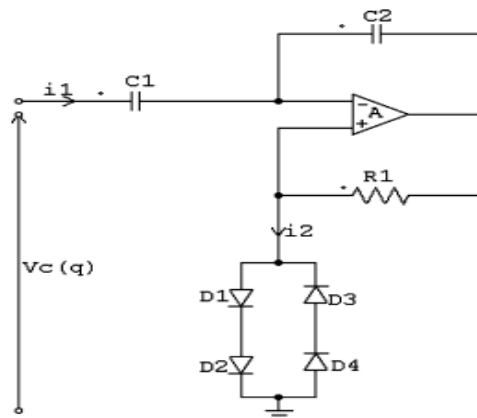
Figure 1.3: Model of the nonlinear capacitor.

1.4 The laser

1.4.1 History and definition

Devices generate visible or invisible light, based on the stimulated emission of light. The word laser stands for Light Amplification by Stimulated Emission of Radiation. The principle of stimulated emission (or induced emission) was described in 1917 by Albert Einstein. In 1950, Alfred Kastler proposed an optical pumping process, which he validated experimentally two years later with Brossel and Winter. Charles Townes and Arthur Schawlow established the principle of laser design in 1958, but it was not until two years later

that the American Theodore Maiman (1927-2007) developed the first laser [20]. The laser is an optical cavity where the photons are emitted by stimulated emission based on population inversion (is the process of achieving a greater population of higher energy state as compared to the lower energy state. The population inversion technique is mainly used for light amplification. It is required for laser operation). The laser is thus made up of an amplifier milieu, a resonant cavity, and reflection mirrors (see **figure 1.4**).
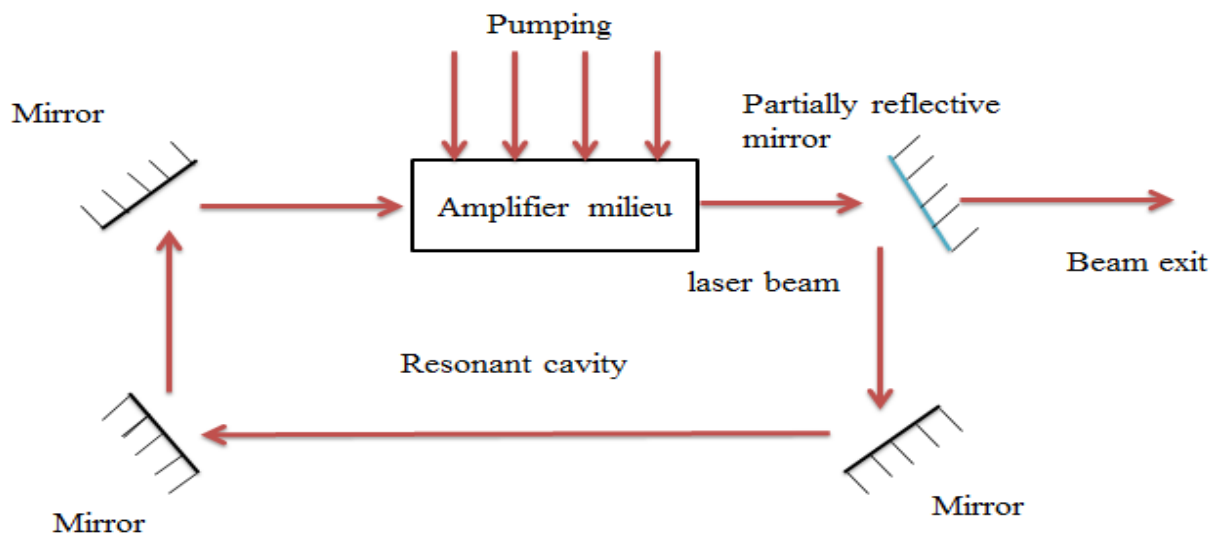
Figure 1.4: Schematic view of a laser.

Laser light has four unique characteristics that differentiate it from ordinary light these are coherence, directionality, monochromatic and high intensity.

1.4.2 Different types of Laser

There are several types of lasers, we can mention among others gas laser (is a laser in which an electric current is discharged through gas inside the laser medium to produce laser light. In gas lasers, the laser medium is in the gaseous state.), and a liquid laser (is a laser that uses the liquid as laser medium), solid-state lasers (is a laser that uses solid as a laser medium. In these lasers, glass or crystalline materials are used), and semiconductor lasers (is the one that interests us in this work).

a) Semiconductor lasers

Semiconductor lasers play an important role in our everyday life. These lasers are very cheap, compact in size, consume low power, and cover a wide spectral range from visible to near-infrared. Semiconductor lasers are also known as laser diodes and have an optical power

of up to several watts continuously. It is different from the solid-state laser. For example, in solid-state lasers, light energy is used as the pump source whereas, in semiconductor lasers, electrical energy is used as the pump source. In semiconductor lasers, a p-n junction of a semi-conductor diode forms the active medium or laser medium. The optical gain is produced within the semiconductor material.

There are several varieties of laser diodes on the laser market, depending on their very different applications.

i) Fabry-Perot cavity laser diodes

These are semiconductor lasers consisting of a resonant cavity delimited by two semi-reflecting plane mirrors inside which there is an active material at the p-n junction (see **figure 1.5**). The electrical pumping of the conduction zone is carried out by metallic contacts in order to carry out the amplification. It is important to note that this type of laser is not optimal for the majority of applications in optical telecommunications systems because of their spectral characteristic which reveals a low SMSR (Single-Mode Suppression Ratio) due to the high number of longitudinal modes.
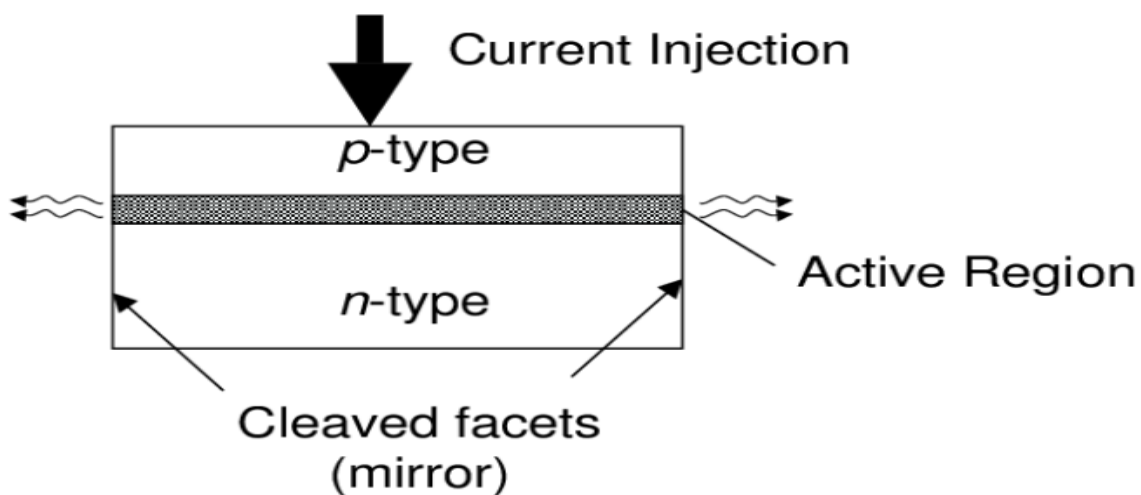
Figure 1.5: Structure of a semiconductor laser with a Fabry-Perot cavity [83].

ii) VCSEL laser diodes

Vertical-Cavity Surface-Emitting, are surface-emitting semiconductor lasers and their optical cavity is formed by Bragg reflectors or mirrors consisting of alternating layers of media of different refractive indices on either side of the p-n junction. Generally, the output

light is in a geometrically circular mode, thus facilitating its coupling with an optical fiber. Certain works show on the one hand that the *VCSELs*, when they are subjected to a sinusoidal modulated current emit pulses and/or packets of pulses of modulated frequencies which can reach a few hundred *MHz* and, on the other hand, excite relaxation oscillations in SRLs (Semiconductors Ring laser) [84].

VCSELs include the following:

❖**Bragg reflector lasers or *DBR*** (Distributed Bragg Reflector): are laser diodes consisting of a cavity in which one side is replaced by a Bragg mirror. The Bragg reflector is a periodic structure whose reflection coefficient depends on the wavelength of the incident photon. *DBRs* are widely used for the transmission of information over optical fibers in optical telecommunications, radar, and embedded systems applications.

❖**Distributed feedback lasers or *DFB***: have a structure similar to *DBRs* and are generally used in the field of fiber optical telecommunications. They are longitudinal single-mode and can emit at the wavelength of 1550 nm at which the optical fiber has minimum attenuation.

DFB and DBR lasers oscillate in a single-longitudinal mode even under high-speed modulation, in contrast to Fabry-Perot lasers, which exhibit multiple-longitudinal mode oscillation when pulsed rapidly [85]. The structure of DBF and DBR is given in **figure 1.6**.
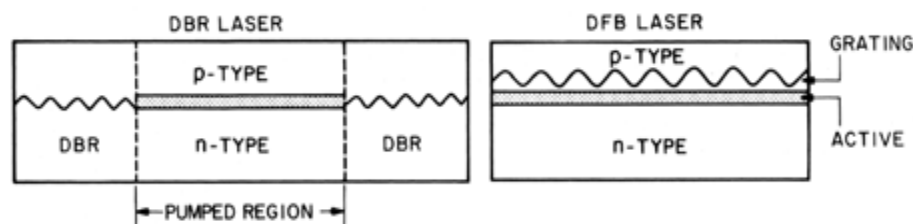
Figure 1.6: Schematic illustration of DBR and DFB lasers [86]

1.4.3 Current-power characteristics of a laser diode.

The optical power output of a laser diode depends on the current injected into the laser. If P_{op} is the photon power at the laser output, I is the pump current and I_{th} is the laser threshold current, then the photon output power will be given by the expression [87,88]:

$$\begin{cases} P_{op} = \alpha'I & \text{if} \quad (I \le I_{th}) \\ P_{op} = \alpha(I - I_{th}) & \text{if} \quad (I \succ I_{th}) \end{cases} \qquad (1.8)$$

where $\alpha = \eta h \nu$ is the directing coefficient of the $P_{op} = f(I)$ curve which depends on the differential Bragg mirror quantum yield η, h is Planck's constant and ν is the photon emission frequency. The parameter $\alpha' = \eta \eta_s \beta h \nu$ is a coefficient that depends on the efficiency and the factor of the spontaneous emission η_s and β respectively (which are negligible). The optical power is assumed to be zero for a pump current below the threshold current ($I < I_{th}$ at $P_{op} = 0$). The current-power characteristic of a laser is given by the following **figure 1.7**:
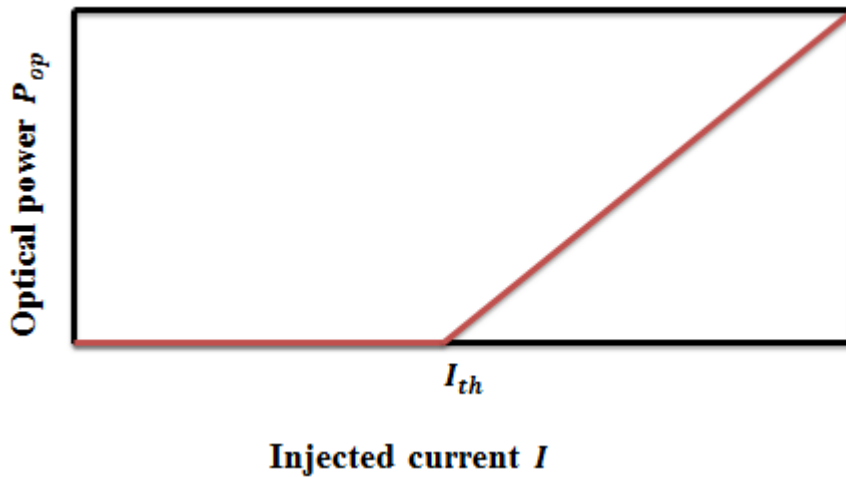
Figure 1.7: Current-power characteristics of a laser diode.

This figure reflects a so-called kink non-linearity existing in the laser medium. This kink non-linearity can therefore be translated by the non-linear function:

$$P_{op} = \mu D (I - I_{th}) \qquad (1.9)$$

where μ is a laser conversion factor, D the non-linear function of the laser defined by the relation :

$$D(x) = \begin{cases} 0 & \text{if} \quad (x \le 0) \\ x & \text{if} \quad (x > 0) \end{cases} \qquad (1.10)$$

For $I < I_{th}$, the laser is off, no photons are emitted. For $I \geq I_{th}$, we have the laser effect which emits a coherent monochromatic beam.

1.4.4 Applications of Lasers

A laser is an optical device that generates an intense beam of coherent monochromatic light by stimulated emission of radiation. Laser light is different from ordinary light. It has various unique properties such as coherence, monochromaticity, directionality, and high intensity. Because of these unique properties, lasers are used in various applications. The most significant applications of lasers include:

❖**Medicine:** Bloodless surgery, cancer diagnosis, and therapy remove tumors successfully, cosmetic treatments such as acne treatment, cellulite and hair removal…

❖**Communications:** Laser light is used in optical fiber communications to send information over large distances with low loss, in underwater communication networks, in space communication, radars, and satellites.

❖**Industries:** In electronic industries for trimming the components of Integrated Circuits (ICs), to collect information about the prefixed prices of various products in shops and business establishments from the bar code printed on the product…

❖**Science and technology:** In computers to retrieve stored information from a Compact Disc (*CD*), and also to store a large amount of information or data in *CD-ROM*, in computer printers…

❖**Military:** To determine the distance to an object, as secretive illuminators for reconnaissance during the night with high precision…

1.5 Electro-optical modulation (Mach-Zehnder Modulator)

Electro-optical modulators are based on the non-linear electro-optical effect which corresponds to the variation of the refractive index of the material by application of a voltage: this is the Pockels effect.

The Mach-Zehnder modulator is the most widely used electro-optical modulator. It is made of lithium niobate (*LiNbO₃*) and is based on an architecture composed of two "Y" junctions linked together by two straight guides which constitute the interferometer arms. The light propagating in the optical guides is generated by a laser source.

The *MZM* has two (02) separate electrodes, namely the bias or DC electrode (constant) used to select the operating point of the modulator and the RF electrode (variable) for wave modulation (see **figure 1.8.(a)**). It is characterized by its static transfer function giving the optical power output P_{out} as a function of the voltage $V(t)$ applied to the electrodes. Thus, if P_{in} represents the optical power of the laser beam at the input of the *MZ* modulator, the relationship between the output power and the applied voltage is a sinusoidal function given by [105],[109]:

$$P_{out} = P_{in} \cos^2 \left[\frac{\pi}{2} \frac{V(t)}{V_{\pi RF}} + \frac{\pi V_B}{2 V_{\pi DC}} \right] \tag{1.11}$$

V_B is the DC voltage applied to the bias and $V_{\pi DC}$ is the half-wave voltage at this electrode. The parameter $V_{\pi RF}$ is the half-wave voltage of the RF electrode which imposes a phase shift of π. For this phase shift of π, the optical power output reaches its maximum. This defines the operating point of an optoelectronic oscillator when the *MZ* modulator is used. The position of the half-wave and quarter-wave voltages giving the non-linearity of the *MZ* is shown in **Figure 1.8.(b)** [89].
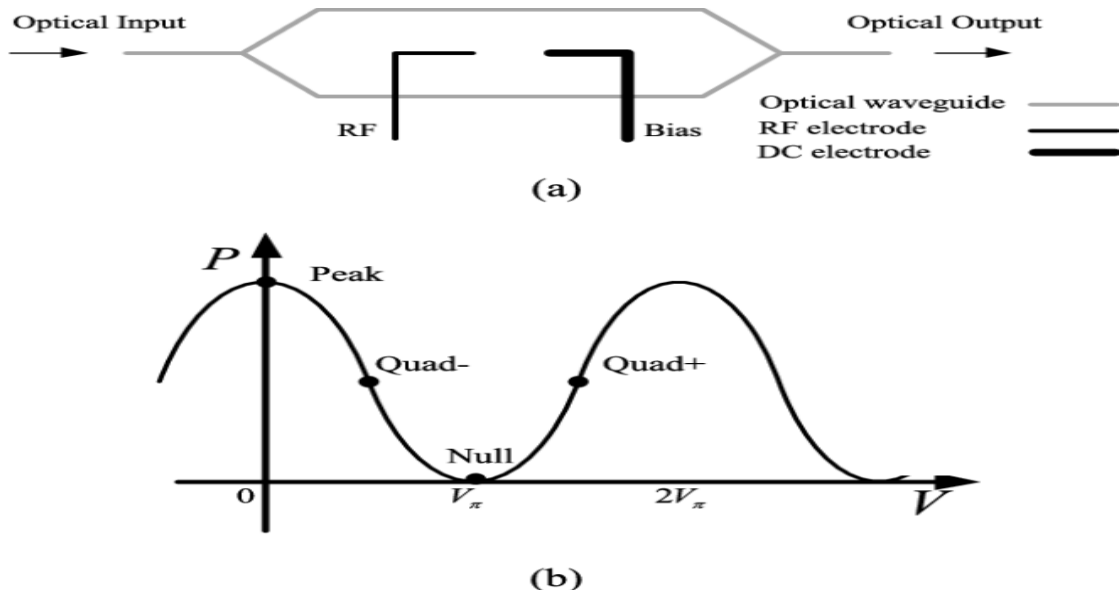
Figure 1.8: (a) Schematic of push-pull-type MZM and (b) the power transfer function curve [89].

In general, intensity modulators are characterized by:

❖**Bandwidth of the modulator**: this is very important as it limits the throughput in digital communications. It also depends on the type of modulator used and varies from one electrode to another.

❖**The half-wave voltage** V_π**:** this voltage makes it possible to pass from a maximum to a minimum transmission (or vice versa). This corresponds to a phase shift of π between the two arms of the *MZ* interferometer.

❖**The voltage** V_{bias} : also called the operating point of the modulator, it is chosen according to the applications of the envisaged modulator. To double the signal frquency, is sufficient to modulate with an operating point located in phase or phase opposition. To modulate a signal, however, it is often preferable to place the operating point in phase quadrature, i.e. the operating point must be in the middle of the linear zone of the transfer function.

❖**Insertion loss** α : this is the ratio of the light power injected at the input to that recovered at the output of the modulator. It corresponds to the capacity of the modulator to transmit light when it is in constructive interference.

❖**The contrast or extinction ratio**: generally induced during the manufacture of the modulator, it represents the ratio between the optical power transmitted at the output of the interferometer in the blocking state (destructive interference) and the interferometer in the passing state (constructive interference). This extinction ratio can be degraded if the two arms of the *MZ* interferometer are not strictly identical (loss imbalance).

The *MZ* modulator has a great advantage in that it can support high optical power and also responds to frequencies above 100 GHz making it an excellent candidate for fiber optical communication [90].

1.6 Modulation by electrical signals

In optical transmission systems, it is important to be able to modulate the light wave by an electrical signal and to be able to demodulate it afterward, supporting very high data rates in the case of digital telecommunications and very high microwave frequencies in the case of analog telecommunications. Thus, we can have intensity modulation, phase

modulation, and frequency modulation. Light intensity modulation offers the advantage of the simplicity of direct detection and is still the most widely used type of modulation. A distinction is made between two types of laser modulation: direct modulation and external modulation. These two modulation techniques are applied in our work.

1.6.1 Directly modulated laser diodes

Direct modulation of a laser source is the simplest method of modulation. This is achieved by superimposing an RF (or microwave) signal on the laser injection current (see **Figure 1.9**). Only semiconductor lasers are of practical interest for direct modulation because of bandwidth and efficiency requirements [91]. The unique feature of the semiconductor laser allows the semiconductor to be modulated directly by modulating its excitation current. At high data rates (10 Gb/s) or higher, the spurious frequencies imposed by direct modulation become relatively large, and this makes the modulation of semiconductor lasers inefficient. When these spurious signals are caused by modulation, the wave propagation speed fluctuates and the shape of the optical signal is distorted as it propagates through the fiber, making long-distance transmission inefficient [92].
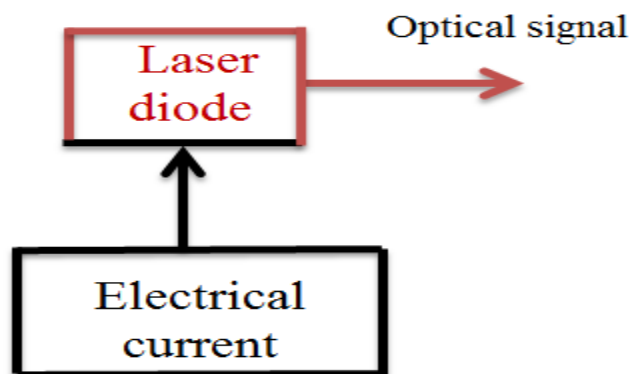
Figure 1.9: Modulation through the laser diode.

1.6.2 External modulators

A typical example of direct intensity modulation is an optical modulation in which data are modulated by varying the intensity of a laser beam. However, this type of modulation is not suitable for long-distance transmission since the power at which the transmitter's laser emits should be kept at a low level, its necessary to use an optical amplifier or repeaters which significantly increase the overall cost of the network solution. For more sophisticated modulations are used devices called external optical modulators [93]-[95].

There are two main categories of external modulation: electro-optical modulators (the one used in this thesis) and electro-absorbent modulators. This classification is based on the properties of the materials used to modulate the light intensity. Several important characteristics must be taken into account when comparing different modulators, namely: the voltage required for phase shifting, the optical processing capability, the linearity of the transfer function, etc.

The modulator has two inputs, one electrical and one optical (see **Figure 1.10**). An optical modulator is a device that produces temporal changes in the amplitude and phase of the optical signal. Several methods of optical modulation exist [96]. Amplitude modulation can be achieved with external modulators by constructing an interferometer in which it is possible to control the phase difference between the two arms by applying a controlled external electrical voltage (using electrodes) to an electro-optical material; this causes the refractive index of a single arm to change, thus producing phase modulation on the first arm of the modulator and amplitude modulation on the output of the interferometer. This type of device is known as a Mach-Zehnder (see **section 1.5**) and allows modulation frequencies over 40 GHz.
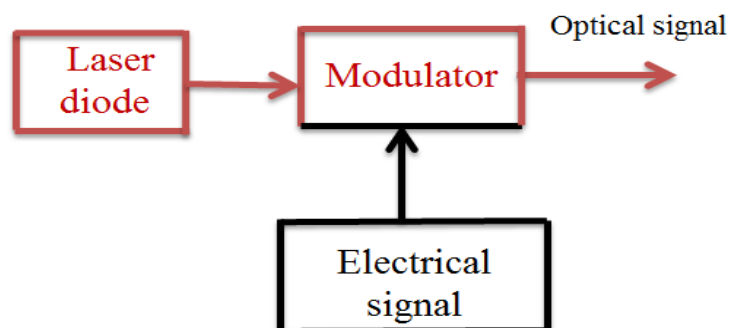
Figure 1.10: Optical link with external modulation.

1.7 Optoelectronic oscillator

1.7.1 Description

Optoelectronic oscillators (*OEOs*) are self-contained systems where the signal is alternately converted in the optical and electrical domains, in a closed-loop configuration (**figure 1.11**). The feedback consists of an electronic part that loops over the optical part. This is the seat of the optical/electrical conversion.

Energy carried by the optical signal

| Conversion Electrical/Optical | **Delay** | Conversion Optical/Electrical |

Energy carried by the electrical signal
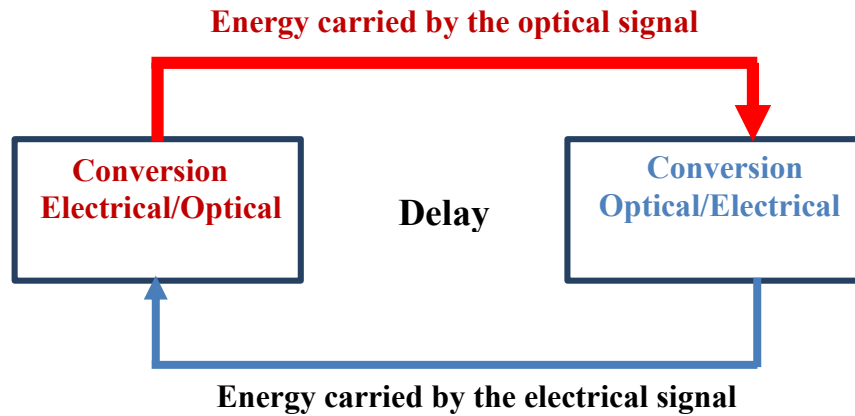
Figure 1.11: Generic representation of an optoelectronic oscillator with time-delayed feedback.

Energy flows alternatively in the optical and electrical forms, and conversion between both paths is performed by electrical-to-optical (*E/O*) and optical-to-electrical (*O/E*) converters. This closed-loop system is always nonlinear, dissipative, and infinite dimensional because of the time delay. The interplay between these three properties is the main source of dynamical complexity in *OEOs*. For metrological applications, a fourth property, stochasticity, becomes relevant as well [97].

1.7.2 Classical optoelectronic oscillator

Optoelectronics oscillators (*OEOs*) are autonomous nonlinear systems whose feedback loop is constituted by an optical and an electrical branch. In their architecture in general, the optical part of *OEOs* are seeded with a continuous-wave (*CW*) semiconductor laser (typically in the near-infrared range). The output laser beam is generally modulated using a nonlinear electro-optic modulator and subsequently launched into an optical fiber line which is long enough to induce a significant time delay. The optical beam is then converted into an electrical signal using a fast photodiode (*PD*). This radio-frequency (*RF*) signal is eventually band pass or low pass filtered, amplified, and then used as a driving signal of the modulator, thereby closing the feedback loop as shown in **figure 1.12**. Following this mechanism, *OEOs* can output *RF* signals with a frequency range from 1 *kHz* to 100 *GHz*, and they display a very wide range of complex dynamical behaviors [98]-[100],[131].

The purity of the microwaves generated with the OEO is since in the oscillation loop the insertion of a fiber delay line allows a considerable storage time equivalent to a quality factor given by the expression:

$$Q_{RF} = 2\pi F T_D \qquad (1.12)$$

where F is the microwave frequency and $T_D = \dfrac{nL}{C}$ is the delay induced by the delay line of

length L, where n is the refractive index of the group velocity, and C is the speed of light in a

vacuum.
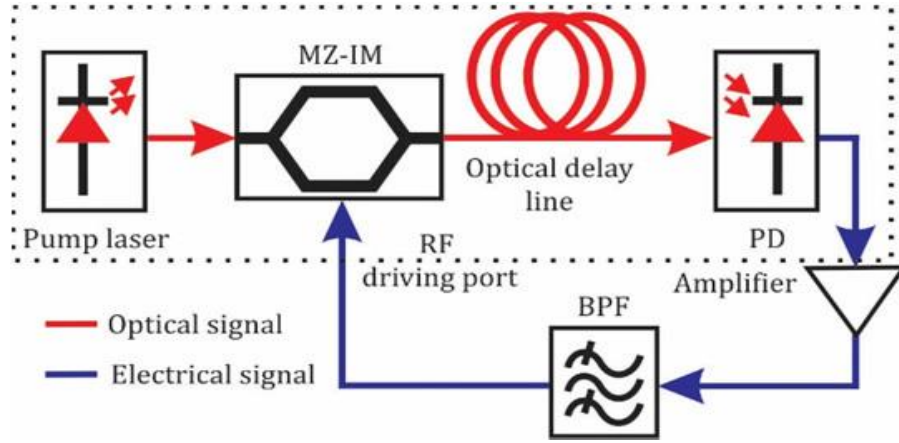
Figure 1.12: A classical Optoelectronic oscillator [101].

This system is described by an Ikeda-type delay integro-differential equation [102]:

$$x + \tau \frac{dx}{dt} + \frac{1}{\theta} \int_{t_0}^{t} x(s)\,ds = \beta \cos^2\left[x(t - T_D) + \phi \right] \qquad (1.13)$$

where β is the normalized gain which is proportional to the laser power, ϕ is the phase

corresponding to the half-wave bias voltage, and $x(t)$ is the normalized voltage through the

circuit. The delay introduced into the loop increases the dimensions of the system and these

two frequencies are inversely proportional to the respective time scales τ and θ. This allows

for three different time scales. By varying the loop gain β, the interaction between the band

pass filter and the optical non-linearity induces the coexistence of periodic slow dynamics and

chaotic fast dynamics [103]. This double dynamics is described by the breathers that are

periodic for small values of the gain; when the gain is large, these breathers become chaotic.

In 2009, Peil *et al*. in "Routes to chaos and multiple time scale dynamics in broadband

bandpass nonlinear delay electro-optic oscillators" explored the multi-scale dynamics in

broadband electro-optical oscillators. They consider a 20 m optical fiber that creates a 100 *ns*

21

delay. The other two time scales were related to the high and low cut-off frequencies of the filter used. Depending on the operating point ϕ and the loop gain, a wide variety of dynamic behaviors such as slow or fast oscillations with different waveforms, and regular or chaotic breathers [104,105].

It has been shown by considering the interaction between the Mach-Zehnder non-linearity and the optical delay that the ultra-pure microwave envelope amplitude becomes unstable as the loop gain increases [106]-[108].

1.7.3 The simplest autonomous optoelectronic oscillator looped by a laser

Goune Chengui in his thesis has shown that it is possible to design a simpler *OEO* than the classical ones [109]. Unlike other *OEOs*, this simplified *OEO* does not use an external modulator (see **figure 1.13**). But a simple electrical signal can be used to pump a laser which will provide oscillations. With this architecture, the intensity modulation is ensured by a piecewise linear function (and therefore, non-linear), through the power-intensity transfer function of the laser diode. The photodiode converts the input power $P(t)$ into an electrical voltage $V(t)$, which is applied to a variable voltage attenuator which here acts as an RF-amplifier with a gain G, before being converted back into the current, $I_{rf}(t)$ to be used to pump the laser diode. The laser diode performs the conversion from the electrical to the optical domain [109].
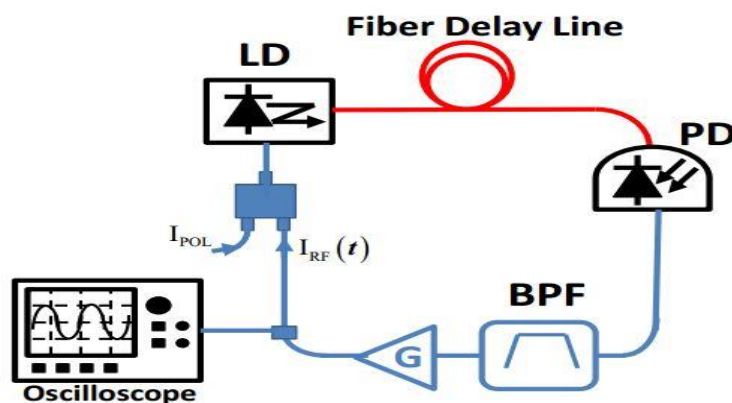
Figure 1.13: Basic architecture of an optoelectronic oscillator [109].

The dimensionless non-linear transfer function of the laser diode is, therefore:

$$D(x) = xH(x) = \begin{cases} 0 & \text{if} & (x \leq 0) \\ x & \text{if} & (x > 0) \end{cases} \tag{1.14}$$

where $H(x)$ is the Heaviside function usually equal to 0 for $x < 0$ and 1 otherwise.

Consequently, the non-linear function of the diode $D(x)$ is equal to zero for negative x, and is equal to x in the contrary case (with a linear evolution). In laser diodes, this function is of the form $\mu D(I - I_{th})$, which is equal to 0 for $I < I_{th}$, and to $\mu(I - I_{th})$ for $I \geq I_{th}$, with μ being the linear conversion factor from intensity to power. The intensity power of the transfer function of the laser diode is, therefore:

$$P(t) = \mu D\left[I_{rf}(t) + I_{pol} - I_{th} \right] \tag{1.15}$$

where $\mu = \eta_d h v$ is the conversion slope of the laser, η_d is the quantum efficiency, h is Planck's constant, and $v = \dfrac{c}{\lambda}$ the frequency of the laser carriers. In this case, if $I_0 = I_{th} - I_{pol}$, the output power of the laser will therefore be:

$$P(t) = \begin{cases} 0 & \text{for} \ \ I_{rf}(t) \leq I_0 \\ \mu\left[I_{rf}(t) - I_0 \right] & \text{for} \ \ I_{rf}(t) > I_0 \end{cases} \tag{1.16}$$

The dynamic properties of the system are governed by the set of bandpass filters induced by the superposition of the pass bands of the *RF* amplifier, the photodiode, and the coupler. Taking advantage of the fact that the high cut-off frequencies f_H and the low cut-off frequencies f_L are very far from each other, it is estimated that this band pass filter consists of a cascade of low-pass linear filters and top-notch high passes. The input voltage $V_{in}(t)$ and the voltage $V_{out}(t)$ of the cascaded band pass filter obey:

$$V_{int}(t) = V_{out}(t) + \frac{1}{\Delta\Omega}\frac{du_s(t)}{dt} + \frac{\Omega_0^2}{\Delta\Omega}\int_{t_0}^{t} V_{out}(s)\,ds \tag{1.17}$$

and the optical output power P is then converted into the electrical domain through the photodiode (*PD*), according to the relationship $V(t) = SP(t - T_D)$, where T_D is the time-delay from the propagation time in the line of the fiber between the laser and the photodetector, and

S the sensitivity of the photodiode. The circuit input voltage of the electrical part can therefore be written as $V_{in}(t) = V(t) = S\mu D\left[I_{rf}(t - T_D) - I_0\right]$. The relationship between $V_{rf}(t)$ and the output voltage $V_{rf}(t) = \kappa G V_{out}(t)$ of the voltage attenuator is converted to current $I_{rf}(t) = V_{rf}(t)/R_Z$, where R_Z is the characteristic impedance used for the voltage-to-current conversion, and κ the dimensionless factor represents all the linear losses (electrical and optical) in the loop. Therefore, the voltage $V_{rf}(t)$ obeys [109]:

$$x + \tau \frac{dx}{dt} + \frac{1}{\theta}\int_{t_0}^{t} x(s)\,ds = \beta D\left[x(t - T) - \alpha\right] \tag{1.18}$$

where $\alpha = V_0$, and V_0 is equivalent to the current-voltage conversion of I_0 by $V_0 = R_Z I_0$. The scaled system variable is $x(t) = V_{rf}(t)$, and the feedback gain control parameter is $\beta = \kappa S \mu G / R_Z$.

By doing a stability study of their system, they showed that this stability depends on the sign of α. For $\alpha \geq 0$ $\left(I_{pol} \leq I_{th}\right)$, the system remains in its fixed equilibrium state regardless of the gain or time delay. It is therefore concluded that the bias current is absolutely a very important element when studying the system, in order to obtain non-trivial dynamic behavior. For $\alpha < 0 \left(I_{pol} > I_{th}\right)$, as β increases and reaches the value $\beta_1 = 1.32$, the limit cycle of frequency $f_1 = 612.1\ kHz$ emerges and becomes an attractive limit cycle for any initial condition taken around this unstable equilibrium point. It thus appears that the necessary condition for the emergence of oscillations is $I_{pol} > I_{th}$, and this depends heavily on the gain.

As a result, the behavior of their bifurcation diagram plotting the maximum of $x(t)$ as a function of the control parameter β shows the different state variations of the system (in three parts) when this control parameter is changed [109]:

❖Portion (A) is the region where $1 < \beta < 1.18$. No oscillation is observed. It turns out that the signal is zero, and the fixed point becomes attractive.

24

❖ Portion (B) is the region where $1.18 < \beta < 1.34$. A limit cycle of period T_D appears; the amplitude of these oscillations increases with the value of β.

❖Portion (C) is the region where $\beta > 1.34$. A limit cycle of slow time-scale oscillations appears which gradually gives rise to the appearance of a fast oscillation of period T_D just at the extrema as β increases continuously.

1.7.4 OEO with the electronic part cascaded by an electrical oscillator.

a) Van der Pol Optoelectronic Oscillator without Mach-Zehnder modulator

OEOs usually have a linear electrical branch where the electrical signal is amplified and the frequency is finally filtered. A very important point of view on the behavior of the *OEO* deserves investigation, such as when this electrical branch responds non-linearly to an input excitation. Goune et *al.*, therefore, explored the non-linearity of the electrical branch by introducing the self-sustaining Van der Pol (*VdP*) electrical oscillator, which is a classic example of a self-oscillating system [109]. Historically, the *VdP* oscillator was introduced by Balthasar Van der Pol in the 1920s. Since then, it has been a very important paradigm for autonomous systems and relaxation oscillations in physical and biological systems [110,111].

In this *OEO* (**figure 1.14**), the nonlinearity of the laser diode is used to perform the conversion from the electrical to the optical domain, while the electrical branch has a *VdP* nonlinearity. Thus, they experimentally implemented the system and its modeling in order to investigate the complex dynamics of the electrical output signal.
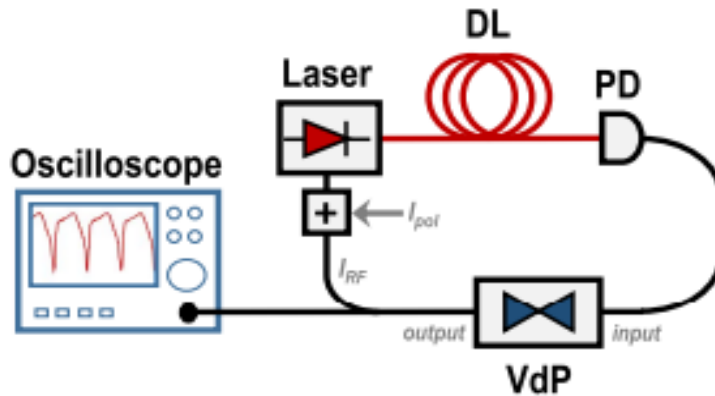
Figure 1.14: The experimental set-up of the Van der Pol-optoelectronic oscillator (VdP-OEO). DL: Delay line; PD: Photodiode; I_{pol}: Laser polarization current; I_{RF}: RF current from the feedback loop [65].

For their results, the bias voltage is taken as $V_{th} - V_{pol} = 2.05V$ to allow the laser to reach its linear operating region. As the gain increases, they observe a significant qualitative difference in harmonic behavior. The main difference between the *VdP* and the *VdP-OEO* is that the oscillations in the latter are asymmetric, with an asymmetry towards positive values. On the other hand, in the *VdP-OEO*, the transitions from negative to positive values are slower than that from positive to negative values, whereas both transitions are of equal duration in the case of the classical *VdP* oscillator. It is also important to note that in both time traces (theoretical and experimental), they also observe the typical increase in the oscillation period as the gain increases.

It is important to remember here that with the VDP oscillator they only obtained periodic and chaotic dynamics in their system.

b) Van der Pol Optoelectronic Oscillator with Mach-Zehnder modulator.

A representative diagram of this system is shown in **figure 1.15** (A.F Talla *et al*. in Breather and Pulse Package Dynamics in multi nonlinear electro-optical systems with delayed feedback). The optical signal in the feedback loop is delivered by a *DBR* semiconductor laser that emits continuous light of maximum power of 12 *mW* with a pump current of 100 *mA*, at the telecommunication wavelength $\lambda = 1559.8$ *nm*. The threshold of their laser is obtained for a measured pump current at $I_{th} = 27.3$ *mA*. This laser is modulated by a Mach-Zehnder electro-optical modulator characterized by its *RF* half-wave voltage $V_{\pi RF}$ and *DC* voltage $V_{\pi DC}$. The

output signal of the *MZ* passes through an optical fiber of length $L = 100\ m$ which introduces a delay $T_D = 0.5\ \mu s$ into the loop. The delayed optical signal is detected by a photodiode which performs the optical/electrical conversion with a sensitivity $S = 0.95\ A/W$. The electrical signal then passes through the *VDP* circuit, whose output is offset controlled, and amplified before returning to the *DC* electrode of the *MZM*. The *VDP* circuit inserted in the electrical branch of the feedback loop is a self-interacting oscillator consisting of a *LC* oscillator (whose frequency is $\omega_0 = 1/\sqrt{LC}$) and a nonlinear negative resistance.
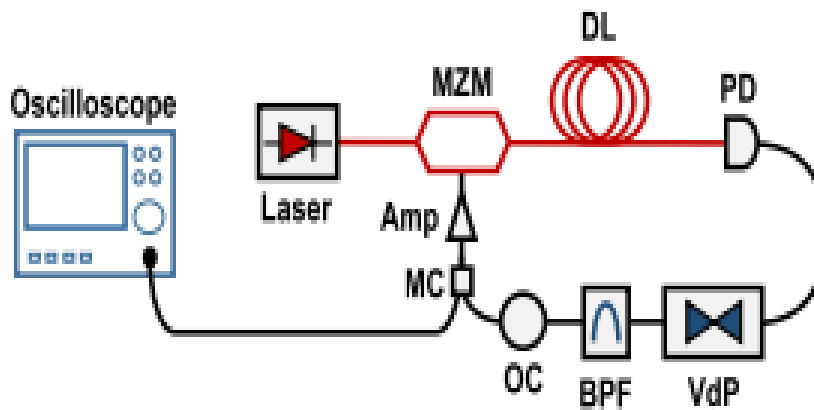
Figure 1.15: Setup for the VdP-OEO with Mach-Zehnder modulator. MZM: Mach–Zehnder modulator; DL: delay line; PD: photodiode; VdP: Van der Pol circuit; BPF: bandpass filter (note that this element stands here for all the bandpass filtering elements of the electric branch); OC: offset controller; MC: microwave coupler; Amp: amplifier [112].

To experimentally explore the complex dynamics of their oscillator, they first consider the case where the delay is fixed at zero (the delay line is removed). When they increase the laser current beyond the threshold, they first observe a hybrid regime where the oscillations are (multi-) periodic. The output voltage of the oscillator is a periodic limit-cycle with a single frequency $f = 0.91\ kHz$ which is of the same order of magnitude as the oscillation frequency of the *VDP* circuit. When the pump current *I* (and generally corresponding laser power *P*) is increased, quasi-rectangular oscillations appear on the sharp rising edge of the relaxation oscillations, but they are rapidly damped soon after their onset. At this stage, the breathers are still periodic. A further increase in pump current leads their system into a regime of complex oscillations involving chaotic breathers and pulse packages.

When the delay is taken into account (insertion of the 100 *m* long optical fiber), the system becomes infinite in dimension. In this case, the system can have other complex dynamical behaviors. They find that when the laser is pumped just above the threshold, relaxation oscillations and breathers comparable to those obtained in the zero delay case appear. However, when they increase the laser power, the system produces pulse packages that are chaotic while those obtained when $T_D = 0$ are periodic. Then a further increase leads their system to hyper-chaos [105]-[112].

It is important to note that their system oscillates with frequencies of the order of a few *kHz* imposed by the *VDP* oscillator.

1.7.5 Optoelectronic oscillators with nonlinear filters in electrical part.

The *CN-OEO* is one of the most recent *OEOs* proposed in 2019 [49]. Indeed, it is built by replacing the classical band-pass filter or the electronic oscillator with a nonlinear cubic filter (**figure 1.16**). This nonlinear filter is implemented using a nonlinear capacitor. It has boosted the complexity of the *OEO* dynamics which opens it to multiple applications such as secure communication, random bit generation…

In their oscillator, the nonlinear capacitor is used to introduce an additional integral term so that the resulting *OEO* model is presented as a novel extension of the broad bandpass Ikeda-like equation. The system can display attractors such as fixed points, limit cycles, and chaos, and is therefore compatible with all the related applications. It is also possible to control mixed-mode oscillations which in return favored quadrupled-frequency limit-cycle oscillations. Adding a nonlinear element in the electric branch is also a natural pathway to emulate complex coherent phenomena in coupled networks of *OEOs* (such as cluster synchronization, for example [113,114]). The final equation of this system is given by [49]:

$$x + \tau \frac{dx}{dt} + \frac{1}{\theta} \int_{t_0}^{t} x(s)\,ds + \eta \left(\int_{0}^{t} x(s)\,ds \right)^3 = \beta \cos^2 \left[x(t - T_D) + \phi \right] \qquad (1.19)$$

where $x = \pi V_{out}(t) / 2V_{\pi RF}$ is the dimensionless dynamical variable of the system. According to **Equation 1.19**, the cubic nonlinear band-pass filter is characterized by three-time scales which are the high cut-off time τ the low cut-off time θ, and the nonlinearity timescale

$\sqrt[3]{1/\eta}$. Therefore, adding the delay T_D transforms the *CN-OEO* into a four-timescales OEO. We will return to this equation in detail in Chapter 2.
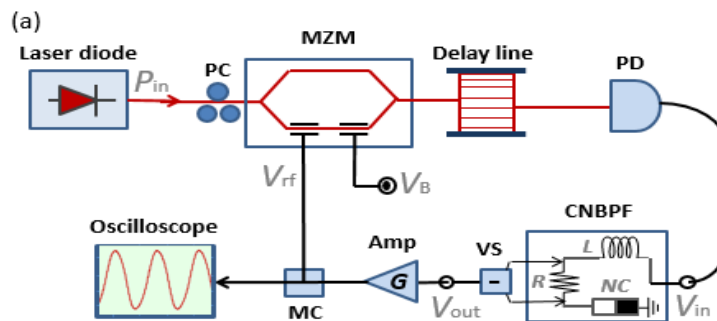
Figure 1.16: Set-up for the CN-OEO. V_B is the offset phase control voltage; PC: Polarization Controller; MZM: Mach-Zehnder Modulator; PD: Photodiode; CNBPF: Cubic-Nonlinear Band-Pass Filter; VS: Voltage Subtractor; Amp: RF amplifier; MC: Microwave Coupler [49].

The limit cycles generated with the device are of higher frequency and amplitude compared to the standard *OEO*. Their system can be operated either in narrow-band or wide-band configuration. It can display or not breathers by tuning some parameters for applications where they have to be either enhanced or avoided. This result shows that the *CN-OEO* is more versatile than the standard one. Their work also offers a more general overview of the origin of breathers in the wide-band *OEO*.

1.7.6 OEO with nonlinear amplifiers (sinh-OEO) [115]

Time-delayed dynamical systems generally feature smooth nonlinear transfer functions in the feedback loop, such as polynomial or sinusoidal functions. As a consequence, the complexity of their dynamical behavior mainly originates from the time-delay. But in 2021, Talla Mbé *et al.* (see **figure 1.17**) explore the opposite case where the nonlinear transfer function is complex ($\cos^2(\sinh)$), and therefore, non-smooth. They perform a bifurcation analysis of the system, and evidence that this novel type of time-delayed system can display a chaotic behavior characterized by positive maximum Lyapunov exponent and quasi-maximal entropy. The high entropy behavior of the system combined with post-processing are used to generate random numbers for small values of the feedback gain with an overall bit rate up to 1.478 Gb/s.

The optical signal in the feedback loop originates from a telecommunication laser diode, which outputs a continuous-wave signal of power P_L (few mW). This signal is used to seed an integrated lithium-niobate Mach-Zehnder modulator characterized by the radiofrequency and direct-current half-wave voltages $V_{\pi RF} = 3.9$ V and $V_{\pi DC} = 5.0$ V, respectively, and biased with a tunable but constant voltage V_B in the DC electrode. One should note that the nonlinear transfer function of this modulator is the conventional $\cos^2$ function, which is the same as the one feature in most OEO implementations. The optical output signal of the Mach-Zehnder modulator is then sent into a fiber delay line of time-delay. The delayed optical wave is then translated to the electrical domain using a photodiode of sensitivity S = 4.75 V/mW at 1550 nm with a detection bandwidth of 150 MHz, and the resulting electrical signal is subsequently routed to a band-pass filter with low- and high cut-off frequencies $f_L = 10$ Hz and $f_H = 5$ MHz, respectively. The filtered signal V_{in} is split with a microwave coupler into two: the first part is used to monitor the electrical signal in the loop owing to a digital oscilloscope while the other part is sent to a custom-made nonlinear amplifier, which outputs a signal V_{out} that is re-injected into the RF electrode of the Mach-Zehnder modulator to close the feedback loop.
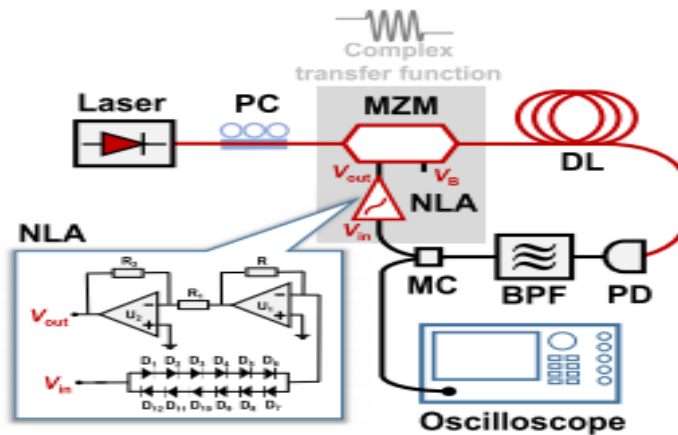
Figure 1.17: Set-up of the optoelectronic oscillator with complex transfer function. PC: Polarization controller; MZM: Mach-Zehnder modulator; DL: Delay line; PD: Photodiode; BPF: Band-pass filter; MC: Microwave coupler; NLA: Nonlinear amplifier (sinh) [115].

Taking into consideration the saturation voltage of the operational amplifiers ($V_{cc} = 15$ V), the relationship between the input V_{in} and the output V_{out} of their nonlinear amplifier is found to be a piecewise hyperbolic sine transfer function given as:

$$V_{out}(t) = \begin{cases} -V_{cc} & \text{if } V_{in} \leq -V_{in_C} \\ 2RI_0 \dfrac{R_2}{R_1} \sinh\left[\dfrac{V_{in}(t)}{6V_0}\right] & \text{if } |V_{in}| < V_{in_C} \\ V_{cc} & \text{if } V_{in} \geq V_{in_C} \end{cases} \qquad (1.20)$$

with $V_{\text{inC}} = 6V_0 arcsinh\ (R_1V_{cc}/2RR_2I_0)$ being the critical value of the input voltage for which the operational amplifiers saturate. The system designed in **figure 1.17** is ruled by the following integro-differential delayed equation [115]:

$$x(t) + \tau \dot{x}(t) + \frac{1}{\theta}\int_0^t x(\xi)d\xi = \beta f_{\text{NLA}}\left[x(t-T)\right] \qquad (1.21)$$

where $x(t) = \pi V_{in}(t)/2V_{\pi RF}$ stands for the state variable, and the overdot means the derivative with respect to time. The high and low cut-off times of the band-pass filter are $\tau = 1/2\pi f_H = 31.85$ ns and $\theta = 1/2\pi f_L = 15.92$ ms, respectively. The parameter $\beta = \pi \kappa SP_L/2V_{\pi RF}$ represents the feedback gain (with κ accounting for all the loop losses), while $\varphi = \pi V_B/2V_{\pi DC}$ is the offset phase of the Mach-Zehnder modulator. The complex function f_{NLA} originates from the combination of the Mach-Zehnder modulator and the nonlinear amplifier (NLA), and it yields:

$$f_{\text{NLA}}[x] = \begin{cases} f_- & \text{if } x \leq -x_c \\ \cos^2\left\{A\sinh[Bx]+\phi\right\}-\cos^2\phi & \text{if } |x| < x_c \\ f_+ & \text{if } x \geq x_c \end{cases} \qquad (1.22)$$

where

$$x_c = \frac{1}{B}\operatorname{arcsin} h\left(\frac{\pi V_{cc}}{2AV_{\pi RF}}\right), \quad A = \pi\frac{RI_0}{V_{\pi RF}}\frac{R_2}{R_1} \quad f_{\pm} = \cos^2\left(\pm\frac{\pi V_{cc}}{2V_{\pi RF}}+\phi\right)-\cos^2\phi, \quad B = \frac{V_{\pi RF}}{3\pi V_0} \quad (1.23)$$

x_C and $f_{\pm}$ are the critical values imposed by the saturation of operational amplifiers, while A and B are the dimensionless amplitude and phase coefficients of the nonlinear amplifier, respectively. In their case, A and B yield $A = 40.28$ and $B = 16.55$. For being the combination of two well defined functions ($cos^2(sinh)$), it is evident that f_{NLA} is *not* a smooth function but it appears to be complex.

31

Their experimental results are found to be in agreement with the numerical simulations. The theory developed predicted that the system should be chaotic for almost any

achievable gain value, and this behavior is recovered both numerically and experimentally. The amplitude of the chaotic oscillations steadily increases with the power of the laser diode, thereby confirming the trend indicated in their bifurcation diagram. It has been also shown that the proposed system produces high-order chaotic dynamics and then can be used as an entropy source. They show that although the limitation imposed by the saturation of the operational amplifier, this entropy source is complex enough to serve as a random numbers generator.

1.8 OEOs in science and technology [97]

In the last 20 years, there has been a steady growth in the number of publications related to *OEOs* from both scientific and technological viewpoints. As a consequence, the *OEO* has become one of the most studied systems in optoelectronics and microwave photonics [116]. From the fundamental side, *OEOs* permit one to investigate the properties of nonlinear time-delayed systems [25]. In this regard, delay-differential equations (*DDEs*) are mathematically infinite dimensional, exactly like spatially extended systems ruled by partial differential equations [117]. Because the timescales and delay time in *OEOs* can be distributed over up to 10 orders of magnitude, they emerged as excellent experimental benchmarks to investigate the rich bifurcation structure originating from the interplay between infinite dimensionality and nonlinearity, leading to complex dynamical states such as slow-fast relaxation oscillations, pulse-package trains, chaotic breathers, chimera states, or hyperchaos. From the applied perspective, propositions for innovative technological systems have been remarkably plentiful and diverse. As highlighted in the preceding sections, *OEOs* are used for ultrastable microwave generation and deliver some of the best phase noise performances at room temperature. *OEOs* are widespread in optical chaos communication architectures and have permitted successful demonstrations of multi-Gbit/s transmission in metropolitan optical fiber networks. Still, in the hyperchaotic regime, they are proven to be efficient sources of entropy for ultrafast random number generation, while passing some of the most stringent randomness tests. *OEOs* are a cornerstone in the emerging field of photonic reservoir computing and proved their potential in established benchmarks such as spoken-digit recognition or time-series forecasting. *OEOs* also have been developed for high-speed and high-sensitivity sensing of magnetic fields, temperature, pressure, or distance [97],[118].

1.9 Optical frequency combs (OFC)

1.9.1 What is an OFC?

It is a spectral structure characterized by a discrete and regularly spaced succession of lines. The traditional answer is that an *OFC* is a phase-stabilized mode-locked laser (*MLL*). While different generation methods have been developed over the past 20 years, *MLLs* were the original *OFC* sources. They were developed almost two decades ago to support the world's most precise atomic clocks. Acting as precision optical synthesizers, frequency combs enable the precise transfer of phase and frequency information from a high-stability reference to hundreds of thousands of tones in the optical domain.
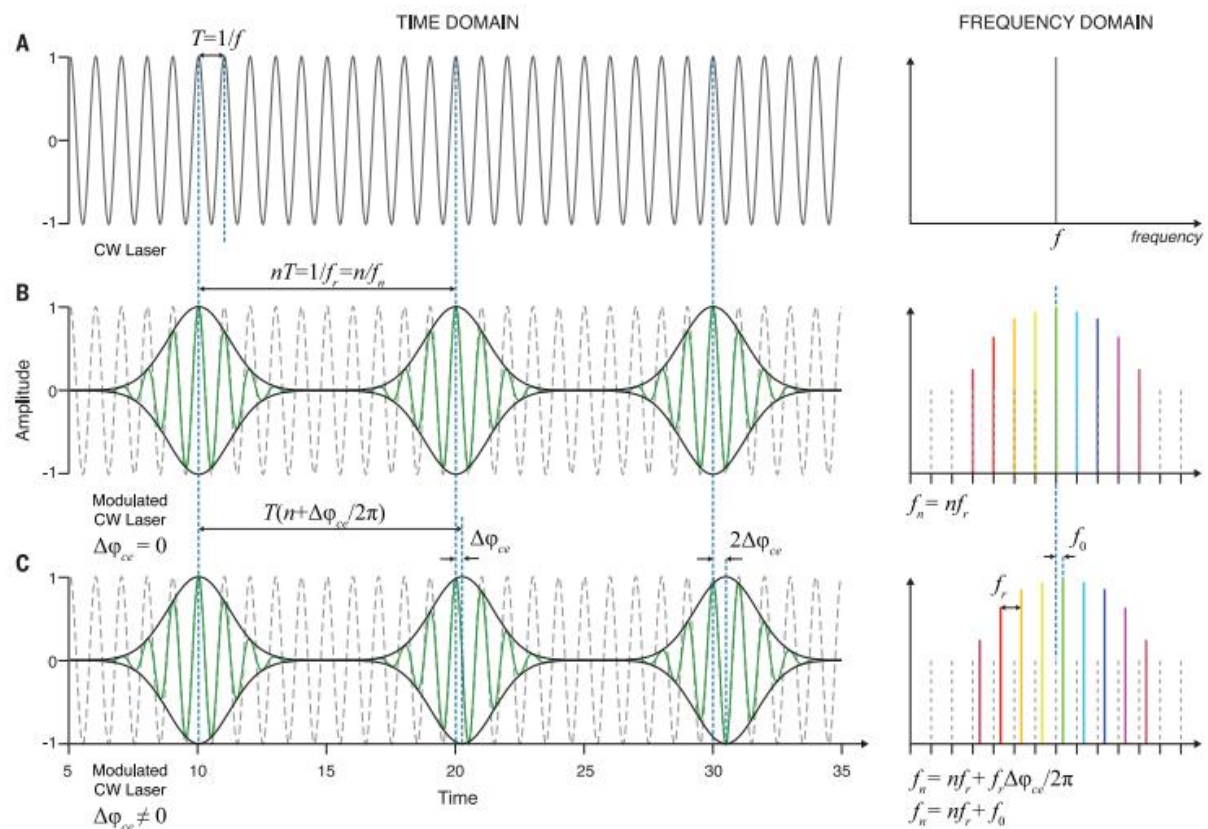
Figure 1.18: Time- and frequency-domain representations of the optical frequency comb [119].

This **figure 1.18** allows us to note that:

❖ (A) The continuous optical wave with frequency f and period T is represented as a single tone in the frequency domain.

❖ (B) An amplitude modulation on the optical wave at a lower frequency f_r that is an exact of f would enable simple frequency division by an integer n.

❖ (C) In general, the modulation frequency is not an exact sub-harmonic of f, but rather the modulation envelope "slips" concerning the fixed carrier f from pulse to pulse.

1.9.2 Combs equation

The behavior of the frequency comb spectrum is most succinctly described by the comb equation. The optical field of the laser pulse train can be described by a carrier frequency, $f_c = \omega_c / 2\pi$ that is modulated by a periodic pulse envelope, $A(t)$. Typically, the time between optical pulses ranges between 1 and 10 ns. Due to the pulse periodicity, the optical field can also be described as a periodic Fourier series of optical modes, $f_n = \omega_n / 2\pi$, with Fourier amplitude components, A_n, and mode number, n, such that [120]:

$$E(t) = A(t) e^{i\omega_c t} = \sum_{n=n_i}^{n_f} A_n e^{in \times \omega_n t} \tag{1.24}$$

Because f_c is not necessarily an exact multiple of the mode spacing, f_r, the individual Fourier frequencies are shifted from integer multiples of f_r by a common offset, such that [121]-[123]:

$$f_n = n * f_r + f_0 \tag{1.25}$$

where n is an integer. **Equation 1.25** is referred to as the comb equation.

❖**The repetition rate** (f_r) **i**s the comb spacing frequency. This frequency is also called the free spectral range.

❖**The offset frequency or the fundamental frequency** (f_0). Pulse formation necessarily requires that every longitudinal laser mode is perfectly equidistant in frequency and shares a common phase. The offset frequency, f_0, controls the carrier phase of the pulse train and

enables fine optical frequency tuning. The detection and control of the laser offset frequency f_0 is the key to allowing precise frequency determination of the comb modes. [120]

1.10 Conclusion

In this chapter, we have presented a review of the literature on some nonlinear electronic components (nonlinear capacitor, Colpitts oscillator), optical components (laser and applications, Mach-Zehnder modulator) as well as the different models of optoelectronic oscillators (in the field of science and technology). In the same way, the presentation of the modulation of the electric signals allows us to understand that the *OEO* presents internal as well as external modulations. This understanding allowed us to identify the problem of this thesis and to better understand the continuation of the work. The problems raised concerned the experimental realization and study of the dynamics of the *OEO* cascaded by an oscillator which presents both complex dynamics and high frequencies, and finally the numerical, analytical, and spectral study of *CN-OEO* as a function of the bandwidth and the non-linear coefficient term present in the equation. In the next chapter, the methodology to be followed for the resolution of the problems encountered will be presented.

Chapter 2

Methodology : Materials and Methods

2.1 Introduction

In the previous chapter, we posed two problems, namely the study of the dynamics of a self-sustained electronic oscillator with both complex dynamics and high frequency in order to insert it into the electrical part of the optoelectronic oscillator, and the study of the effet of some key parameters such as the bandwidth ant the cubic-nonlinear coefficient on the dynamics and the power spectrum of the *CN-OEO*. Thus, the aim of this chapter is to present the two systems used, and the approach to be followed for the numerical and analog resolution as well as to present the optical components necessary for the experimentation. **Section 2.2** is devoted to the presentation of the two systems (*OEO-Colpitts* and *CN-OEO* system). **Section 2.3** presents the electronic components and the method of analog simulation. In this section, we present some electronic components by establishing the equations that govern the operation of the electronic circuits incorporated in the electronic part of the *OEO*. **Section 2.4** is reserved for the presentation of the optical material used for the experimentation. **Section 2.5** is dedicated to the determination of the global equation of the CN-OEO system. The numerical method for solving the equations will be discussed in **section 2.6.** It deals with the Runge-Kutta method, the numerical tools for the characterization of the dynamic states of nonlinear systems, and finally the method of spectral analysis. The conclusion of the chapter appears in **section 2.7**.

2.2 Presentation of the two systems used in this thesis.

In this work, two different optoelectronic oscillator systems were considered.

2.2.1 OEO-Colpitts System

The proposed *OEO* with a Colpitts oscillator inserted in its electrical path is referred to as *OEO*-Colpitts whose schematic representation is shown in **figure 2.1**. This corresponds to the state where K_{in} and K_{out} are on in **figure 2.3 (a)**. The optical signal in the feedback loop is provided by a continuous-wave Distributed Feedback (*DFB*) laser diode. It delivers power up to 12 *mW* at the telecom wavelength $\lambda = 1.55$ *µm* and is also used to perform the electrical-to-optical conversion via its pump voltage electrode. The threshold of this laser diode is obtained experimentally for a pump voltage measured at $V_{th} = 1.02$ *V*. The light at the exit of

the laser diode is delayed by an optical delay line of time-delay T_D. The delayed optical signal is detected by a fast photodiode with an optical/electrical conversion factor $S = 0.95$ A/W.

(a)   **(b)**
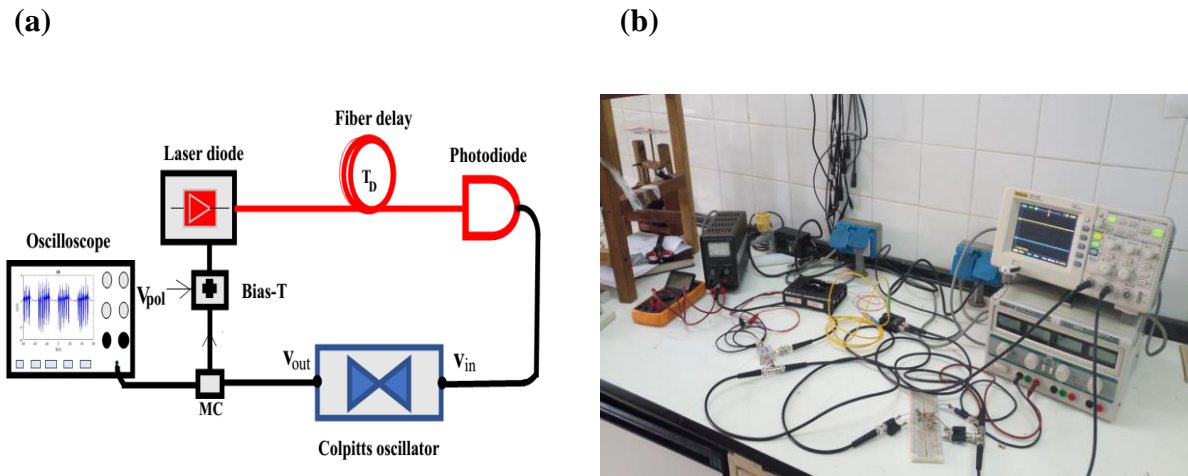
Figure 2.1: (a): Experimental set-up of the OEO-Colpitts oscillator. MC: Microwave Coupler. (b): A picture of the OEO-Colpitts oscillator in the laboratory.

When the switch K_{in} is on, this electrical signal feeds the Colpitts oscillator at a particular point of the circuit (V_{in}) and the output is probed at V_{out} (see **figure 2.3 (a)**) for the switch K_{out} on and then added to the polarization voltage (V_{pol}) before fedback to the electrode of the laser diode. A microwave coupler (*MC*) is used to visualize the signal at the input and output of the *OEO-Colpitts* thanks to a digital oscilloscope.

2.2.2 CN-OEO System

The experimental setup of the *CN-OEO* is presented in **figure 2.2 (a)** [67]-[68]. A telecommunication continuous-wave laser diode with wavelength $\lambda_L = 1.55$ μm and power P_{in} seeds a Mach-Zehnder modulator (*MZM*) characterized by a radio frequency (*RF*) and direct-current (*DC*) half-wave voltages $V_{\pi rf}$ and $V_{\pi dc}$, respectively. The modulated light is retarded by an optical delay line resulting in a time-delay T_D, before being converted to an electrical signal with a photodiode (*PD*) of responsivity S. The electrical signal generated by the photodiode V_{in} passes through a cubic-nonlinear band-pass filter (*CNBPF*) that outputs V_{out} and in turn is subjected to an amplification before being re-injected into the *RF* electrode of the *MZM*. We notice that the *CNBPF* is made of a resistor R, a coil L, and a nonlinear capacitor (*NC*). The nonlinear capacitor is constructed with an operational amplifier U (type *LF356*), two capacitors $C_{1,2}$, one resistor r, and a mixed assembly of eight simple junction

diodes (type *IN400X*) and whose characteristics are the thermal voltage V_T, the inverse saturation current I_S (**figure 2.2 (b)**). The number of junction diodes in series is $n = 4$.
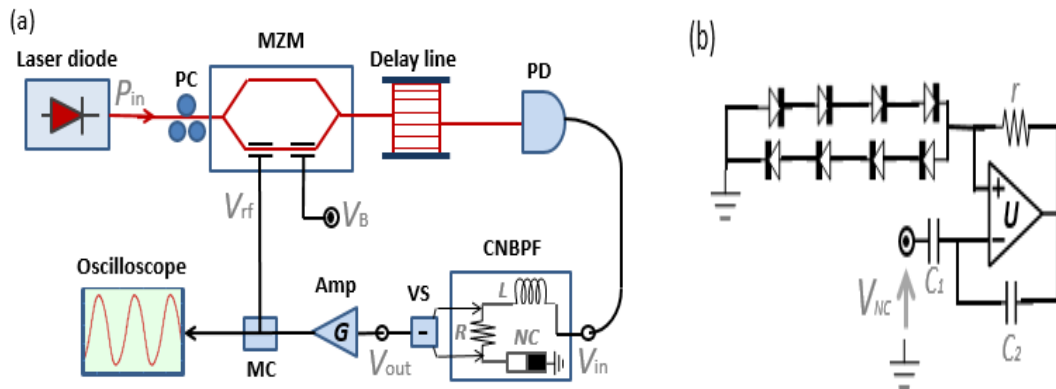
Figure 2.2 : (a): Set-up of the cubic-nonlinear optoelectronic oscillator.(b): Nonlinear capacitor (NC). PC: Polarization controller. MZM: Mach-Zehnder Modulator. V_B is the offset phase control voltage. PD: Photodiode. CNBPF: Cubic-nonlinear band-pass filter. VS: Voltage subtractor. Amp: RF amplifier. MC: Microwave coupler [67]-[68].

2.3 The electronic circuits used in this thesis.

An electronic circuit is a set of interconnected electronic components that can be active or passive and whose purpose is to perform a given function. Electronic components are elements intended to be assembled with others to perform one or more electronic functions.

In electronics, a component is active when it allows the power of a signal to be increased so that the additional power is recovered through a power supply. It allows the power of a signal to be amplified or transformed into voltage and/or current. In other words, it is capable of introducing energy into the circuit to which it contributes. In the vast majority of cases, active components are semi-conductors and are classified into two main categories: discrete active components (which carry out a single function) and integrated circuits (which are designed to carry out one of several electronic functions). On the other hand, a component is said to be passive when it does not allow the power of a signal to be increased; it can even sometimes reduce the power available at the output by the Joule effect.

In this thesis, by assembling passive and active components we will use two nonlinear circuits, namely the Colpitts self-sustained oscillator and the cubic nonlinear filter.

2.3.1 Self-sustained Colpitts oscillator.

In order to simulate this oscillator numerically and compare it with an analog simulation from the point of view of its dynamics, it is important to determine certain characteristics such as its frequency and its equations.

a) Determination of the frequency of the Colpitts oscillator.

In order to determine the oscillation frequency of the Colpitts oscillator, one consider the set-up given in **figure 2.3.** The total gain of the circuit is:

$$G = G_1 \times G_2 \tag{2.1}$$

(a) **(b)**
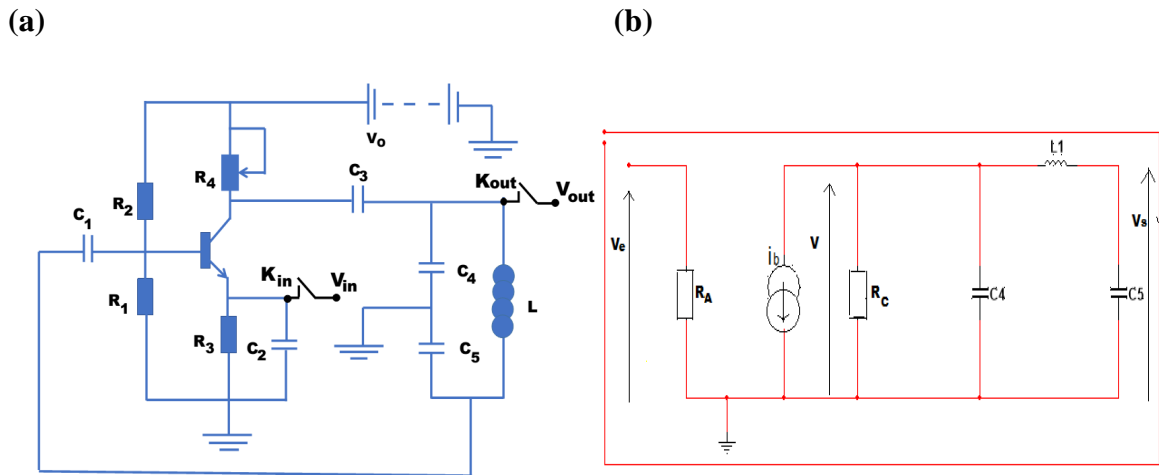
Figure 2.3: (a) Circuit of the Colpitts oscillator (b) Colpitts oscillator circuit in the static regime.

Where $G_1 = \dfrac{V_S}{V}$ is the gain of the tank circuit and $G_2 = \dfrac{V}{V_e}$ is the gain of the amplifier circuit.

❖Determination of G_1

$$\left(Z_{L_1} + Z_{C_5}\right)V_S = Z_{C_4}V \tag{2.2}$$

from which we have
$$G_1 = \frac{Z_{C_4}}{\left(Z_{L_1} + Z_{C_5}\right)} \tag{2.3}$$

❖Determination of G_2

$$V = -Z\beta i_b = -Z\beta \frac{V_e}{R_A} \tag{2.4}$$

In more detail

$$\left(R_C // Z_{C_4} \right) // \left(Z_{L_1} + Z_{C5} \right) \tag{2.5}$$

$$Z = \frac{R_C Z_{C_4} \left(Z_{L_1} + Z_{C_5} \right)}{R_C Z_{C_4} + \left(R_C + Z_{C_4} \right) \left(Z_{L_1} + Z_{C_5} \right)} \tag{2.6}$$

By replacing Z by its expression in **equation 2.4** we have:

$$G_2 = -\frac{\beta}{R_A} \left[\frac{R_C Z_{C_4} \left(Z_{L_1} + Z_{C_5} \right)}{R_C Z_{C_4} + \left(R_C + Z_{C_4} \right) \left(Z_{L_1} + Z_{C_5} \right)} \right] \tag{2.7}$$

The final expression for the gain of this oscillator is definitely given by:

$$G = -\frac{\beta R_C}{R_A} \left[\frac{Z_{C_4} Z_{C_4}}{Z_{C_4} Z_{C_5} + Z_{C_4} Z_{L_1} + R_C \left(Z_{L_1} + Z_{C_4} + Z_{C_5} \right)} \right] \tag{2.8}$$

Applying the Barkhausen criterion, we obtain the following two equations:

$$\begin{cases} -\dfrac{\beta}{R_A} \left[\dfrac{Z_{C_4} Z_{C_4}}{Z_{C_4} Z_{C_5} + Z_{C_4} Z_{L_1}} \right] = 1 \\ R_C \left(Z_{L_1} + Z_{C_4} + Z_{C_5} \right) = 0 \end{cases} \tag{2.9}$$

The first equation of the system allows for determining the oscillation condition while the second equation allows to obtain the oscillation frequency of the Colpitts oscillator. Thus we have:

$$-L_1 \omega^2 + \frac{1}{C_4} + \frac{1}{C_5} = 0 \tag{2.10}$$

$$\omega^2 = \frac{1}{L_1} \left(\frac{1}{C_4} + \frac{1}{C_5} \right) \tag{2.11}$$
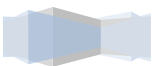
Hence the expression for the frequency is given by:

$$f = \frac{1}{2\pi}\sqrt{\frac{C_4 + C_5}{LC_4 C_5}}$$

(2.12)

This frequency will be determined by taking into account the values of our components. Subsequently, the determination of the equations of this oscillator is crucial in deciding to make a numerical study.

b) Determination of the Colpitts oscillator equations.

Taking into account the above circuit (**figure 2.3 (a)**) and applying Kirchhoff's laws we can write the equations of the Colpitts oscillator as follows:

$$\begin{cases} L\dfrac{dI_L}{dt} = V_{C_4} - V_{C_5} \\[2mm] R_1 C_1 \dfrac{dV_{C_1}}{dt} = 2V_{BE} + 2V_{C_2} - V_0 + R_1 I_b \\[2mm] R_3 C_2 \dfrac{dV_{C_2}}{dt} = R_3 I_E - V_{C_2} \\[2mm] R_4 C_3 \dfrac{dV_{C_3}}{dt} = V_0 - V_{C_3} - V_{C_4} - R_4 I_C \\[2mm] R_4 C_4 \dfrac{dV_{C_4}}{dt} = V_0 - V_{C_3} - V_{C_4} - R_4 I_C - R_4 I_L \\[2mm] R_1 C_5 \dfrac{dV_{C_5}}{dt} = R_1 I_L - 2V_{BE} - 2V_{C_2} - R_1 I_b + V_0 \end{cases}$$

(2.13)

Where V_{C_i} $(i = 1, 2, ..., 5)$ represent the voltages across the capacitors C_i. $V_{BE} = V_{C_5} - V_{C_2} - V_{C_1}$ is the emitter–base voltage, $I_E = f(V_{BE}) = I_S\left(e^{\frac{V_{BE}}{V_T}} - 1\right)$ the emitter current, I_C is the collector current, I_b is the base current ($I_C = \beta I_b$). V_T and I_S are the thermal voltage and the saturation current of the emitter-base of the bipolar junction transistor, respectively.

For convenient numerical analysis, let us introduce the following set of dimensionless variables and parameters to the system of **equation 2.13** of the Colpitts oscillator, above established in the previous chapter:

$$x_1 = \frac{V_{C_2}}{V_T}, \; x_2 = \frac{V_{C_3}}{V_T}, \; x_3 = \frac{V_{C_4}}{V_T}, \; x_4 = \frac{\rho I_L}{V_T}, \; x_5 = \frac{V_{C_5}}{V_T}, \; x_6 = \frac{V_{C_1}}{V_T}$$

$$\rho = \sqrt{\frac{L}{C_3}}, \; t = \tau.t', \; \tau = \sqrt{LC_3}, \; a = \frac{V_0}{V_T}, \; v_1 = \frac{V_{BE}}{V_T} = x_5 - x_6 - x_1$$

$$\gamma_2 = \frac{\sqrt{LC_3}}{C_1(\beta+1)V_T}I_S, \; a_1 = \frac{\sqrt{LC_3}}{C_2 V_T}I_S, \; b_1 = \frac{\sqrt{LC_3}}{C_2 R_3}, \; a_2 = \frac{\beta\sqrt{LC_3}}{C_3(\beta+1)V_T}I_S \tag{2.14}$$

$$a_3 = \frac{\sqrt{LC_3}}{R_4 C_4}, \; g = \frac{\beta\sqrt{LC_3}}{C_4(\beta+1)V_T}I_S, \; b_3 = \frac{C_3}{C_4}, \; a_5 = \frac{C_3}{C_5}, \; \gamma = \frac{2\sqrt{LC_3}}{C_5 R_1}$$

$$a_4 = \frac{\sqrt{LC_3}}{C_3 R_4}, \; v = \frac{\sqrt{LC_3}}{R_1 C_1}, \; , \; \varepsilon = \frac{\sqrt{LC_3}}{C_5(\beta+1)V_T}I_S$$

Therefore, the above equations are rewritten in the dimensionless form as:

$$\begin{cases} \dot{x}_1 = a_1 e^{v_1} - b_1 x_1 \\ \dot{x}_2 = a_4(a - x_2 - x_3) - a_2 e^{v_1} \\ \dot{x}_3 = a_3(a - x_2 - x_3) - g e^{v_1} - b_3 x_4 \\ \dot{x}_4 = x_3 - x_5 \\ \dot{x}_5 = a_5 x_4 + \gamma(\frac{a}{2} - x_5 + x_6) + \varepsilon e^{v_1} \\ \dot{x}_6 = v(x_5 - x_6 - \frac{a}{2}) + \gamma_2 e^{v_1} \end{cases} \tag{2.15}$$

It is important to note that each equation in this system of equations is an ordinary differential equation which will be solved numerically by the *RK4* method presented below.

In addition to the Colpitts oscillator, we also have the cubic-nonlinear band-pass filter.

2.3.2 Cubic-nonlinear band-pass filter (CNBPF)

The voltage V_{in} (voltage at the output of the photodiode) is filtered with a cubic-nonlinear band-pass filter (CNBPF) made of a coil L, a resistor R, and a nonlinear capacitor NC (see **figure 2.4 (a)**) [67]-[68]. The output voltage V_{out} of the *CNBPF* is the voltage difference probed across the resistor R. The inner structure of the nonlinear capacitor is depicted in **figure 2.4 (b**) [67]-[68]. It is implemented using an operational amplifier U (type LF356), two capacitors $C_{1,2}$, one resistor r, and a mixed assembly of eight simple junction diodes (type IN400X). These junction diodes are characterized by their thermal voltage $V_T = 25\ mV$, inverse saturation current $I_S = 5\ \mu A$, and the number of junction diodes in series $n = 4$.

(a)   **(b)**
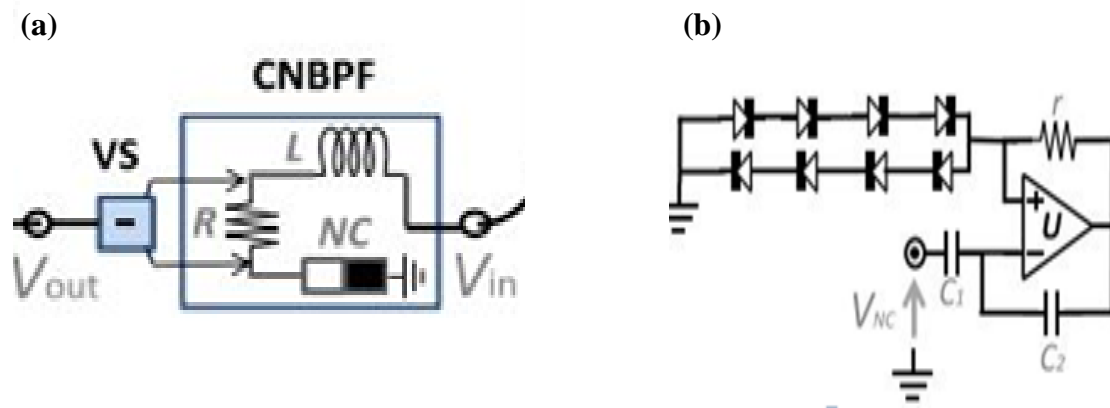
Figure 2.4: (a) Cubic-nonlinear band-pass filter (CNBPF) and (b) the inner structure of the nonlinear capacitor [67]-[68].

The application of the Kirchhoff laws permits to evaluate the voltage across such a nonlinear capacitor which is:

$$V_{NC}(q) = V_{C1} + V_d = \frac{q}{C_1} + 2nV_T Sinh^{-1}\left(\frac{i_2}{2I_s}\right) \tag{2.16}$$

And yet,
$$V^- - V_S = \frac{q}{C_2} \tag{2.17}$$

Because $\quad V^- = O \quad$ and $\quad V_S = ri_2 \tag{2.18}$

we therefore determine
$$i_2 = -\frac{q}{rC_2} \qquad (2.19)$$

where
$$V_{NC}(q) = \frac{q}{C_1} + 2nV_T Sinh^{-1}\left(-\frac{q}{2I_s rC_2}\right) \qquad (2.20)$$

$$q = \frac{1}{R}\int_0^t V_{out}(s)ds \qquad (2.21)$$

of the series capacitor, and yields the relationship

$$V_{NC}(t) = \frac{1}{R}\left(\frac{1}{C_1} - \frac{nV_T}{2rI_sC_2}\right)\int_0^t V_{out}(l)dl + \frac{nV_T}{48(rRI_sC_2)^3}\left(\int_0^t V_{out}(s)ds\right)^3 \qquad (2.22)$$

where t is the time. Then, the output voltage $V_{out}(t)$ of the *CNBPF* is related to the input $V_{in}(t)$ by:

$$V_{in}(t) = \frac{L}{R}\frac{dV_{out}(t)}{dt} + V_{out}(t) + V_{NC}(t) \qquad (2.23)$$

By plotting **equation 2.20**, we obtain the characteristics of the voltage as a function of the charge given by the following **figure 2.5** which is indeed a nonlinear behavior.
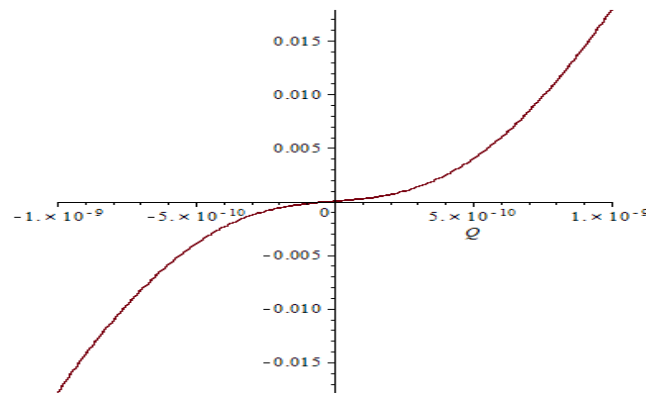
Figure 2.5: Characteristics curve of the nonlinear capacitor.

2.3.3 Electrical amplifier

The electrical amplifier is an amplifier circuit consisting of operational amplifiers and passive components of analog electronics (resistor and capacitor) integrated into a box. It is used to increase the power of the signal. Its gain depends on the frequency and voltage of the input signal. If G represents the gain of the amplifier or the amplification factor, the input signal $V_{in}(t)$ and the output signal $V_{out}(t)$ are related by the following relationship:

$$V_{out}(t) = GV_{in}(t) \qquad (2.24)$$
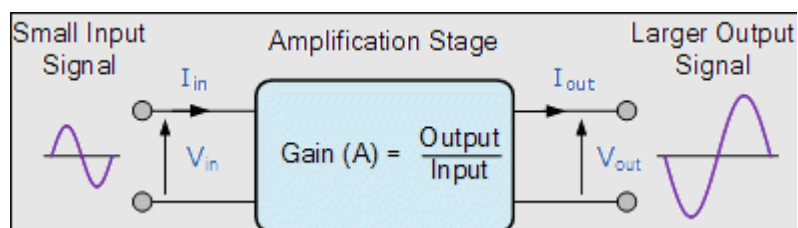
Figure 2.6: Diagram of an amplifier.

To build up our optoelectronic oscillator, we will also need the optical components.

2.4 The optical components used in this thesis

In addition to the electronic components used, the study carried out in this thesis also uses optical components which play an important role. Thus these two components, put together, form a feedback loop.

2.4.1 The laser diode

Our very first optical component is a wavelength-tunable multi-electrode laser diode (butterfly laser) which is a *DBF-type* semiconductor widely used in optical telecommunication. It emits a monochromatic (infrared) laser beam of rectilinear polarization and wavelength $l = 1.55\,\mu m$. This wavelength and its optical power are controlled by electrical current or voltage. To determine the threshold voltage of our laser, we have experimentally plotted the output voltage of this laser against the output voltage of the photodiode. For this purpose, this threshold voltage is approximately equal to 1.02 V (see **figure 2.7**). It is very important to remember here that these semiconductors must be handled with great care otherwise, they may deteriorate at the first manipulation.

According to this curve, when the active voltage of the laser emission is lower than 1.02 *V*, no phenomenon is observed. But for a voltage a little higher than this value, one can start to observe dynamics if the rest of the circuit obeys the oscillation conditions.
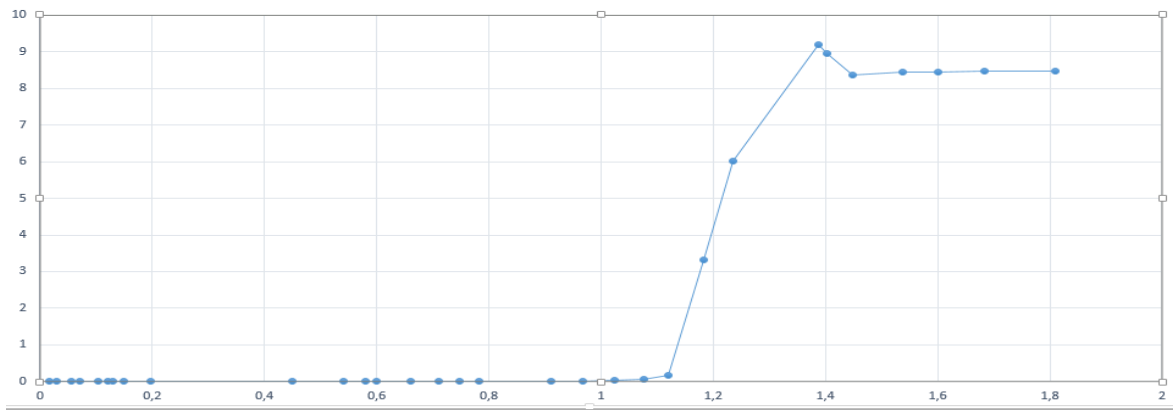
Figure 2.7: Laser diode, Laser mount, and Current-power characteristics of a laser diode.

2.4.2 Mach-Zehnder modulator

A beam of coherent light from the laser diode is modulated in intensity using the electro-optical effect and the principle of interferometry. The power of the incoming light beam (or intensity) P_{in} is ideally divided into two equal parts that are routed to two diverging optical paths (see **Figure 2.8**). In the first path, the light undergoes phase modulation and $\frac{1}{2}\sqrt{P_{in}}$ turns into $\frac{1}{2}\sqrt{P_{in}}e^{i\Delta\varphi}$, while in the other path the amplitude of the second beam suffers only from the phase shift of the material and turns into $\frac{1}{2}\sqrt{P_{in}}e^{i\Delta\varphi_0}$. Then, the two optical paths are reconnected and the beams interfere, resulting in the ideal case in total output power:

46

$$P_{out} = \left| \frac{1}{2}\sqrt{P_{in}}\,e^{i\Delta\varphi} + \frac{1}{2}\sqrt{P_{in}}\,e^{i\Delta\varphi_0} \right|^2 = P_{in}\cos^2\left[\frac{\pi V}{2V_\pi}\right] \tag{2.25}$$

$$\Delta\varphi = \frac{2\pi}{\lambda_0}n(E)L = \Delta\varphi_0 + \pi\frac{V}{V_\pi} \tag{2.26}$$

where, $$\Delta\varphi_0 = \frac{2\pi}{\lambda_0}n_0L, \quad V_\pi = \frac{\lambda_0 d}{2L}\left\{\left[\frac{dn}{dE}\right]_{E=0}\right\}^{-1} \tag{2.27}$$

λ_0 is the wavelength of the light beam passing through a Pockels medium of length L, V is a constant voltage applied across the thickness d. $E = V/d$ is an electric field which is therefore applied to the electro-optical medium and $\Delta\varphi$ is the accumulated phase shift at the output.

Taking into account the other characteristics, the final expression for the output power is that of the following equation given in Chapter 1:

$$P_{out} = P_{in}\cos^2\left[\frac{\pi}{2}\frac{V(t)}{V_{\pi RF}} + \frac{\pi V_B}{2V_{\pi DC}}\right] \tag{2.28}$$

Figure 2.8: Mach-Zehnder modulator.

Figure 2.8 is a representation of the Mach Zehnder modulator found on the market. At the output of this modulator, the optical fiber can be placed.

2.4.3 The optical fiber

An optical fiber is a very thin glass or plastic wire that is a conductor of light and is used for the transmission of data and light. It offers a much higher data rate than coaxial cables and can be used as a medium for a "broadband" network through which television,

telephone, video-conferencing, or computer data can be transmitted. In other words, it is the channel for transmitting optical information over very long distances and at previously impossible rates, and it creates a delay in the feedback loop. It consists of three concentric elements as shown in **Figure 2.9 (a).**

❖The core: Which generally varies between 10 and 85 μm. It is in this area, made of glass with a refractive index of n_1 that the light is guided and propagates along the fiber.

❖The cladding: A layer of glass with a refractive index of $n_2 \times n_1$ that surrounds the core (approximately 125 μm). The composition of the glass used is different from that of the core. The combination of these two layers allows the light to be confined within the core, by total reflection of the light at the core-cladding interface.

❖The protective layer or insulation: This is a mechanical protective coating generally made of polyvinyl chloride (*PVC*).

(a)   **(b)**
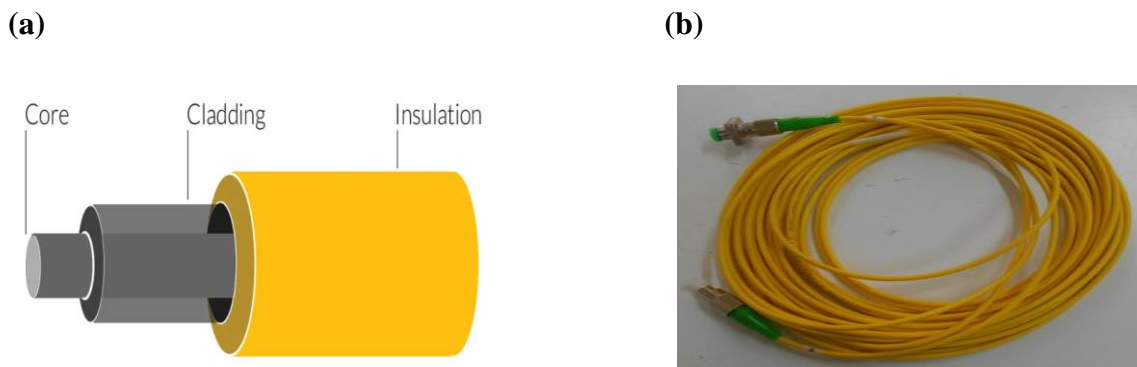
Figure 2.9: Structure and a roll of an optical fiber.
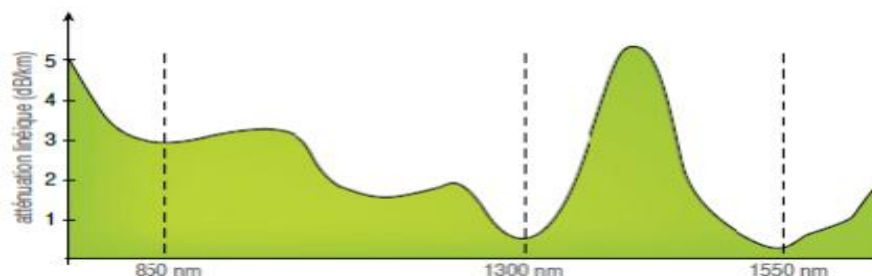
Figure 2.10: Attenuation in an optical fiber as a function of the wavelength of the light [129].

As light travels along the fiber, it gradually attenuates. This attenuation expressed in dB/km depends on the wavelength of the light used and is given by the relationship:

$$A\left(dB/km\right) = 10\log\left(\frac{P_{in}}{P_{out}}\right)$$

(2.29)

Where P_{in} and P_{out}, represent the input and output power of the optical fiber respectively. However, the wavelength of the light used to transmit a signal is not chosen at random. It must correspond to a maximum of attenuation (see **figure 2.10**). According to this figure, the wavelength of our laser used ($\lambda = 1.55\mu m$) corresponds to a minimum attenuation.

The time delay in the fiber is proportional to the refractive index of the core, the length of the fiber used, and inversely proportional to the speed of light according to the equation:

$$T = \frac{nL}{c}$$

(2.30)

When one has several fiber rolls and wishes to physically interconnect them, one must use the 'fiber to fiber' principle which consists of bringing them into contact using a precision alignment ring usually made of ceramic called a sleeve.

At the output of the optical fiber, which is an optical signal, an optical/electrical converter is required.

2.4.4 The photodiode

The role of the photo-detector is to convert optical power fluctuations, carrying information, into current fluctuations. In other words, it is used for optical/electrical conversion. It is the last element of the optical link and the first of the detection chain. That used (PDA10CF) is of the InGaAs type designed for the detection of signals in the 700-1800 *nm* wavelength range with an output impedance equal to 50Ω for a voltage of *5V* (**figure 2.11**). As for the choice of the optical fiber, that of this semiconductor for the detection of the signals is not also a coincidence but is preponderant because of its sensitivity which is close to 1 for the wavelength of our laser used. It intervenes in the optoelectronic equations by its sensitivity noted *S*.

(a)   (b)
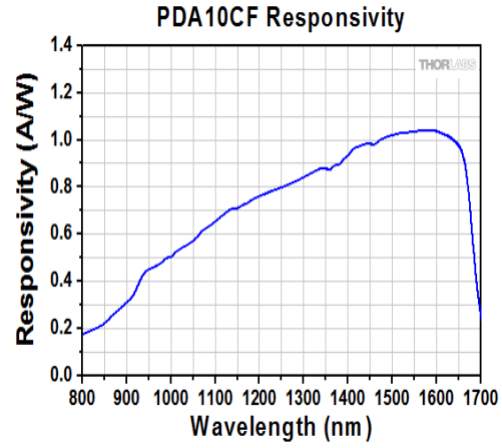
Figure 2.11: (a) Photodiode and (b) sensitivity of the photodiode as a function of the wavelength of the light signal [130].

2.5 Global equation of the CN-OEO system

Taking into account the electronic and optical components of the *CN-OEO* system listed above one can easily determine the equations governing the dynamics of this oscillator.

According to **equation 2.23**,

$$V_{in}(t) = \frac{L}{R}\frac{dV_{out}(t)}{dt} + V_{out}(t) + V_{NC}(t) \tag{2.31}$$

Where

$$V_{in}(t) = SGP_{in}\cos^2\left[\frac{\pi V(t-T)}{2V_{\pi RF}} + \frac{\pi V_B}{2V_{\pi DC}}\right] \tag{2.32}$$

is the output voltage of the photodiode or the voltage entering the non-linear filter, V_{out} is the output voltage of the filter and

$$V_{NC}(t) = \frac{1}{R}\left(\frac{1}{C_1} - \frac{nV_T}{2rI_s C_2}\right)\int_0^t V_{out}(l)dl + \frac{nV_T}{48(rRI_s C_2)^3}\left(\int_0^t V_{out}(s)ds\right)^3 \tag{2.33}$$

is the voltage across the nonlinear capacitor. Taking into account **equations (2.31), (2.32),** and **(2.33)**, the final equation is given by:

$$x + \tau\frac{dx}{dt} + \frac{1}{\theta}\int_{t_0}^t x(s)ds + \eta\left(\int_0^t x(s)ds\right)^3 = \beta\cos^2\left[x(t-T_D)+\phi\right] \tag{2.34}$$

where $x = \pi V_{out}/2V_{\pi RF}$ is the dimensionless dynamical variable of the system. Contrary to other *OEOs*, the particularities of *CN-OEO* come from the fact that it has the cubic-nonlinear band-pass filter and four timescales which are: the high cut-off time

$$\tau = L/R, \tag{2.35}$$

the low cut-off time
$$\theta = R \bigg/ \left(\left(\frac{1}{C_1}\right) - \frac{nV_T}{2rI_sC_2}\right) \tag{2.36}$$

the nonlinearity timescale
$$\sqrt[3]{1/\eta} \tag{2.37}$$

with

$$\eta = nV_T V_{\pi RF}^2 \bigg/ \left(12(rRI_sC_2)^3(\pi G)^2\right) \tag{2.38}$$

representing the cubic nonlinear coefficient, and the last timescale is the time-delay T_D. The normalized feedback gain and the offset phase are respectively $\beta = \pi SGP_{in}/2V_{\pi RF}$ and $\phi = \pi V_B/2V_{\pi DC}$.

      For mathematical convenience and without loss of generality, the following rescalings are done:

$$v = t/\theta, \quad \sigma = T_D/\theta, \quad x_\sigma = x(v - \sigma),$$
$$y = -\frac{1}{\theta}\int_0^t x(s)ds, \quad \rho = \eta\theta^3, \quad \varepsilon = \tau/\theta \tag{2.39}$$

so that **equation 2.34** can be rewritten in the form of the following flow:

$$\varepsilon\dot{x} = -x + y + \rho y^3 + \beta\cos^2(x_\sigma + \phi)$$
$$\dot{y} = -x \tag{2.40}$$

      This equation system is a delay-differential equations.

2.6 Numerical methods used to solve the problem

      Physical systems are described by equations whose analytical solution is not always obvious. The equations describing these systems are either in differential or algebraic form and thus require numerical approximations to describe the related physical phenomena.

Numerical methods are based on an algorithm that is implemented through computers to solve different types of problems. Computers enable us to approximate the solutions to analytically intractable problems, and also to visualize those solutions. In this thesis, the physical system is described by the ordinary differential equations (case of the Colpitts oscillator) and the delay differential equations (case of the *CN-OEO*).

2.6.1 Runge-Kutta method

Runge-Kutta methods are an important family of implicit and explicit iterative methods for the approximation of solutions of *ODEs*. These techniques have been elaborated for the first time in 1894 by Carle Runge and have been improved by Martin W. Kutta in 1901 [124,125].

a) The case of the ordinary differential equation (ODEs)

In this thesis, we will use the Runge-Kutta method because it is one of the most efficient numerical methods for these types of equations due to its advantage of being numerically stable [126]. There are several orders (second order, third order, and fourth-order) for this method but it is the fourth order that we use because of its stability.

If we consider a physical system described by the following first-order *ODE*:

$$\dot{x} = f(t, x),$$ (2.41)

with the initial condition $x(t_0) = x_0$. The Runge-Kutta method is used to approximate the exact solution numerically. The solution $x_{i+1} = x(t + h)$ is given by equation 2.2 where h is the integration step.

$$x_{i+1} = x_i + \frac{1}{6}(k_1 + 2k_2 + 2k_3 + k_4) + 0(h^5)$$ (2.42)

where the $k_{1,2,3,4}$ are given by :

$$k_1 = h \times f(t, x)$$
$$k_2 = h \times f(t + h/2, x + k_1/2)$$
$$k_3 = h \times f(t + h/2, x + k_2/2)$$
$$k_4 = h \times f(t + h, x + k_3)$$

(2.43)

It is important to know the initial condition x_0 in order to calculate the other values. For the case of an integro-differential equation of the form:

$$\dot{x} = f(t, x) + \alpha \int_{t_0}^{t} x(s)\,ds$$

(2.44)

with the initial condition $x(t_0) = x_0$, where α is a parameter that does not depend on time t and x. **Equation 2.4** is decomposed into two ordinary equations by introducing a new variable y.

$$\dot{y} = \alpha x(t)$$

(2.45)

$$\dot{x} = f(t, x) + \alpha y(t) = g(t, x, y)$$

(2.46)

Where $g(t, x, y)$ is the new function. The solution to this system of equations by posing $z(t, x) = \alpha x(t)$ is given by:

$$y_{i+1} = y_i + \frac{1}{6}(l_1 + 2l_2 + 2l_3 + l_4) + 0(h^5)$$

(2.47)

$$x_{i+1} = x_i + \frac{1}{6}(k_1 + 2k_2 + 2k_3 + k_4) + 0(h^5)$$

(2.48)

where the $k_{1,2,3,4}$ on the one hand and the $l_{1,2,3,4}$ on the other are given by:

$$k_1 = h \times g(t, x, y)$$
$$k_2 = h \times g(t + h/2, x + k_1/2, y + l_1/2)$$
$$k_3 = h \times g(t + h/2, x + k_2/2, y + l_2/2)$$
$$k_4 = h \times g(t + h, x + k_3, y + l_3)$$
$$l_1 = h \times z(t, x)$$
$$l_2 = h \times z(t + h/2, x + k_1/2)$$
$$l_3 = h \times z(t + h/2, x + k_2/2)$$
$$l_4 = h \times z(t + h, x + k_3)$$

(2.49)

Fortran 90 (mathematical FORmula TRANslating system) and Matlab (MATrix LABoratory) software are used to perform the calculations.

b) The case of the delay-differential equations (DDEs)

Contrary to ordinary differential equations where the initial conditions are given by a discrete and finite set of values, initial conditions in delay-differential equations should be specified using a function $g(t)$ defined on the continuous interval $[-\tau, 0]$ so that infinity of values has to be initially known to fully characterize a unique solution of the system. In this regard, delay-differential equations (*DDEs*) are mathematically infinite dimensional, exactly as spatially extended systems ruled by partial differential equations.

In delay differential equations, the dynamics at each time t depend on the value of the vector X at each time t, but also on the value of X at the previous time $t - \tau$, with $\tau > 0$ [25]. If we introduce the variable with delay $X(t - \tau)$ and $G = (G_1, G_2, ..., G_n)$ the n-dimensional vector field, the *DDE* is thus written:

$$\dot{X} = G(t, X(t), X(t - \tau))$$

(2.50)

with $\quad X(t) = g(t) \; for \; t \in [-\tau, 0]$

(2.51)

where g is a time-dependent n-dimensional vector, $X(t) = [x_1(t), x_2(t), ..., x_n(t)]$ and $X(t - \tau) = [x_1(t - \tau), x_2(t - \tau), ..., x_n(t - \tau)]$ are vector variables. The iterative scheme of RK4 for *DDE* is given in [127] as follows:

$$x_{i+1,j} = x_{i,j} + \frac{h}{6}\left(l_{1,j} + 2l_{2,j} + 2l_{3,j} + l_{4,j}\right) \tag{2.52}$$

$$t = t + h$$

Where

$$l_{1,j} = G\left(t_i, x_{\tau,i,j}, x_{i,j}\right)$$

$$l_{2,j} = G\left(t_i + h/2, x_{\tau,i,j}, x_{i,j} + hl_{1,j}/2\right)$$

$$l_{3,j} = G\left(t_i + h/2, x_{\tau,i,j}, x_{i,j} + hl_{2,j}/2\right) \tag{2.53}$$

$$l_{4,j} = G\left(t_i + h, x_{\tau,i,j}, x_{i,j} + hl_{3,j}\right)$$

i repre sents the time increment and j the index for the variable x_j.

2.6.2 Numerical tools for the characterization of the dynamical states of our nonlinear systems

a) Bifurcation diagrams

Another set of concepts useful for the analysis of dynamical systems is the theory of bifurcation. A bifurcation is a phenomenon in which, the properties of a dynamical system change qualitatively when a control parameter of the system is varied. In order to plot the bifurcation diagram of continuous dynamical systems, a set of consecutive maxima of the variable representing the attractor must be obtained or a periodic capture of the variable after each period when the period is known. In the bifurcation phenomena, attractors may appear, disappear, or be replaced by another one. Bifurcation diagrams help us to visualize these transitions. Thus, one can identify fixed points, periodic orbits, or chaotic attractors. One can also identify various routes to chaos taken by dynamical systems.

The value for which the bifurcation occurs is called the bifurcation point. There are several types of bifurcation. We can mention among others:

❖The fold bifurcation or node-col

In this type of bifurcation, two equilibrium points exist (one is stable and the other is unstable) before the bifurcation. After the bifurcation, no equilibrium exists.

❖The Hopf bifurcation

A Hopf bifurcation occurs when a periodic solution cycle or limit cycle surrounding an equilibrium point emerges or disappears when a parameter μ varies. When a stable limit cycle surrounds an unstable equilibrium point, it is called a supercritical Hopf bifurcation. If the limit cycle is unstable and surrounds a stable equilibrium point, it is called a subcritical Hopf bifurcation.

Moreover, some stable solutions like quasi-periodic oscillations can be misinterpreted from the bifurcation diagram as they are represented with dense points like chaos/hyper chaos solutions. Let us also note that hysteresis dynamics are tracked using this method by superimposing two sets of data corresponding respectively to increase and decrease values of the control parameter. Even though the bifurcation diagram helps to distinguish stable (periodic) solution areas from unstable (chaotic) ones; it doesn't provide any information about the kind of dynamic (chaos or hyper chaos) that is present in unstable areas.

Of this fact, Lyapunov exponents and phase portraits are some additional tools required to conclude the dynamics of the investigated system.

b) Lyapunov's exponent

To gain the most information from a dynamical system, one should look for its maximum Lyapunov exponent. Chaotic behavior is illustrated by a positive maximum Lyapunov exponent. The evaluation of the maximum Lyapunov exponent can be done by observing the evolution of small perturbations of the system during its evolution over time. Thus, for a positive maximum Lyapunov exponent, a stretch occurs when initially neighboring points are separated: this is chaos. Moreover, for a negative exponent, there is a contraction or approach that characterizes a unique oscillatory or static state: this is regularity; and finally, for a zero exponent, we have a set of quasi-periodic waveforms: this is the torus.

Two methods exist to achieve this, the first is to perform the spectral calculation of the Lyapunov exponent for all dimensions of the system. And the second consists to perturb the

system by introducing small variations on each of its axes. But, it is the second method that will be used in this thesis.

Thus, if we consider a system with n degrees, the small variations are given by $\varepsilon_1, \varepsilon_2, ..., \varepsilon_n$

such that we have :

$$
\begin{aligned}
x_1 &\leftarrow x_1 + \varepsilon_1, \\
x_2 &\leftarrow x_2 + \varepsilon_2, \\
\cdot \quad &\qquad ., \\
\cdot \quad &\leftarrow \quad ., \\
\cdot \quad &\qquad ., \\
x_n &\leftarrow x_n + \varepsilon_n.
\end{aligned}
\tag{2.54}
$$

Then, the maximum Lyapunov exponent will be defined by:

$$
\lambda_{\max} = \lim_{x \to \infty} \frac{1}{t} \ln\left(\sqrt{\varepsilon_1 + \varepsilon_2 + ... + \varepsilon_n} \right).
\tag{2.55}
$$

Furthermore, this maximum one-dimensional Lyapunov exponent $\lambda_{\max}$ can be calculated using the following general formula:

$$
\lambda_{\max} = \lim_{m \to \infty} \frac{1}{m} \sum_{i=0}^{m-1} \ln\left| f(x_i) \right|,
\tag{2.56}
$$

With m is a number of iterations

$$
f(x_i) = M_J \times u,
\tag{2.57}
$$

where M_J is the Jacobian matrix associated with the system and u is the local variable used to describe the dynamics of this system in the vicinity of the equilibrium point. There are two possible cases:

❖ $\lambda \leq 0$: In this case, we distinguish two sub-cases for which the oscillatory states are stable:

• Case where $\lambda < 0$. In this case, we have regular oscillations.

• Case where $\lambda = 0$. In this case, we have a toric orbit made up of a set of quasi-periodic waveforms.

❖ $\lambda > 0$: In this case, we have a toroidal orbit made of a set of quasi-periodic waveforms, which materializes the presence of a chaotic state.

Note that the combination of the bifurcation diagram and the maximum Lyapunov exponent is an efficient tool to study the behavior (chaotic or not) of a dynamic system. The bifurcation diagram allows accounting for the qualitative state of the system while the maximum Lyapunov exponent allows accounting for the state of the system quantitatively.

c) Time series

This time-based analysis is a specific way of understanding a sequence of points collected over a regular time interval and period rather than recording them intermittently or randomly.

Time series analysis typically requires a large number of data points to ensure consistency and reliability. An extensive data set ensures you have a representative sample size and that analysis can cut through noisy data. It also ensures that any trends or patterns discovered are not outliers and can account for seasonal variance. Additionally, time-series data can be used for forecasting-predicting future data based on historical data.

It is often important to accompany the time series with phase portraits.

d) Phase portraits

The region of the phase space towards which the trajectories of a dissipative dynamical system converge is called an "*attractor*". Attractors are geometrical shapes that characterize the long-term evolution of dynamical systems. There are four types of attractors: a point, a torus, a limit cycle, and a more complex fractal-like structure [128].

❖The "*fixed point*" attractor is a point in the phase space towards which the trajectories tend and is, therefore, a constant stationary solution,

❖The "*limit cycle*" attractor is a closed trajectory in phase space towards which the trajectories tend. It is therefore a periodic solution of the system,

❖The "*torus*" attractor represents the motions resulting from two or more independent oscillations which are sometimes called quasi-periodic motions,

❖ Strange attractors are much more complex than the others.

2.6.3 Fourier Spectral analysis

Observation of the dynamical state of the system in the time domain, phase portrait, and many others is often insufficient to deduce the mathematical expression of the signal. It would be interesting to find another representation that would provide more information about the signal than the usual time representation for example. This new representation should show certain characteristics of the signal directly, not in the time domain (as a function of time) but in the frequency domain, i.e. as a function of frequency. Power spectrum analysis is one of the main tools for exploring the oscillation characteristics of physical systems, especially when certain system parameters change.

Joseph FOURIER (1768-1830) French scientist profoundly influenced the mathematics and physics of the sciences of his century with his study of the propagation of heat, which led to the discovery of the trigonometric series bearing his name.

Fourier's Theorem states that under certain conditions of derivation and continuity, any periodic continuous-time signal $s(t)$ of period T_0 can be written as a sum of sinusoidal signals. This sum can be written in two ways:

❖ Real trigonometric form.

❖Complex exponential form.

Here we will focus on the real trigonometric form. Any periodic continuous-time signal s(t) of

period $T_0 \left(\omega_0 = \dfrac{2\pi}{T_0} \right)$ can be written:

$$s(t) = a_0 + \sum_{n=1}^{+\infty} a_n \cos(n\omega_0 t) + b_n \sin(n\omega_0 t)$$

$$A_n = |a_n| \quad , \quad \varphi_n = 0 \quad n \geq 0$$

(2.58)

with $\qquad a_0 = \dfrac{1}{T_0} \displaystyle\int_{t_0}^{t_0+T_0} s(t) dt \quad$ and $\quad b_0 = 0$ (2.59)

$$a_n = \dfrac{2}{T_0} \int_{t_0}^{t_0+T_0} s(t) \cos(n\omega_0 t) dt, \quad n \geq 1$$

(2.60)

$$b_n = \dfrac{2}{T_0} \int_{t_0}^{t_0+T_0} s(t) \sin(n\omega_0 t) dt, \quad n \geq 1$$

(2.61)

The next general term is still called the n_{th} harmonic, where A_n is the Fourier amplitude and φ_n is the phase at the origin.

$$u_n(t) = a_n \cos(n\omega_0 t) + b_n \sin(n\omega_0 t) = A_n \cos(n\omega_0 t - \varphi_n)$$

(2.62)

$$A_n = \sqrt{a_n^2 + b_n^2}, \quad A_n \geq 0 \quad \forall n$$

(2.63)

$$\varphi_n = \arctan \dfrac{b_n}{a_n}$$

(2.64)

❖a_0: average value of the signal (continue component)

❖Harmonic of order 1: fundamental.

❖Amplitudes A_n tend to 0 when n tends to infinity.

❖Decomposition independent of the interval $[t_0, t_0 + T_0]$

❖If $s(t)$ is an even number, $\quad b_0 = 0 \quad \forall n \qquad s(t) = a_0 + \sum_{n=1}^{+\infty} a_n \cos(n\omega_0 t)$ $\qquad$ (2.65)

$A_n = |a_n| \quad , \quad \varphi_n = 0 \quad n \geq 0$ $\hspace{7cm}$ (2.66)

❖If $s(t)$ is an uneven number, $a_n = 0 \quad \forall n$

$$s(t) = \sum_{n=1}^{+\infty} b_n \sin(n\omega_0 t) = \sum_{n=1}^{+\infty} b_n \cos\left(n\omega_0 t - \frac{\pi}{2}\right) \qquad (2.67)$$

Taking into account the expression for the Fourier amplitude, the Fourier power is given by

$$P = 20.0\log(|A_n|) \qquad (2.68)$$

2.7 Conclusion

In the first part of this chapter, our two systems were presented nemaly the *OEO-Colpitts* and *CN-OEO* system. Then we presented the components of the electrical and optical part of the *OEO*. In these sections, the frequency and the equations of the Colpitts oscillator have been found, as also that of the cubic nonlinear band pass filter (*CNBPF*) and we have listed the optical components used in this thesis. The threshold voltage of the laser diode used was obtained experimentally. The *RK4* methods for solving *ODEs* and *DDEs* applied to our equations previously determined as well as the method for spectral analysis of a system were presented. All these methods and components will be used in chapter 3. We will then present and discuss the numerical and experimental results obtained.

Chapter 3

Results and discussion

3.1 Introduction

In this chapter, we present the results obtained in the framework of our thesis work. **Section 3.2** will be devoted to the dynamics of the optoelectronic oscillator cascaded by the Colpitts oscillator. In this part, we will first make a theoretical and experimental study of the dynamics of the self-maintained Colpitts oscillator, and then an experimental study of the *OEO-* Colpitts system in the case of zero delays and in the presence of delay. Two types of dynamics exhibited by the Colpitts oscillator will be considered. In **section 3.3**, we will study the spectra and dynamics of the *CN-OEO* system as a function of two system parameters: the bandwidth of the bandpass filter and the nonlinear cubic coefficient term. The last section is reserved for the conclusion of the chapter.

3.2 Experimental study of the Colpitts-OEO system

We are exploring experimentally an optoelectronic oscillator featuring a Colpitts oscillator in its electrical path.

To make a good study of this system it is imperative to know first of all certain characteristics of the Colpitts oscillator being in its electric part namely the amplitude and the frequency of the various types of dynamic behavior which it delivers. For that a theoretical and experimental study of the Colpitts oscillator solitary is essential.

3.2.1 Theoretical and experimental study of the Colpitts oscillator

Oscillators of the Colpitts-type are well-known since they are commonly used as electronic oscillators for generating limit-cycle oscillations at radio frequencies and present some interesting advantages such as the relative simplicity of their electronic circuits. It was shown that with an appropriate setting of these circuit parameters, they can exhibit rich and complex dynamical behaviors (chaos) at various operating frequencies which potential applications are in communication, radar systems, and so on [73,74]. These attractive properties justify our choice to focus on this class of oscillators.

a) Experimental realization of the Colpitts oscillator circuit

The design of the Colpitts oscillator is shown in **figure. 3.1 (a)** when the switches K_{in} and K_{out} are off (which will be on in **section 3.2.2**). **Figure 3.1b** depicts its experimental set-

up in the laboratory. The following electronic components are used: four resistors (R_1, R_2, R_3, and R_4); five capacitors (C_1, C_2, C_3, C_4, and C_5) one coil (L), and one transistor of type *2N2222* which is polarized with $V_0 = 5$ *V*. This transistor (semiconductor) is a common *NPN* bipolar junction transistor (BJT) used for general purpose low-power amplifying or switching applications. It is designed for low to medium current, low power, and medium voltage. The gain of our transistor is measured with an appropriate multimeter and is equal to 261.

The values of these electronic components are given as follows in **table 1**:

Table 1: Values of the Colpitts oscillator components.

Designation	Components	Values
Resistors	R_1, R_2	10 kΩ
Resistor	R_3	100 Ω
Potentiometer	R_4	value 220 Ω
Coupling capacitors	C_1, C_3	10 nF and 1 nF
Decoupling capacitor	C_2	10 Nf
Capacitors	C_4, C_5	1 nF each
Coil	L	5 µH

Using **expression 2.12** of chapter 2, and the values of the components used in this circuit, we can calculate the theoretical value of its fundamental frequency which is equal to 3.20 *MHz*.

Note that in the circuit of **figure. 3.1**, the only nonlinear device is the bipolar junction transistor, which nonlinear character is responsible for the complex behavior experienced by the electronic circuit. The resistor R_4 is used both for damping and biasing purposes. As mentioned, we stress that the modification of the standard Colpitts oscillator allows shifting the fundamental frequencies to higher ones, closer to the threshold frequencies of the transistor [131].

Before studying its dynamics, we will first draw its bifurcation diagram.
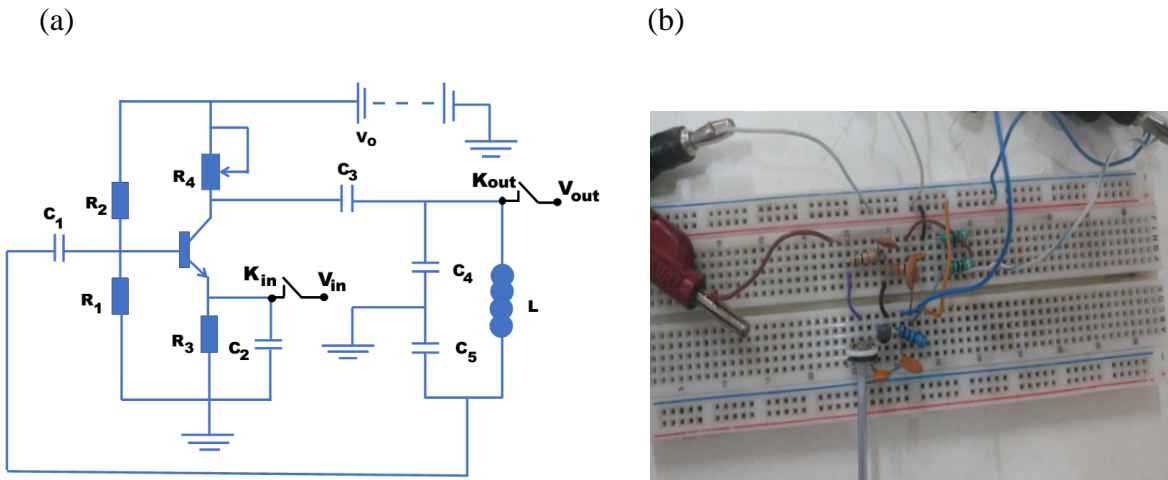
Figure 3.1: (a) Electronic circuit of the Colpitts oscillator. (b) A picture of the Colpitts circuit in the laboratory.

b) Bifurcation diagram

To better appreciate the frontiers between the different dynamical regimes of the Colpitts oscillator, its numerical bifurcation diagram is plotted in **figure 3. 2**. The bifurcation diagram is obtained by plotting the coordinate x_3 in terms of the control parameter R_4. It can be observed three parts in this bifurcation diagram, namely a fixed point when R_4 is inferior to 37 Ω. The limit cycle boundered at $[R_4 = 37\ \Omega; R_4 = 97\Omega]$. In this interval all the time traces of x_3 are periodic. The birth of bursting oscillations is observed for $R_4 \approx 98\ \Omega$. The maximum value of R_4 above which the bursting oscillations disappeared is $R_4 = 120\ \Omega$. Above this value, the Colpitts oscillator undergoes the unstable domain that is not shown in **figure 3.2**.

64
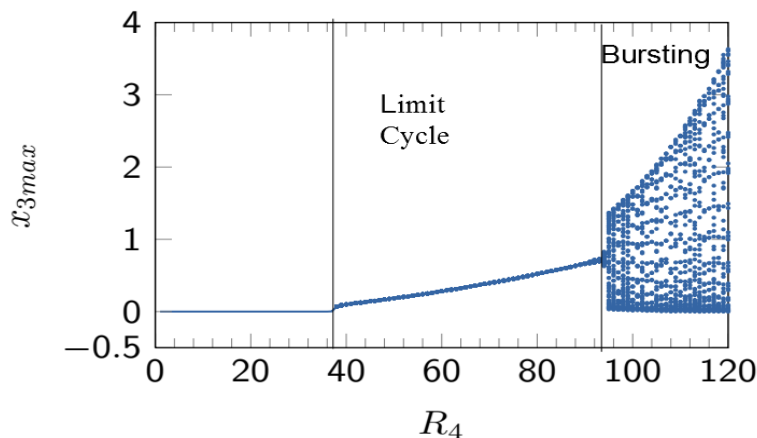
Figure 3.2 : Bifurcation diagram of the Colpitts oscillator showing the state variable x_3 versus R_4

Thereafter, we will use both forms of signals (limit-cycle and bursting) for the excitability in an optoelectronic oscillator.

c) Dynamics of the Colpitts oscillator

In addition to establishing the equations governing the operation of the Colpitts oscillator and even wiring its circuit on a test plate, we first used the Multisim software (see **figure 3.3**). This software gave us an idea of its dynamic behavior as well as the values of the components to be used. The only parameter of the circuit is the potentiometer R_4.
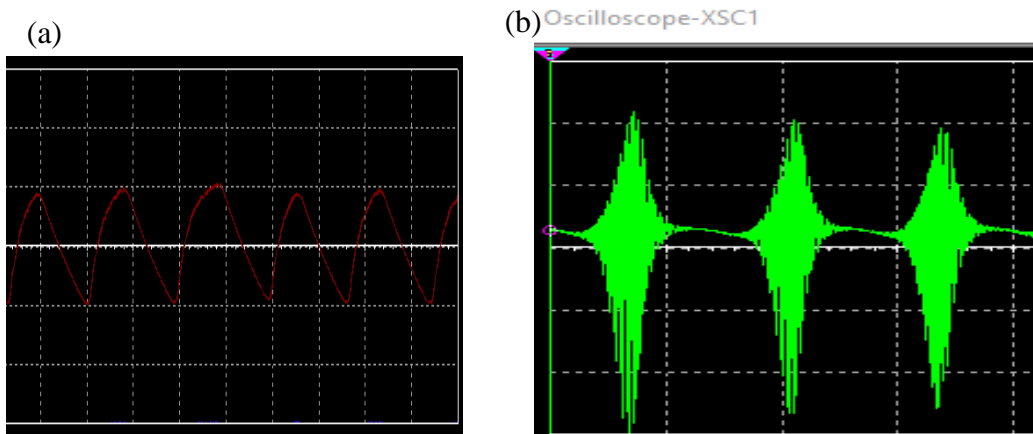
Figure 3.3: Limit-cycle and bursting oscillations in the solitary Colpitts oscillator obtained with Multisim software.

Experimentally, when tuning the potentiometer (R_4), different time traces have been recorded (**figure 3.4 (a)** and **(c)**) and compared to the numerical ones obtained from **equation 2.15** (see **figure 3.4 (b)** and **(d)**). It appears that the Colpitts oscillator exhibits limit-cycle and bursting oscillations depending on the value of the potentiometer. An interesting agreement is found between the numerical and experimental results. These two results confirm those already obtained with the electronic simulation software Multisim.

Figure 3.4.(a) and **(b)** present the case where $R_4 = 50 \ \Omega$. The Colpitts oscillator displays limit cycle oscillation having a frequency of 4.5 *MHz* and a maximum amplitude of 264 *mV*. As R_4 is further increased, the limit-cycle changes to the bursting oscillations (**figure 3.4.(c)** and **(d)**) for $R_4 = 105 \ \Omega$) exactly as predicted by the bifurcation diagram in **figure 3.2**.

Indeed, when R_4 is equal to $R_4 = 105 \ \Omega$, the bursting oscillation appears. These bursting oscillations are characterized by the alternation of two phases: silent and active phases. The silent phase (interval between two packages of oscillations) is characterized by a sort of dead zone where the voltage output is always constant to zero materialized by the

horizontal line existing between the packages. The active phase (packages of oscillations) consists of the transient apparition of fast oscillations over a short period compared to the period of the package which is referred to as slow.

Experimental   Numerical
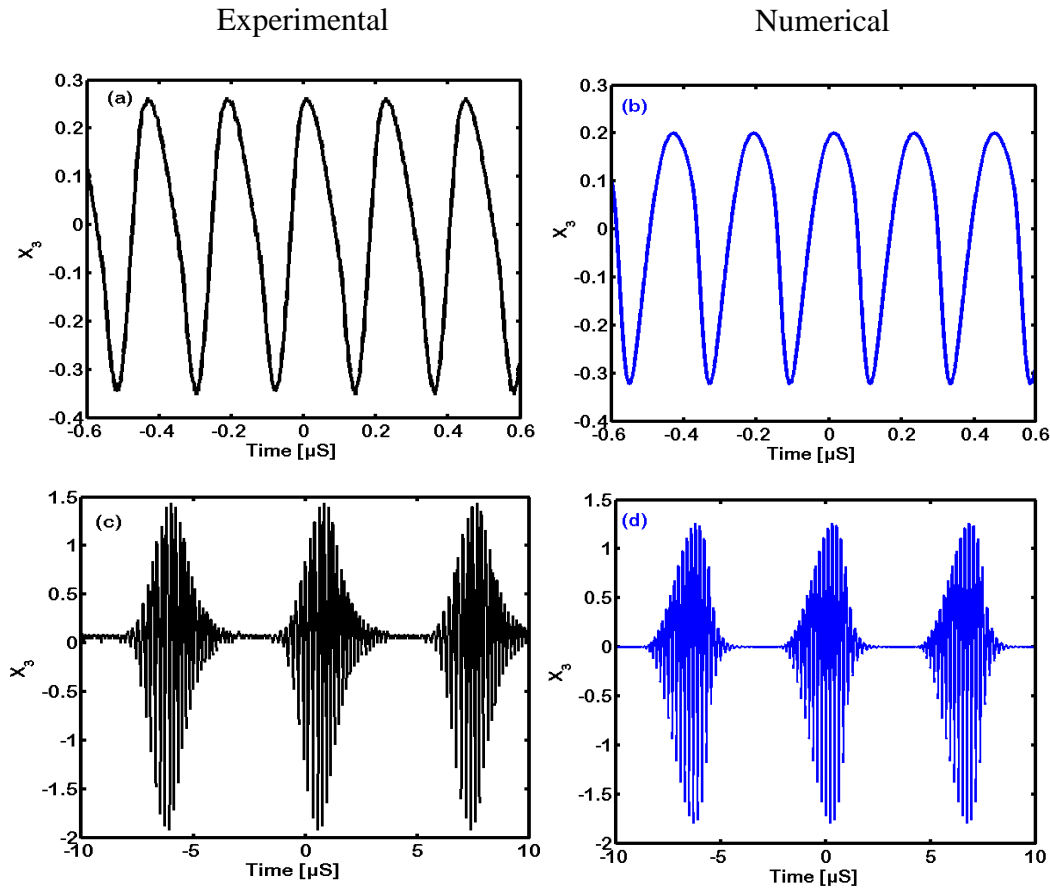
Figure 3.4: Limit-cycle and bursting oscillations in the solitary Colpitts oscillator. (a) and (c) are the experimental results (black color). (b) and (d) are numerical simulation results (blue color).

The frequency of the slow oscillation is equal to 2.5 *MHz* with a maximum amplitude of 1.44 *V*. These bursting oscillations similar to the conventional heart sound signals (Kingni et al. 2013) are quite raised in amplitude and frequency and could also be used in telecommunication as the amplitude modulator (*AM*), and for radar systems if higher frequencies are attained.

It is also important to note that the minimum and maximum frequencies of the limit-cycle obtained experimentally with this oscillator are 3.5 *MHz* (which is appreciably close to the theoretical frequency of 3.2 *MHz*) with a maximum amplitude equal to 120 *mV* and 4.76

MHz with a maximum amplitude of 320 *mV*, respectively given by **figure 3.5 (a)** and **(b)** for different values of *R₄*.
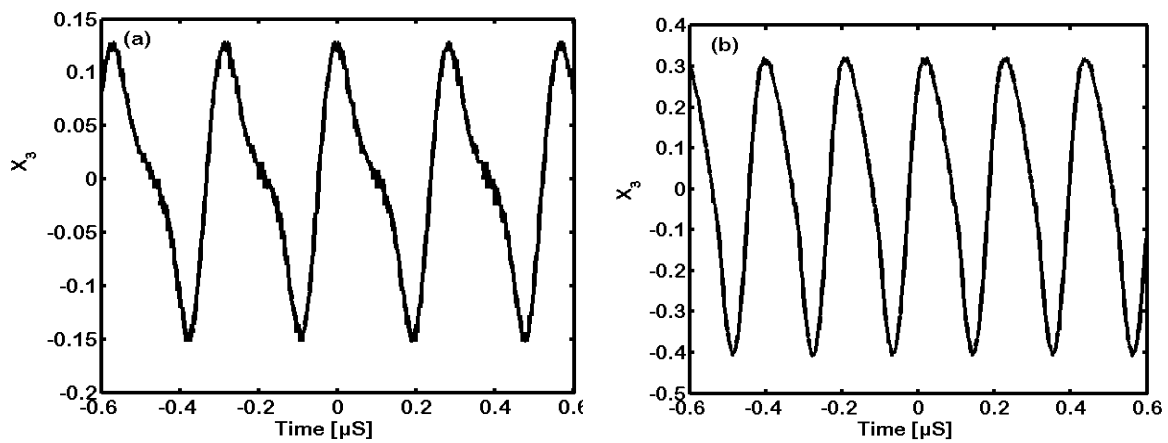
Figure 3.5: Other experimental limit-cycles of the Colpitts oscillator. (a) limit-cycle with the lowest frequency of $3.5 \ MHz$ ***(*** $R_4 = 40\Omega$ ***) and (b) limit-cycle with the highest frequency of*** $4.76 \ MHz$ ***(*** $R_4 = 80\Omega$ ***).***

In addition to the bursting oscillations, this oscillator exhibits another very interesting dynamic behavior, namely the mixed-mode oscillations as shown in **figure 3.6**. This type of dynamic behavior is characterized by an alternation between high and low amplitude oscillations, also known as a breather, and finds its application in various fields such as electrical and electronic engineering (circuits and control systems), mechanical systems and transport vehicles, as well as electrochemistry and biological structures. It is also obtained for a value of the potentiometer taken at $R_4 = 105 \ \Omega$.

As in the previous cases, a good agreement is also obtained between the numerical (blue color) and experimental results (back color) which allowed us to validate the experimental model of our Colpitts oscillator.
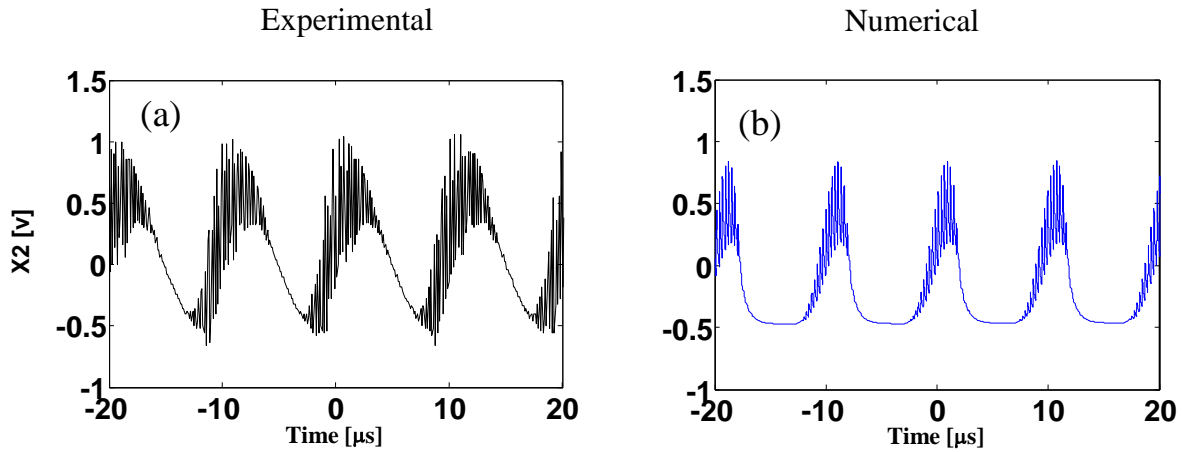
Figure 3.6: (a) Black color for experimental result and (b) blue color for numerical simulation. Mixed-mode oscillation in Colpitts oscillator.

3.2.2 Results obtained by inserting the Colpitts oscillator into the OEO

Inserting the Colpitts oscillator in the optoelectronic oscillator (see **figure 2.1**), we put forward the interaction between optical nonlinearity and electronic nonlinearity to obtain also complex dynamical behaviors. The resulting system is called OEO-Colpitts. The temporal dynamics of the system with and without delayed feedback are investigated experimentally.

The different dynamical states of the Colpitts oscillator found in **section 3.2** necessarily affect the dynamics of the system as developed hereafter.

a) Dynamics of the OEO-Colpitts oscillator

The goal here is to study the interaction between the nonlinearity due to the solitary Colpitts oscillator and that of the *OEO*. We then focus on three parameters of the system to analyze its dynamics: the potentiometer of the Colpitts oscillator, the power of the laser, and the length of the optical fiber. To analyze the dynamics of the *OEO-Colpitts* oscillator, two major cases are considered. Firstly, the case where the Colpitts oscillator generates a limit-cycle (potentiometer $R_4 = 50$ Ω) and secondly when it emits a bursting oscillation (potentiometer $R_4 = 105$ Ω), considering in each case the cases with and without delay. The question is to see what happens in the optoelectronic systems in these states.

68

i) Case with the limit‑cycle of the Colpitts oscillator ($R_4 = 50\ \Omega$)

The principal tunable parameter of the *OEO-Colpitts* oscillator is the polarization voltage V_{pol}. To explore experimentally the complex dynamics of the oscillator, we first consider the case where the time-delay is set to zero (the delay line is removed: $T_D = 0$). When the polarization voltage is increased beyond the threshold, a regime of multi-periodic oscillations is observed as displayed in **figure 3.7 (a),(e)** (for V_{out} and V_{in}). This signal oscillates with a maximum frequency equal to $f = 18.18\ MHz$ and a maximum amplitude of 4.72 *V* for V_{out} and 1.15 *V* for V_{in}, which are large compared to the oscillation frequency and the maximum amplitude of the solitary Colpitts oscillator found equal to 4.5 *MHz* and 264 *mV*, respectively (see **section 3.2**). Precisely, this frequency is four times the one of the solitary Colpitts oscillator (**18.18⁄4.5 ≈ 4.**).
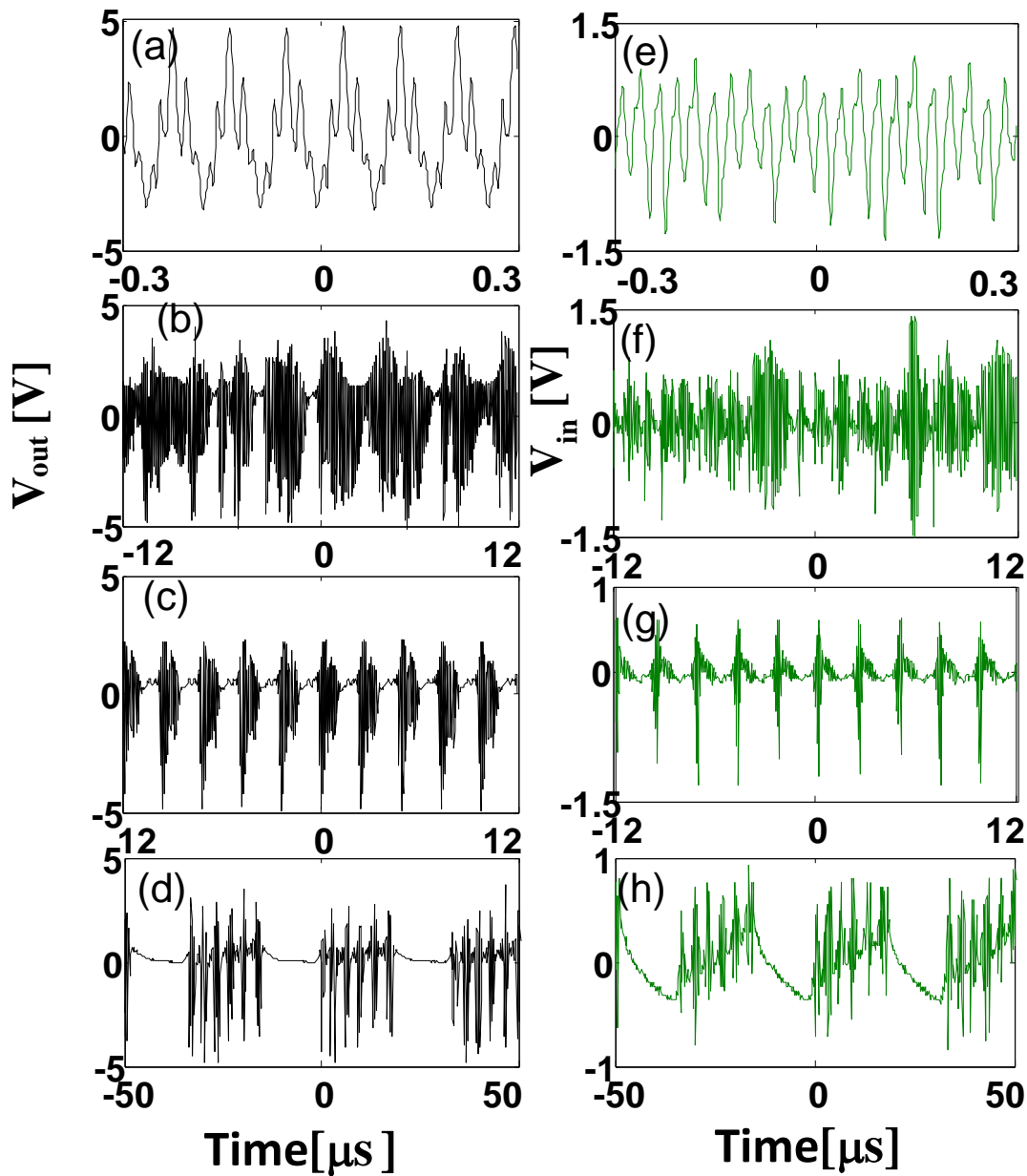
Figure 3.7: Black color for Vout and green color for Vin: (a)and(e)) Multi-periodic, (b)and(f) chaotic bursting, (c)and(g) periodic bursting, and (d)and(h) pulse-package oscillation in the time domain as the polarization voltage is increased beyond the threshold ($T_D = 0$). (a),(e) $V_{pol} = 1.29\ V_{th}$; (b),(f) $V_{pol} = 1.34\ V_{th}$; (c),(g) $V_{pol} = 1.4\ V_{th}$; (d),(h) $V_{pol} = 1.6\ V_{th}$.

As the polarization voltage is increased, it appears a chaotic bursting oscillation (see **figure 3.7 (b),(f)** for the two voltages) and thereafter these bursting become periodic

characterized by the fast-scale dynamics superimposed onto a slow-scale, as displayed in **figure 3.7 (c),(g)** for the two voltage. The frequency of the slow oscillation is equal to 438.6 *kHz* (frequency of the package) and with a maximum amplitude equal to 2.32 *V* for V_{out} and 0.55 *V* for V_{in}. The interval between two packages is characterized by a sort of a single oscillation and at the inner of each slow-scale dynamics (package), the chaotic fast-scale dynamics are observed. Thereafter, higher polarization voltage leads the system to a dynamical state corresponding to chaotic pulse-package oscillations observed in **figure 3.7 (d),(h)**, and the system continues to exhibit these chaotic oscillations until the signal extinguishes (not shown).
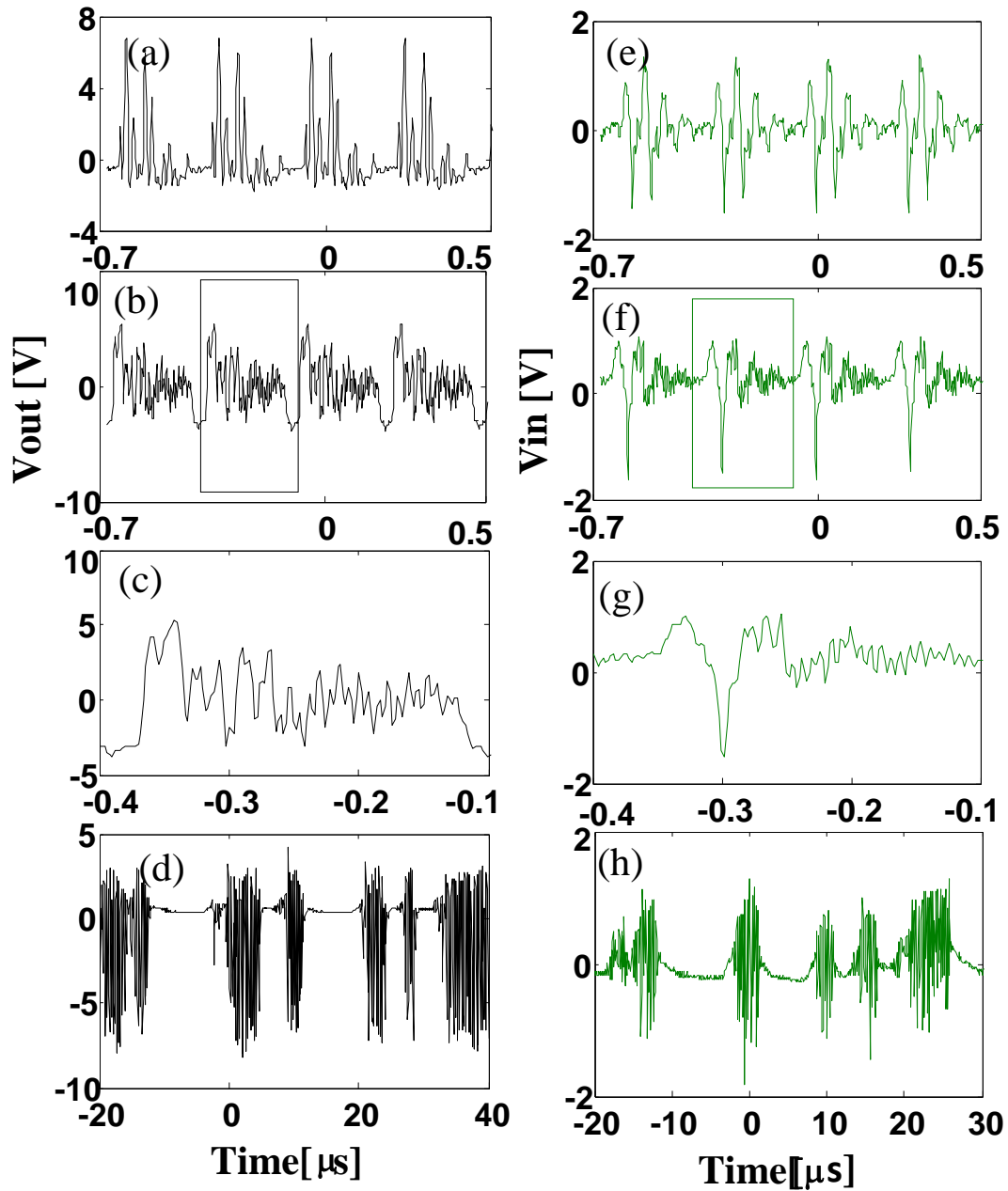
Figure 3.8: Black color for V_{out} and green color for V_{in}: (a),(e) Multi-periodic, (b),(f) slow-fast dynamics, and (d),(h) chaotic bursting oscillation in the time domain as the polarization voltage is increased beyond the threshold ($T_D = 0.2$ μs). (a),(e) $V_{pol} = 1.09\ V_{th}$; (b),(f) $V_{pol} = 1.24\ V_{th}$; (d),(h) $V_{pol} = 1.54\ V_{th}$; (c),(g) are the enlargements of one package of (b)and(f).

In the second consideration and still, in the case with the limit-cycle oscillation of the solitary Colpitts oscillator, the time delay is accounted for (insertion of the optical fiber of length 43 m ∶ $T_D = 0.2$ μs). The system becomes infinite-dimensional. For a value of polarization voltage just beyond the threshold, multi-periodic dynamics are observed (see

figure 3.8 (a),(e) for the case of the two voltages) with a maximum amplitude equal to 6.8 *V* (for V_{out}) , 1.4 *V* for V_{in} and with the maximum frequency of the system rather equal to 16.67 *MHz*. This maximum frequency has slightly decreased (16.67 *MHz*) compared to the case where the delay line is removed (18.18 *MHz*) but the maximum amplitude has increased (from 4.7 to 6.8 *V* for V_{out} and form 1.15 to 1.4 *V* for V_{in}). However, when the polarization voltage increases, the system generates other types of multi-periodic states characterized by fast-scale dynamics alternated by slow-scale dynamics as observed in **figure 3.8 (b),(f)** with a maximum frequency equal to 13.89 *MHz* and a maximum amplitude equal to 5.36 *V* for V_{out} and 1 *V* for V_{in}.

Figure 3.8 (c),(g) show the enlargement of one package of **figure 3.8 (b),(f)** unveiling the fast-scale dynamics. This enlargement allows observing that the system has several amplitudes in its dynamics. We find that a further increase of the polarization voltage finally drives the system in a regime of chaotic bursting oscillations given in **figure 3.8 (d),(h)** for the two voltages. Here, the maximum frequency is reached when the polarization voltage is increased just beyond the threshold before gradually drops. Therefore, the insertion of the optical fiber delay line in the system increases the maximum amplitude but also slightly decreases the maximum frequency.
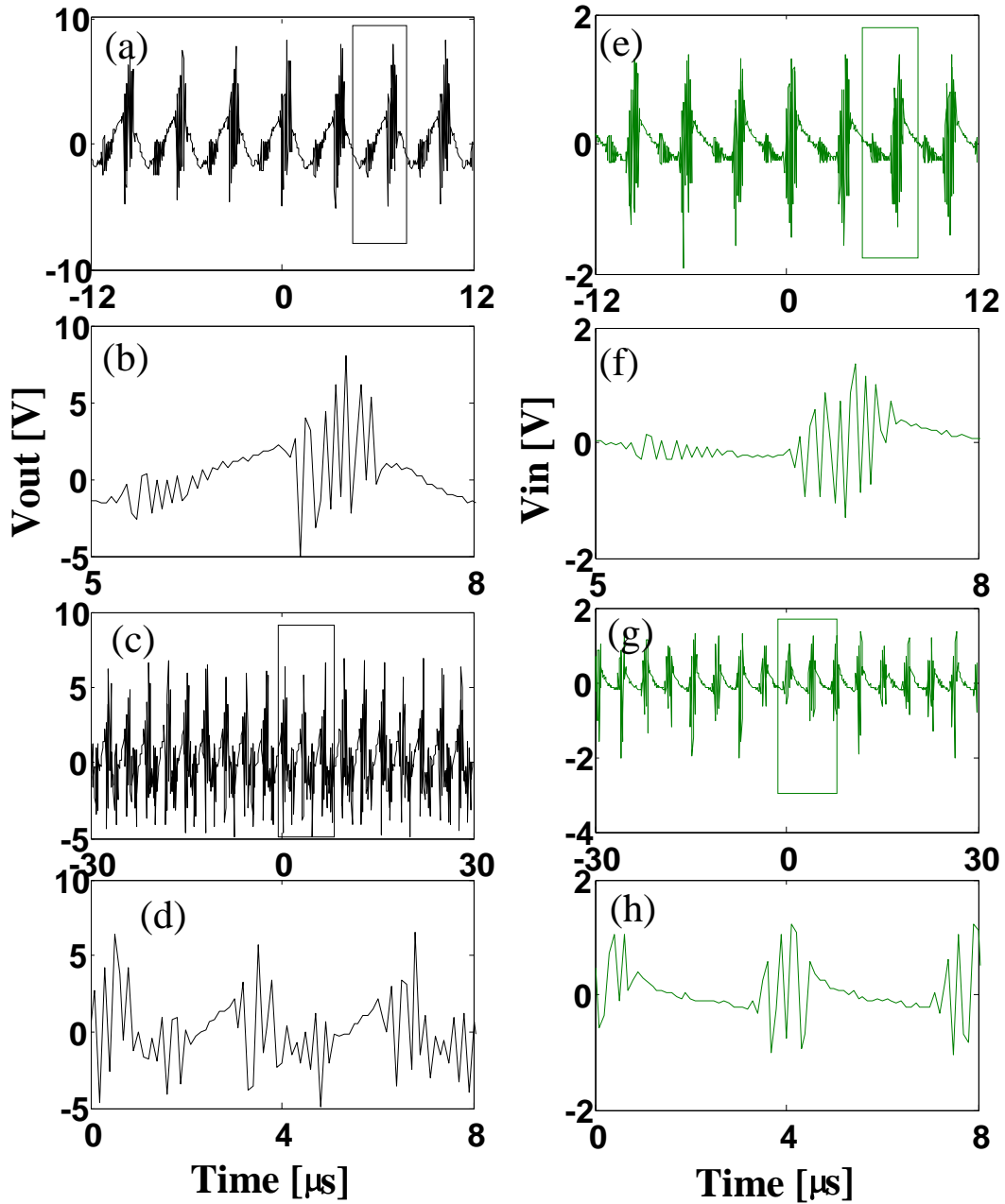
Figure 3.9: *Black color for V_{out} and green color for V_{in}: Experimental time-traces of the OEO-Colpitts oscillator for $T_D = 0$ µs. (a),(e) Bursting, and (c),(g) chaotic bursting oscillations are observed when the polarization voltage is increased beyond the threshold. (a),(e) $V_{pol} = 1.14\ V_{th}$; (c),(g) $V_{pol} = 1.52\ V_{th}$. (b),(f)and (d),(h) are the enlargements of (a),(e) and (c),(g) respectively.*
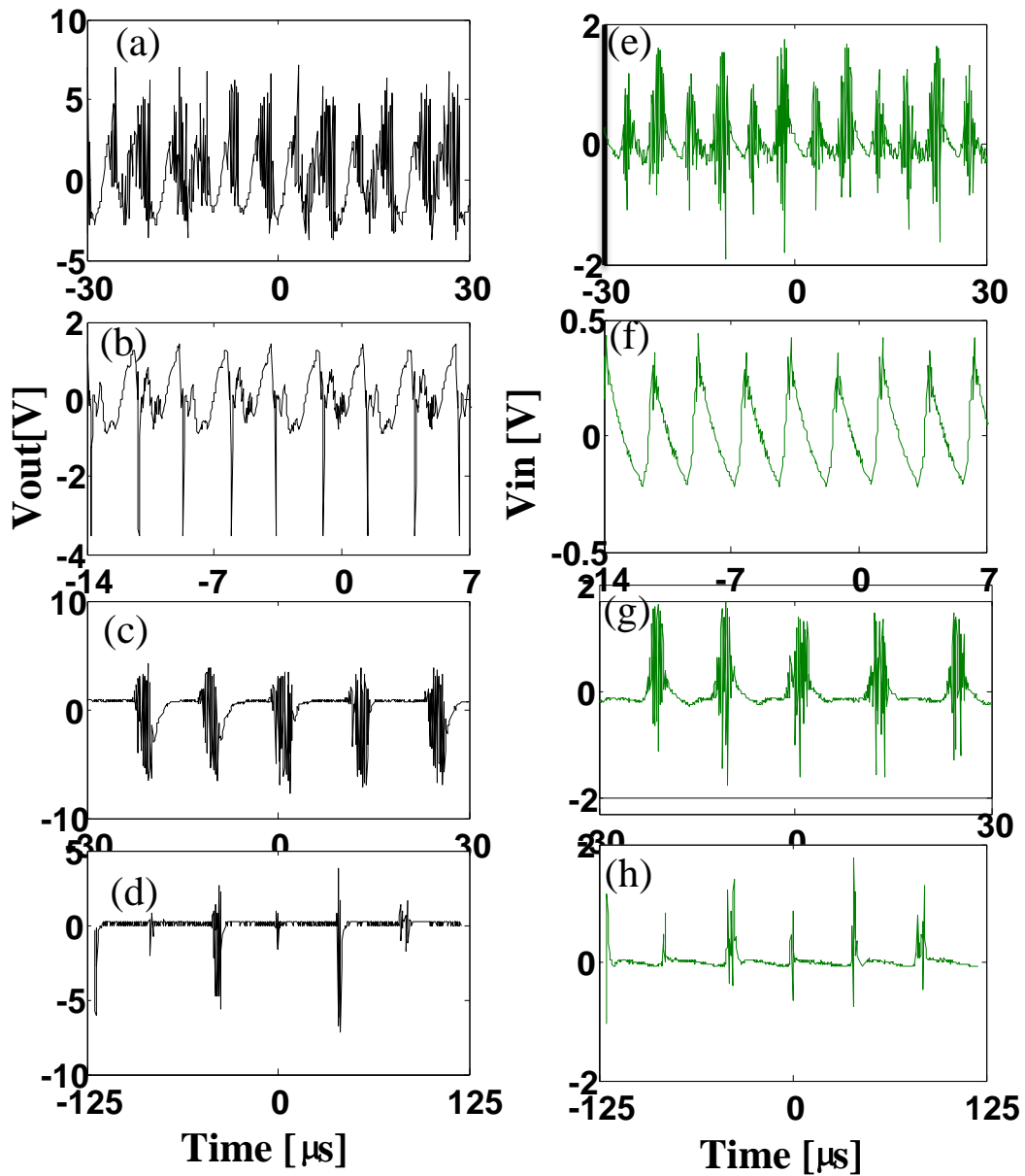
Figure 3.10: Black color for V_{out} and green color for V_{in}: From chaos to chaotic bursting oscillations. The laser pump voltage is increased beyond the threshold ($T_D = 0.2$ μs); (a),(e) chaos for $V_{pol} = 1.12$ V_{th}; (b),(f) Multi-periodic for $V_{pol} = 1.4$ V_{th}; (c),(g) beginning of the chaotic bursting for $V_{pol} = 1.6$ V_{th}; (d),(h) full chaotic bursting for $V_{pol} = 1.74$ V_{th}.

ii) Case with the bursting oscillation of the Colpitts oscillator (R4 = 105 Ω)

In this case, similar work is done as in previous section but, the only difference is that the solitary Colpitts oscillator is configured to emit bursting oscillations. For the case where the time-delay is set to zero ($T_D = 0$ μs), firstly for the value of the polarization voltage just

beyond the threshold, the bursting oscillations are observed (**figure 3.9 (a),(e)** for the two voltages) with the oscillation frequency corresponding to one of the bursting oscillations of the solitary Colpitts oscillator (2.5 *MHz*). In this case, one can observe that the maximum amplitude of the system is equal to 8.2 *V* for V_{out} and 1.4 *V* for V_{in}. These bursting oscillations are characterized by an alternation of two different oscillation packages separated by some fast-scale dynamics. Furthermore, chaotic bursting oscillations (see **figure 3.9 (c),(g)**) are obtained when the polarization voltage increases. The enlargements observed in **figure 3.9 (b),(d)** for V_{out} and (f),(h) for V_{in} display the inner structures of each package of bursting and chaotic bursting oscillations of **figure 3.9 (a),(c) and (e),(g)**, respectively.

Besides, when the delay line is added ($T_D = 0.2$ *μs*) in the system, the dynamical behavior which is initially chaotic (see **figure 3.10 (a),(e),** for the two voltages) migrates towards multi-periodic oscillation (**figure 3.10 (b),(f)**). The maximum frequency corresponding to this multi-periodicity is equal to 195 *kHz* with a maximum amplitude of 1.4 *V* for V_{out} and 0.45 *V* for V_{in}. Finally, the system returns to a chaotic state (chaotic bursting **figure 3.10 (c),(g) and (d),(h)**) in V_{out} and V_{in} when the polarization voltage is increased. The main difference between the cases without and with the delay line is that one has only bursting oscillation with a maximum amplitude equal to 8.2 *V* and chaotic bursting oscillation in the first case; but, the multi-periodic oscillation with a maximum amplitude equal to 1.4 *V* is also observed in the second case for the V_{out} of the system.

3.3 Power spectrum analysis of the dynamics of time-delayed optoelectronic oscillators with wide and narrow band nonlinear filters

In this section, we report on the power spectrum analysis of the phenomena of multi-periodicity, crenelated, mixed-mode oscillations, and chaos when the values of the bandwidth and the cubic-nonlinear term (*CNT*) of the filter vary in the cubic-nonlinear optoelectronic oscillator (*CN-OEO*) (**figure 2.2**).

Combining both Kirchhoff's laws and the general modeling of the *OEO*, the whole system of **figure 2.2** is ruled by the integro-differential delayed equation [67]: see **section 2.5** for the global equation of the *CN-OEO* system.

Throughout this thesis, except for the tunable parameters G, L, and P_{in}, we consider the following values of the key parameters [67]-[68] contained in **Table 2**:

Table 2: Values of the CN-OEO system components.

Designation	Components	Values
Resistor	R	2.5 kΩ
Resistor	R	300 Ω
Capacitor	C_1	270 Pf
half-wave voltage (RF)	$V_{\pi rf}$	3.9 V
half-wave voltage (DC)	$V_{\pi dc}$	5 V
Time-delay	T_D	3.28 µs
Responsivity	S	4.75 V/Mw
Saturation current	I_S	5 µA
Thermal voltage	V_T	25 Mv
Capacitor	C_2	9.15 Nf

The fixed point (x_0, y_0) of **equations (2.39)** and **(2.40)** yields $x_0 = 0$ and y_0 satisfying the third-order polynomial

$$\rho y_0^3 + y_0 + \beta \cos^2 \phi = 0. \tag{3.1}$$

which is nontrivial if β or φ is different from *0* or *π/2 (mod [2π])*, respectively. It is important to mention that y_0 is real and unique since ρ and β are positive quantities.

As the gain evolves, Hopf bifurcation can occur at

$$\gamma_H = \beta_H \sin(2\phi) \tag{3.2}$$

and the system exhibits limit-cycle oscillations with frequency ω_H such that [68]:

$$\omega_H = \sqrt{\frac{\frac{3}{2}\delta\left(-1 + \sqrt{1 + \frac{4\sigma^3 \xi}{3\delta^2}}\right)}{\sigma^3}} \tag{3.3}$$

at the effective normalized gain

$$\gamma_H = -1 - \frac{(\omega_H \sigma)^2}{2} + \frac{(\omega_H \sigma)^4}{24} \tag{3.4}$$

where $\quad \delta = \varepsilon + \sigma = \frac{1}{\theta}\left(\frac{L}{R} + T_D\right) \quad$ and, $\quad \xi = \left(1 + 3\rho y_0^2\right) \tag{3.5}$

To investigate the effect of the bandwidth of the filter, it is possible to tune either the high or the low cut-off time. It is preferable to deal with the high cut-off time by monitoring the coil since it could not affect other parameters of the system. By doing so, reducing the value of the coil L decreases τ while increasing L increases τ. It is important to note that such change is done respecting the requirement of the wideband OEO $\tau < T_D < \theta$.

The following section deals with the dynamical behavior as well as the corresponding spectrum for different values of the coil.

3.3.1 Effect of the coil on the dynamics of CN-OEO

According to **equation 2.34** changing the coil L modifies the value of the high cut-off time τ and then changes the width of the band-pass filter.

a) Case where *L = 10 μH*

In this subsection, the value of the coil is fixed at $L = 10\ \mu H$, corresponding to a high cut-off time $\tau = 4\ ns$ that is $f_H = 39.8\ MHz$. Besides, the low cut-off time is $\theta = 41\ \mu s$ (i.e $f_L = 3.9\ kHz$). Then the bandwidth is large (39.79 *MHz*). The sub **subsections i)** and **ii)** respectively address the different bifurcation diagrams and their corresponding power spectrafor some values of the *CNT ρ*.

i) Bifurcation diagram

The full bifurcation diagrams and the maximum Lyapunov exponents of the system without (**figures 3.11 (a)** and **(d)**) and with (**figures 3.11 (b)** and **(e)**, and **(c)** and **(f)**) the *CNT* present the various dynamical states that can be obtained as the effective normalized gain $\gamma = \beta \sin(2\phi)$ is varied.
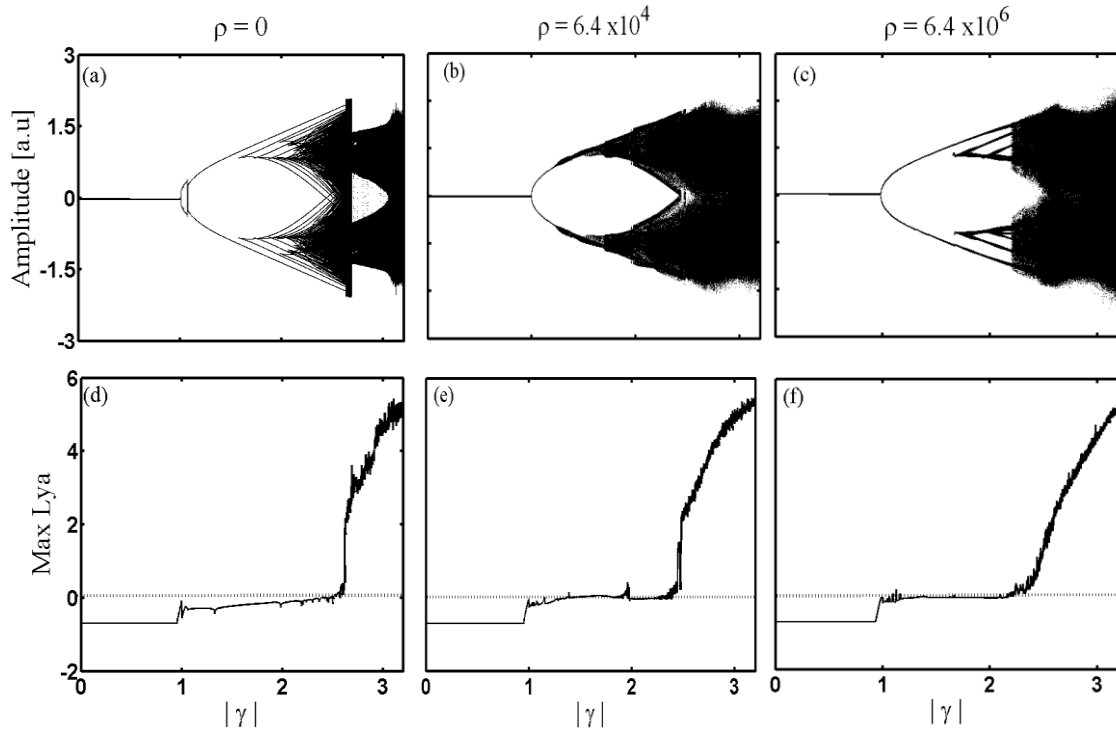
Figure 3.11 : Bifurcation diagrams and maximum Lyapunov exponents of: (a) and (d), the standard OEO (ρ = 0) (i.e. without the cubic-nonlinear term in equation(2.40)); ((b) and (e)) and ((c) and (f)) for the CN-OEO (i.e. with cubic-nonlinear term in equation (2.40) corresponding to ρ = 6.4 ×10⁴ and ρ = 6.4 ×10⁶, respectively). φ = −π/4

The bifurcation diagram (**figure 3.13 (a)**) and the Lyapunov exponent (**figure 3.13 (d)**) of the standard *OEO* (the case with $\rho = 0$) depicts the usual sequence: Fixed point for $|\gamma| \leq 1$; limit-cycles for γ above 1 which frequency decreasing as γ increases; mixed-mode oscillations from $|\gamma| \geq 1.57$. Mixed-mode oscillations also known as breathers are trajectories of a dynamical system in which there is an alternation between oscillations of distinct large and small amplitudes [132,133]. The multiple lines of the bifurcation diagram mark an increase of small amplitude oscillations of these mixed-mode oscillations as the effective normalized gain γ evolves routing to chaos from $|\gamma| \geq 2.5$.

Figures 3.11 (b) and **(e)** show the evolution of the amplitude as the effectively normalized gain increases when the *CNT* $\rho = 6.4 \times 10^4$ is considered in equation 3.12. Periodic oscillation dominates until $|\gamma|$ is close to 2.35. Just above this value, chaotic behavior appears in the system. Compared to the case of **figure 3.11 (a)**, one first observes that the threshold of the effective normalized gain is not considerably affected by the *CNT* ($|\gamma th| = 1$). Secondly, one notes that the region in form of a circular arc observed in the case of standard *OEO* just after the threshold value no longer exists. Thirdly, the chaotic dynamics appears a little

earlier; that is $|\gamma| = 2.35$ for 6.4×10^4 whereas it was $|\gamma| = 2.5$ for $\rho = 0$. When the *CNT* is increased (6.4×10^6), the threshold value of γ remains at $|\gamma th| = 1$. However, the value of γ from which chaos emerges in the system has reduced again; it is now equal to 2.15 (see **figures 3.11 (c)** and **(f)**).

The following sub sub-section analyses the spectra of the signals at different levels of the bifurcation diagrams.

ii) Spectral response

Figure 3.12 shows the times series, the power spectra, and the phase portraits of the standard *OEO* ($\rho = 0$) for different values of the effective normalized gain chosen above the threshold. For instance, $/\gamma/ = 1.05$ (**figures 3.12 a1-a3**), the time series is a relaxation oscillation whose fundamental frequency is about 300 *kHz* corresponding to a region in the form of a circular arc (see **figure 3.11 (a)**) confirmed by a phase portrait showing a slow-fast dynamical limit-cycle. For $/\gamma/ = 1.1$ (**figures 3.12 b1-b3**), another limit-cycle oscillation similar to sinusoid (**figure 3.12 b1**) is observed in the time series, with a fundamental frequency of about 13.75 *kHz* and harmonic frequencies of 27.5 *kHz* and 41.25 *kHz* revealed by the power spectrum. Increasing γ ($/\gamma/ = 1.5$ (**figures 3.12 c1-c3**)), relaxation oscillation reappears in a different form from that obtained when $/\gamma/ = 1.05$ with a lower fundamental frequency (12 *kHz*) and several harmonics. The fundamental frequency is continuously decreasing with the increase of γ as well as the number of harmonics of these fundamental frequencies. Such growth precedes mixed-mode oscillations (see **figures 3.12 d1-d3** for $/\gamma/ = 2.3$). The fundamental frequency of large amplitudes shown in the power spectrum has also been reduced to 8 *kHz*, and the phase portrait reveals that breathers are symmetrical. Finally, when $/\gamma/$ reaches the chaotic region, e.g $/\gamma/ = 2.65$ (**figures 3.12 e1-e3**), one has a flat broadened power spectrum and a phase portrait exhibiting a strange attractor.
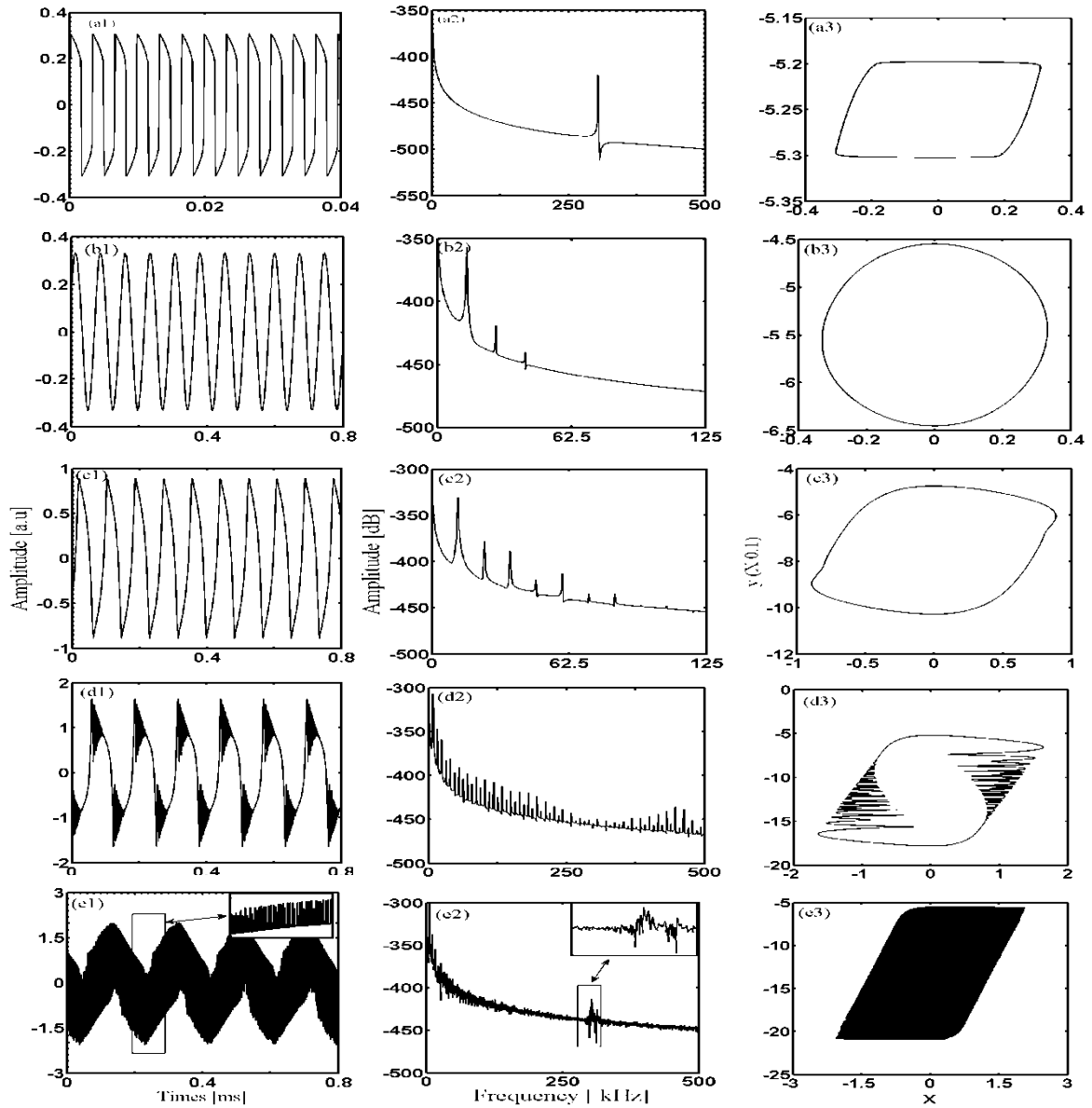
Figure 3.12: Time series (first column), power spectra (second column), and phase portraits (third column) for the standard OEO (ρ = 0) at different values of γ. |γ| = 1.05 (figures 3.12 a1-a3), |γ| = 1.1 (figures 3.12 b1-b3), |γ| = 1.5 (figures 3.12 c1-c3), |γ| = 2.3 (figures 3.12 d1-d3), and |γ| = 2.65 (figures 3.12 e1-e3)

Figure 3.13 displays the time series, the power spectrum, and the phase portraits of this system for different values of the effective normalized gain above the threshold when the *CNT* is different from zero ($ρ = 6.4 \times 10^4$). For $|γ| = 1.05$ (**figures 3.13 a1-a3**), the time series exhibit a limit-cycle oscillation where the fundamental frequency f_0 is about 2.1 *MHz* corresponding to the peak of larger amplitude. The two other peaks of the spectrum are equally distant from the fundamental frequency with a spacing equal to the inverse of the time

delay ($1/T_D = 303$ kHz). Furthermore, we can also observe side lobes that appear periodically indicating multiples of the comb spacing frequency $\kappa \times 1/T_D$ where κ is a strictly positive integer. This frequency $\Omega_{FSR}/2\pi = 1/T_D = 303$ kHz is also called the free spectral range [134]. The single-phase portrait loop confirms the time series. When the effective normalized gain is increased, ($/\gamma/ = 1.5$ for **figures 3.13 b1-b3**), the time series show relaxation oscillations which are alternate. The fundamental frequency is now about $f_0 = 1.2$ MHz. The power spectrum also displays frequency combs. As can be seen, with the increase of γ, the energy in different harmonics is being redistributed more evenly and the phase portrait shows a limit-cycle of several lines. When $/\gamma/=2$ (**figures 3.13 c1-c3**), in the time series, one can note that the system displays mixed-mode oscillations with modulated amplitude. The power spectrum shows a curve similar to the previous case, with the same fundamental frequency but, a slightly larger amplitude is observed. When the value of the effective normalized gain increases ($/\gamma/ = 2.3$ for **figures 3.13 d1-d3**), the mixed-mode oscillations with modulated amplitude become important and crenelated oscillation occurs. Crenelated oscillation displays two types of dynamics: the slow dynamics characterized by square oscillations of the plateau and the fast dynamics representing the oscillations inside the plateau. The power spectrum indicates the fundamental frequency at a value of 1.5 MHz but with multiple peaks. The phase portrait shows the form of oscillations contained in each dynamics. For higher values of γ, the system exhibits a chaotic behavior (**figures 3.13 e1-e3** for $/\gamma/ = 3.1$).

For the following case, we increase the value of the *CNT* to $\rho = 6.4 \times 10^6$. The results are displayed in **figure 3.14**. Topologically, one can witness that as γ increases, the system exhibits dynamic features similar to the case where $\rho = 6.4 \times 10^4$ (see **figure 3.13**). That is the evolution from limit-cycle oscillation at an early value of γ ($/\gamma/ = 1.05$ and $/\gamma/ = 1.5$ for **figures 3.14 a1-a3** and **figures 3.14 b1-b3**, respectively) then, mixed mode oscillations ($/\gamma/ = 2$ for **figures 3.14 c1-c3**), crenelated oscillations ($/\gamma/ = 2.5$ for **figures 3.14 d1-d3**), and finally chaotic behavior ($/\gamma/ = 3.1$ for **figures 3.14 e1-e3**). Moreover, limit cycle oscillations present packages of frequency combs with the same combs spacing (303 *kHz* = $1/T_D$ and see **figures 3.14 b2** and **c2**) i.e same free spectral range as in the case where $\rho = 6.4 \times 10^4$. Nevertheless, it is important to notice that the differences are at the level of the fundamental oscillation frequencies ($f_0 = 5.8$ *MHz*, $f_0 = 4.3$ *MHz*, and $f_0 = 3.7$ *MHz* for $\rho = 6.4 \times 10^6$ against $f_0 = 2.1$ *MHz*, $f_0 = 1.2$ *MHz*, and $f_0 = 1.2$ *MHz* for $\rho = 6.4 \times 10^4$ when $/\gamma/ = 1.05$, $/\gamma/ = 1.5$, and $/\gamma/ = 2$, taken respectively for the two cases) and the spectrum envelope (when the value of γ increases, the envelope of the spectrum keeps the same shape in the limit-cycle oscillations

and whose fundamental frequency remains the only peak of great amplitude for the case $\rho = 6.4 \times 10^6$).

Figure 3.13: Time series (first column), power spectra (second column), and phase portraits (third column) for the CN-OEO ($\rho = 6.4 \times 10^4$) at different values of γ. $|\gamma| = 1.05$ (figures 3.13 a1-a3), $|\gamma| = 1.5$ (figures 3.13 b1-b3), $|\gamma| = 2$ (figures 3.13 c1-c3), $|\gamma| = 2.3$ (figures 3.13 d1-d3), and $|\gamma| = 3.1$ (figures 3.13 e1-e3).

83
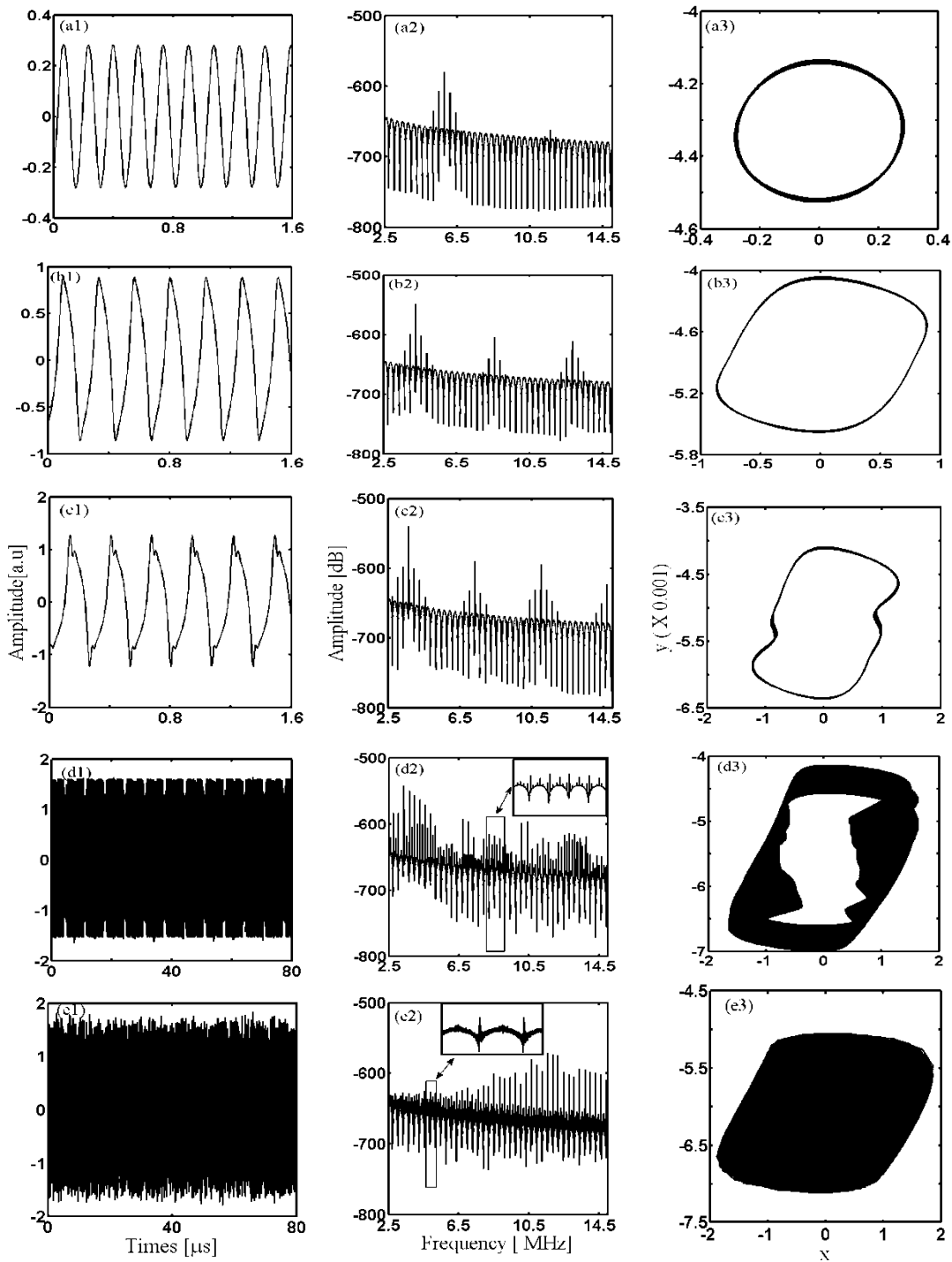
Figure 3.14: *Time series (first column), power spectra (second column), and phase portraits (third column) for the CN-OEO ($\rho = 6.4 \times 10^6$) at different values of γ. $|\gamma| = 1.05$ (figures 3.14 a1-a3), $|\gamma| = 1.5$ (figures 3.14 b1-b3), $|\gamma| = 2$ (figures 3.14 c1-c3), $|\gamma| = 2.5$ (figures 3.14 d1-d3), and $|\gamma| = 3.1$ (figures 3.14 e1-e3).*
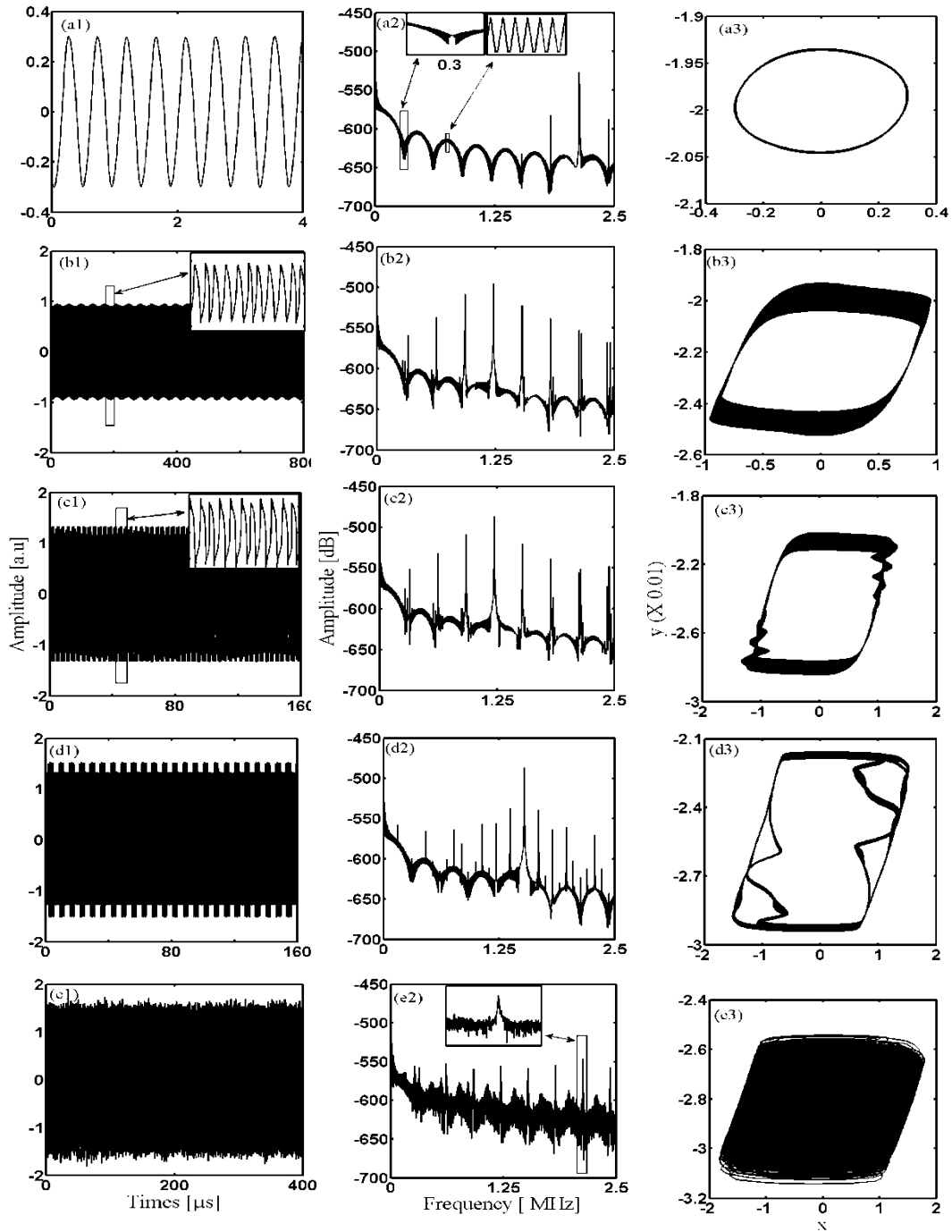
In either case, the frequency combs are observed in the presence of the *CNT* and are characterized mainly by their *k*-th frequency components f_k given by $f_k = f_0 + k \cdot 1/T_D$, where f_0 is the fundamental frequency corresponding to the frequency associated with the phase shift between two successive laser pulses, $1/T_D = \Omega_{FSR}/2\pi = 303\ kHz$ is the free spectral range [135].

The following section consists of increasing the value of the coil. This increase brings the two cut-off times closer.

b) Case where *L = 10 mH*

In this part, the procedure is similar to that done in **subsection 3.3.1.a)** with the difference that only the value of the coil is modified and is taken equal to $L= 10\ mH$. It results that, the value of the high cut-off time is $\tau = 4\ \mu$s and the low cut-off time $\theta = 41\ \mu$s corresponding to respective frequencies $f_H = 39.8\ kHz$ and $f_L = 3.9\ kHz$. Thus, the bandwidth is narrow equal to 35.9 *kHz*. Several other phenomena and dynamic behaviors might occur in the system.

i) Dynamical behaviors

To better appreciate the frontiers between the different dynamical regimes of the standard *OEO* and *CN-OEO*, numerical bifurcation diagrams, and their corresponding maximum Lyapunov exponents are plotted in **figure 3.15**. For three cases $\rho = 0$, $\rho = 6.4 \times 10^4$, and $\rho = 6.4 \times 10^6$, these bifurcation diagrams and Lyapunov exponents qualitatively display similar results. That is the dynamics globally commence with fixed-point followed by a Hopf-bifurcation characterized by limit-cycle oscillations which dwell until a certain value of the bifurcation parameter, where mixed-mode oscillations and period-doubling take place; the further increase of the bifurcation parameter leads the system into chaotic motions (see **figure 3.15** and **figure 3.11** for some value of ρ, respectively). However, there are several important differences that merit being underlined. The first one is about the order of the values of γ in the bifurcation diagram. The order of γ in the bifurcation diagram for $L = 10\ mH$ is higher compared to the case of $L= 10\ \mu H$ for the same value of the *CNT*. Consequently, the threshold value for the Hopf bifurcation is larger. When $L= 10\ \mu$H, $/\gamma$th$/$ conserved the same value of the threshold $(/\gamma$th$/ = 1)$ no matter the value of ρ (see figure 3.13). But, **figure 3.15** shows that $/\gamma$th$/ = 1$ for $\rho = 0$, $/\gamma$th$/ = 3.36$ for $\rho = 6.4 \times 10^4$, and $/\gamma$th$/ = 1.3$ for $\rho = 6.4 \times 10^6$. Besides, the *CNT* makes the chaotic dynamics occurring a little later (in **figure 3.15**, $/\gamma/ = 5.85$

for $\rho = 0$, $|\gamma| = 9.2$ for $\rho = 6.4 \times 10^4$ and $|\gamma| = 12.3$ for $\rho = 6.4 \times 10^6$). The second thing to underline concerns the case where $\rho = 6.4 \times 10^6$. Comparing **figures 3.11 (c)** and **(f)** and **figures 3.15 (c)** and **(f)**, it is remarkable that the routes to chaos are different. Mixed-mode oscillations are not pronounced in **figure 3.15 (c)** and chaos arise almost abruptly through a crisis phenomenon.

The next section consists of taking some values of the effective normalized gain above the threshold value and observing the response of the system from the spectral point of view.
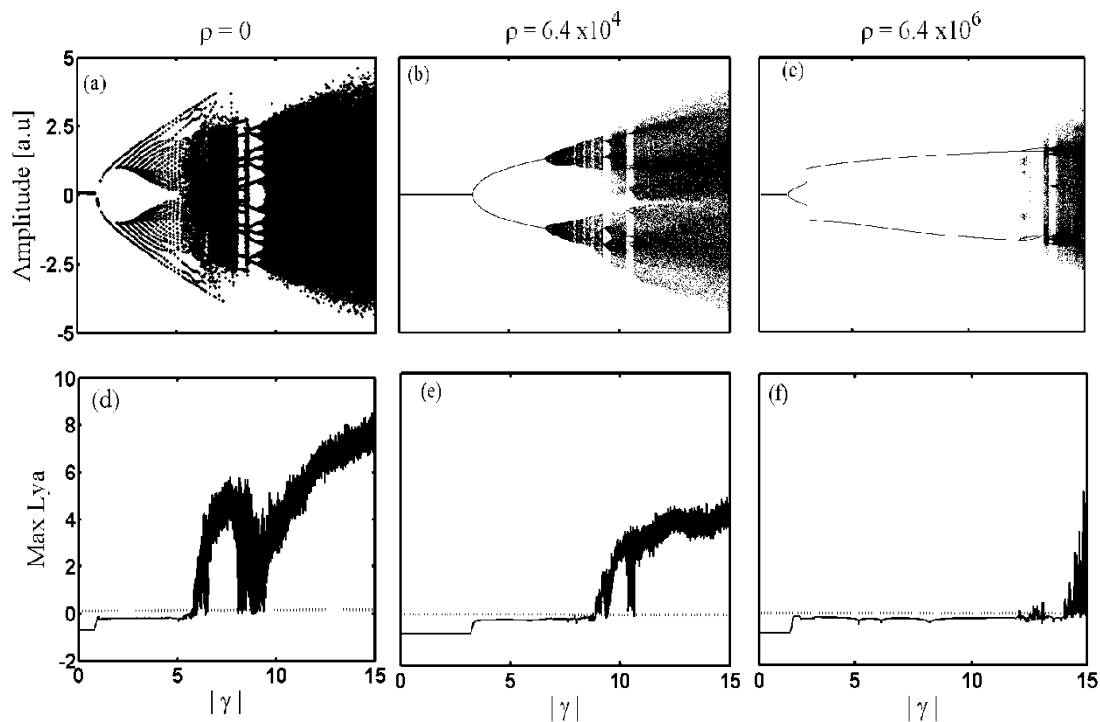
Figure 3.15: Bifurcation diagrams and maximum Lyapunov exponents of: (a) and (d), the standard OEO ($\rho = 0$) (i.e. without cubic term in equation (2.40)); ((b) and (e)) and ((c) and (f)), the CN-OEO (i.e. with cubic term in equation (2.40) corresponding to $\rho = 6.4 \times 10^4$ and $\rho = 6.4 \times 10^6$, respectively). $\varphi = -\pi/4$.

ii) Spectral response

For the first case where the coefficient of the *CNT* is zero (standard *OEO*), our simulation shows some spectral states corresponding to each dynamical behavior that we can observe in **figure 3.16**. Thus, taking a value of γ just above the threshold $|\gamma| = 1.05$ (**figures 3.16 a1-a3**), a limit-cycle oscillation occurs in the time series and whose fundamental frequency is equal to 9.5 *kHz,* and its harmonic (19 *kHz* and 28.5 *kHz*) as can be seen in the Fourier spectrum. The trajectories of the phase portrait show a clear limit cycle. For $|\gamma| = 1.5$

(**figures 3.16 b1-b3**), the system rather exhibits relaxation oscillation whose fundamental frequency is now equal to 8.25 *kHz* and several other harmonics appear in the power spectrum where their intensity decreases until they completely attenuate. When $/\gamma/$ is further increased ($/\gamma/$ = 4.8 (**figures 3.16 c1-c3**)), the system now displays mixed-mode oscillations whose maximum amplitude of oscillations is equal to 2.7 and the power spectrum indicates their fundamental frequency at a value equal to 3.5 *kHz*. Small amplitude oscillations are symmetrical as shown in the phase portrait. An increase in the effective normalized gain ($/\gamma/$ = 6.3 for **figures 3.16 d1-d3**) drives the system in a regime of chaotic mixed-mode oscillations. Here, no obvious peak can be observed in the power spectrum. When $/\gamma/$ is increased to 9.1 (**figures 3.16 e1-e3**), the chaotic state disappears and the system behaves with a multi-periodic oscillation whose fundamental frequency is about 42.5 *kHz*. Finally, when $/\gamma/$ is taken above the value of 9.5, the system completely goes back into a chaotic state (see **figures 3.15 (a) and (d)**).
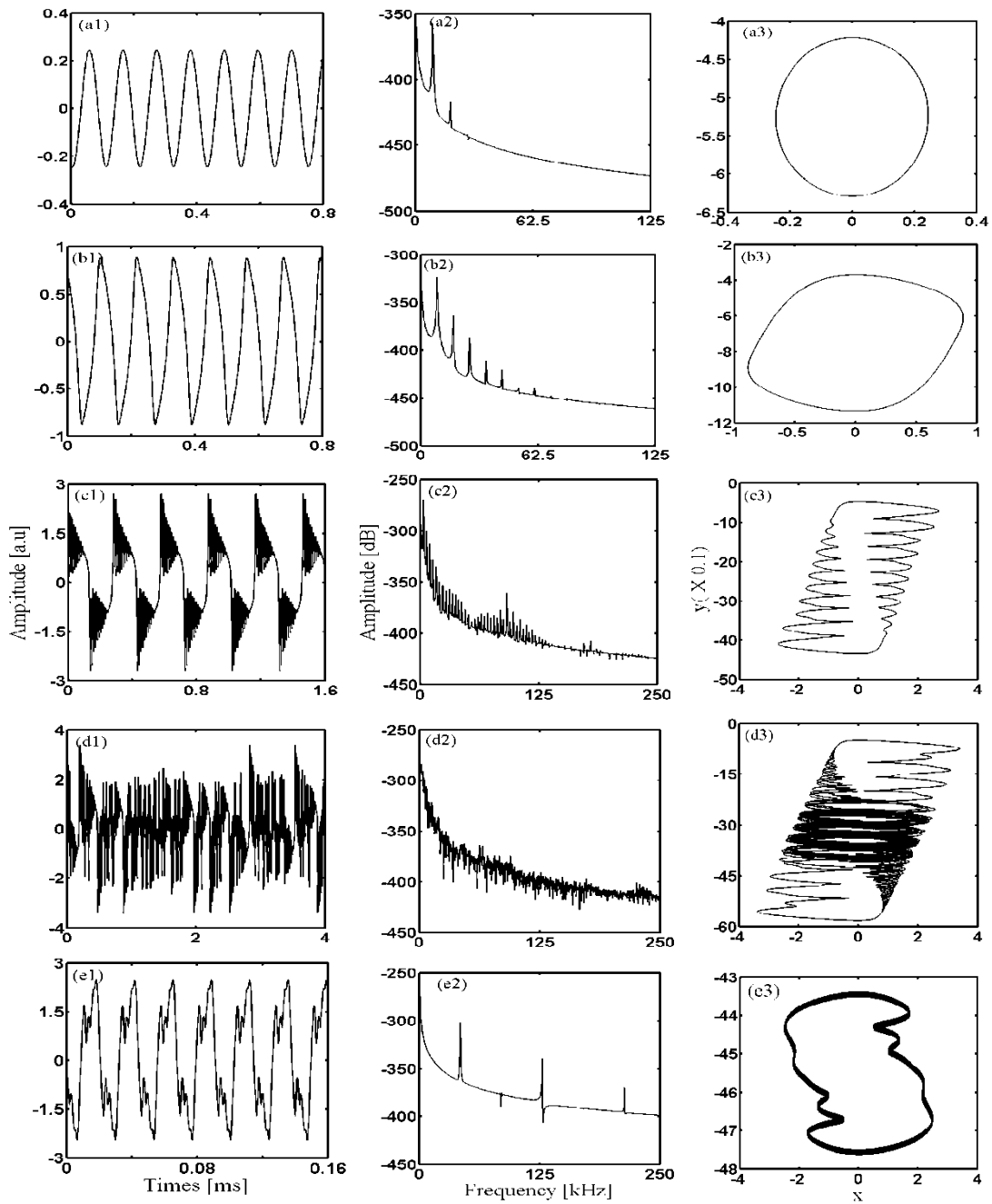
Figure 3.16: Time series (first column), power spectra (second column), and phase portraits (third column) for the standard OEO (ρ = 0) at different values of γ. |γ| = 1.05 (figures 3.16 a1-a3), |γ| = 1.5 (figures 3.16 b1-b3), |γ| = 4.8 (figures 3.16 c1-c3), |γ| = 6.3 (figures 3.16 d1-d3), and |γ| = 9.1 (figures 3.16 e1-e3).

Figure 3.17 shows the dynamic behavior and the corresponding power spectra for some values of the effective normalized gain when the *CNT* is $\rho = 6.4 \times 10^4$. For this case, the threshold value of the effective normalized gain is obtained for a value equal to 3.36. Taking the value of the effective normalized gain equal to 3.45 (**figures 3.17 a1-a3**), the almost sinusoidal oscillation is produced. The related power spectrum indicates that the fundamental

frequency is about 245 *kHz* and a harmonic equal to 490 *kHz*. For / γ/ = 8.8 (**figures 3.17 b1-b3**), the periodic waveform with fourteen distinct peak intensities is shown in the time series, the sub-harmonic frequency appears in the power spectrum whose the first is about 17.5 *kHz* i.e the fundamental frequency (245 *kHz*) divided by fourteen and the corresponding phase portrait shows also fourteen loops that are intertwined together. When / γ/ is increased (/ γ/ = 9.7 for **figures 3.17 c1-c3**), the peak intensities of the time series behave as an irregular fluctuation, the associated power spectrum broadens, and the phase portrait exhibits a strange attractor. For / γ/ = 10.5 (**figures 3.17 d1-d3**), the chaotic dynamic state previously observed disappears and a 3-T period oscillation is shown in the system. Three peaks with different intensities emerge in the time series, the sub-harmonic frequency appears in the power spectrum whose first is about 84 *kHz* (the fundamental frequency divided by three). The corresponding phase portrait shows three loops. As the effective normalized gain is increased (/ γ/ = 12 for **figures 3.17 e1-e3**), chaotic dynamics are definitely observed.

Now, we increase the value of the *CNT* to $\rho = 6.4 \times 10^6$ and the results are shown in **figure 3.18**. Compared to the case where $\rho = 6.4 \times 10^4$ (**figure 3.17**), the system presents different ranges of the effective normalized gain but one can attest to a similarity, namely that the route to chaos is made only through the period-doubling (of different periods). However, it is more interesting to notice some differences summarized in **Table 3**. Indeed, **table 3** reveals that for a value just above the threshold value of γ ($\gamma = 3.45$ for $\rho = 6.4 \times 10^4$ and $\gamma = 1.5$ for $\rho = 6.4 \times 10^6$), one notices a period-1 dynamics for both cases (see lines 2 and 7). On the other hand, while one observes changes in the fundamental frequency, harmonics, and sub harmonics frequencies for $\rho = 6.4 \times 10^4$ when γ varies from 3.45 to 10.5 (see lines 2, 3, 4, 5 and **figure 3.15 (b)**), the dynamic behavior for the case where $\rho = 6.4 \times 10^6$ remains at one period for practically the same range of the variation of γ (1.5 to 10.8: see lines 7, 8 and **figure 3.15 (c)**). The chaotic dynamics occur a little far when the value of the *CNT* ρ passes from $\rho = 6.4 \times 10^4$ to $\rho = 6.4 \times 10^6$ (see lines 4, 6, and 10). Another difference is that when the *CNT* passes from $\rho = 6.4 \times 10^4$ to $\rho = 6.4 \times 10^6$, the side lobes appear in the power spectrum.

Figure 3.17: Time series (first column), power spectra (second column), and phase portraits (third column) for the CN-OEO ($\rho = 6.4 \times 10^4$) at different values of γ. $|\gamma| = 3.45$ (figures 3.17 a1-a3), $|\gamma| = 8.8$ (figures 3.17 b1-b3), $|\gamma| = 9.7$ (figures 3.17 c1-c3), $|\gamma| = 10.5$ (figures 3.17 d1-d3), and $|\gamma| = 12$ (figures 3.17 e1-e3).

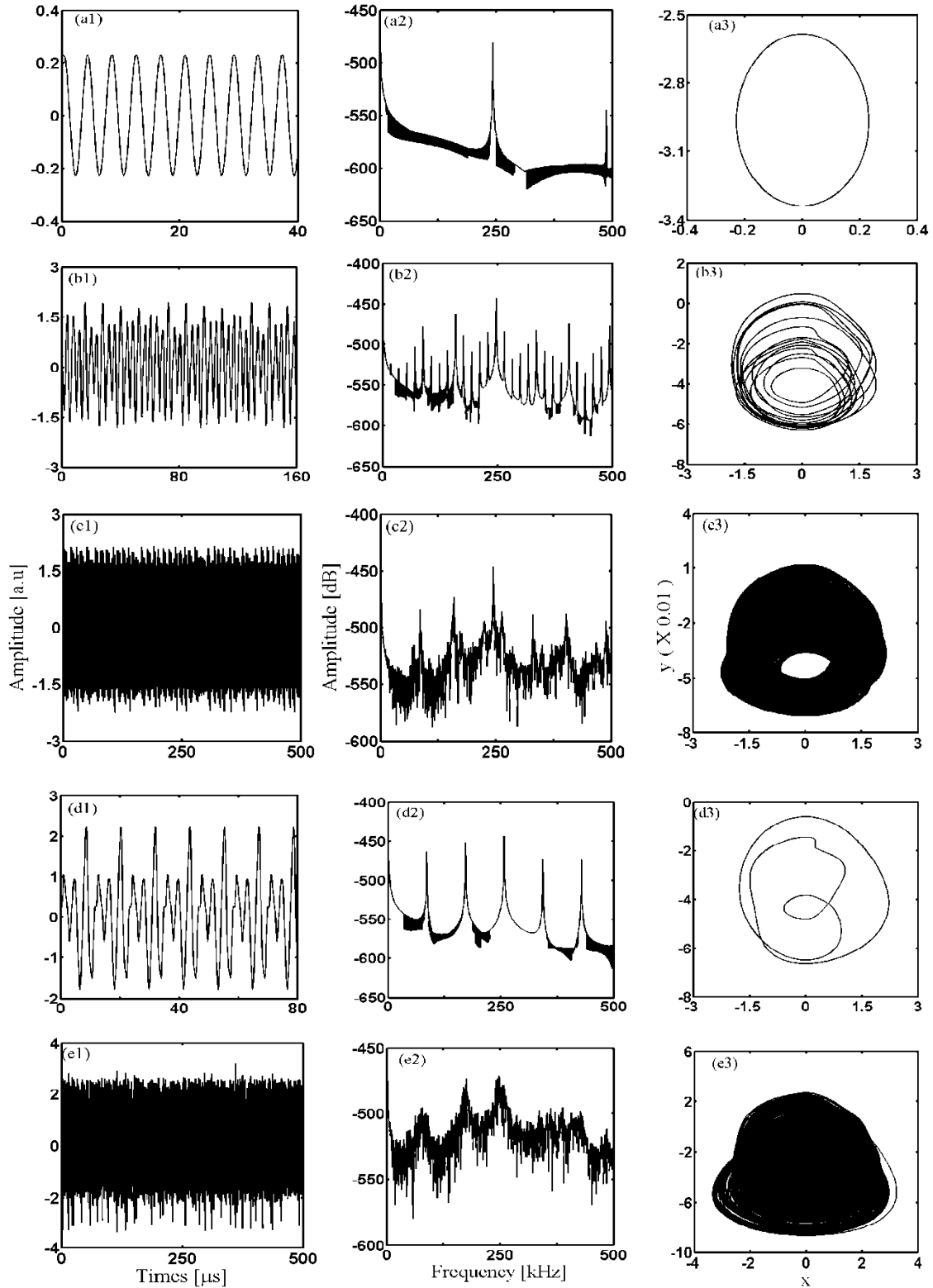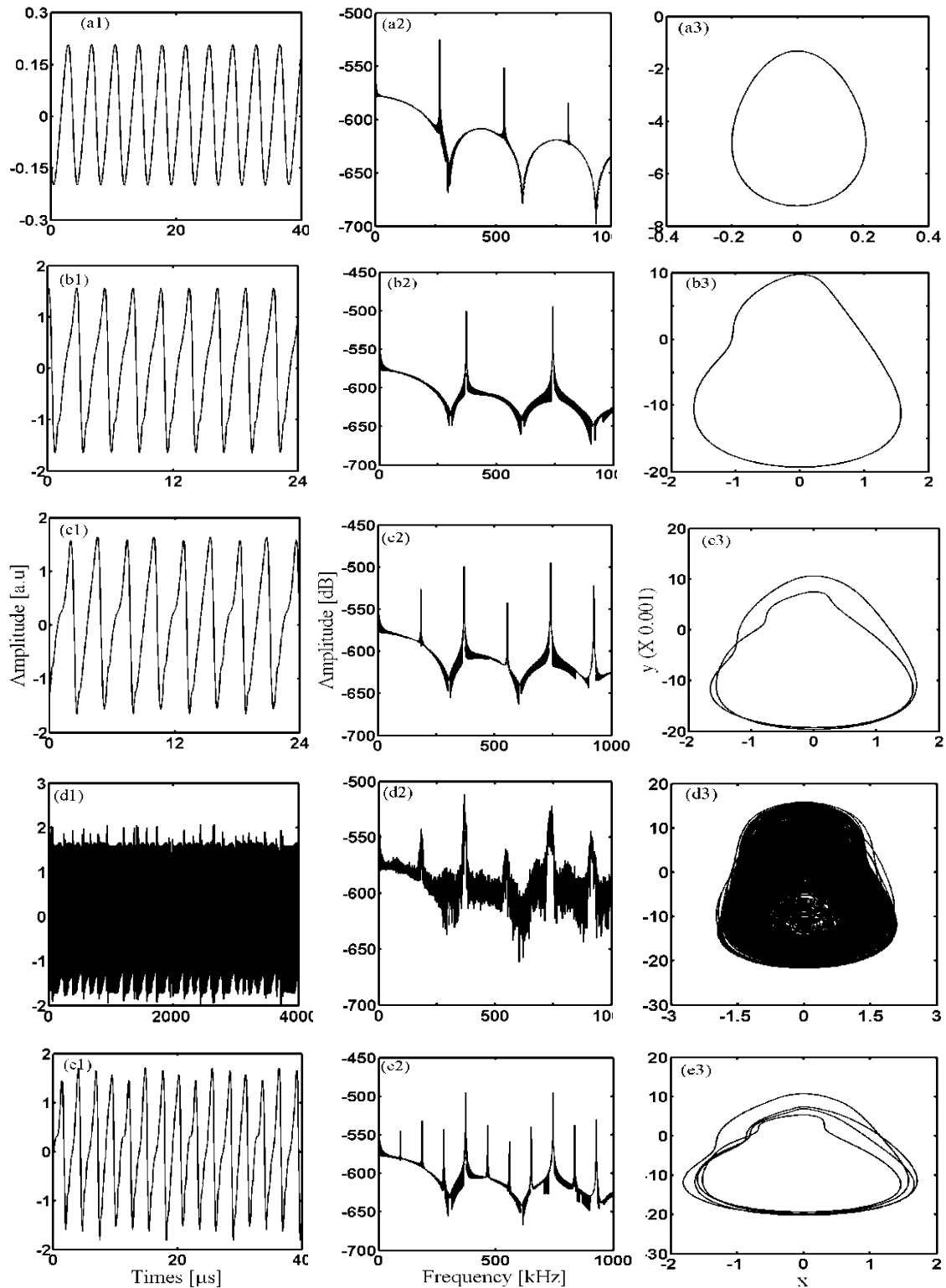*Figure 3.18: Time series (first column), power spectra (second column), and phase portraits (third column) for the CN-OEO ($\rho = 6.4 \times 10^6$) at different values of γ. $|\gamma| = 1.5$ (figures 3.18 a1-a3), $|\gamma| = 10.8$ (figures 3.18 b1-b3), $|\gamma| = 11.8$ (figures 3.18 c1-c3), $|\gamma| = 12.5$ (figures 3.18 d1-d3), and $|\gamma| = 13.5$ (figures 3.18 e1-e3).*

Table 3: Some differences with the increase of the effective normalized gain in presence of the cubic-nonlinear term when L=10 mH. (F.F: Fundamental Frequency; F.S.H: First Sub-Harmonic; F.H: First Harmonic).

$|\gamma|$	ρ	Dynamics (number of periods)	F.F (kHz)	F.S.H (kHz)	F.H (kHz)	**Figures**
3.45	6.4×10^4	Periodic (One)	245	None	490	**3.17**
8.8	6.4×10^4	Periodic (fourteen)	245	17.5	262.5	**3.17**
9.7	6.4×10^4	Chaos	None	None	None	**3.17**
10.5	6.4×10^4	Periodic (three)	252	84	336	**3.17**
12	6.4×10^4	Chaos	None	None	None	**3.17**
1.5	6.4×10^6	Periodic (One)	265	None	530	**3.18**
10.8	6.4×10^6	Periodic (One)	370	None	740	**3.18**
11.8	6.4×10^6	Periodic (two)	370	185	555	**3.18**
12.5	6.4×10^6	Chaos	None	None	None	**3.18**
13.5	6.4×10^6	Periodic (four)	360	90	450	**3.18**

3.3.2 Influence of the cubic-nonlinear coefficient on the selectivity of characteristic peaks

This section shows the influence of the *CNT* on the central peak when the value of the coil and that of the effective normalized gain taken just above the threshold value are maintained fixed. From this **figure 3.19**, when ρ increases (black to blue in **figure 3.19**), the appearance of low-intensity peaks around the central peak shows a kind of translation toward the smaller intensities. Besides, that reduction in intensity is accompanied by a narrowing in the width of the central peak. The fact that the width of the central peak narrows with the

increase of ρ demonstrates that the system becomes more and more selective in terms of oscillation frequencies.
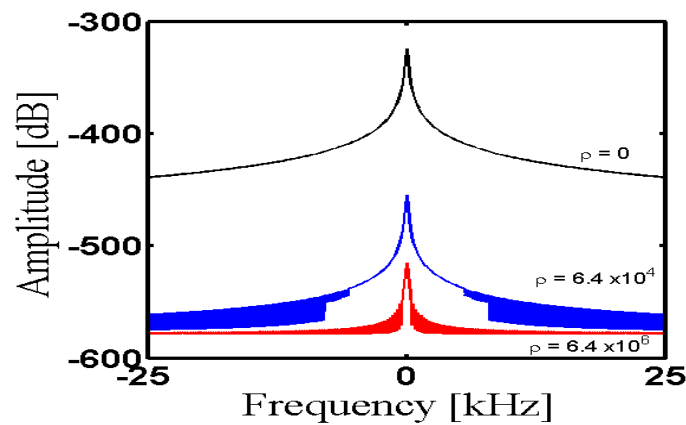
Figure 3.19: Power spectra: black for $\rho = 0$, - blue for $\rho = 6.4 \times 10^4$, and - red when the value of the cubic-nonlinear term increases ($\rho = 6.4 \times 10^6$). For these three cases, L=10 μH, and the value of the effective normalized gain remains the same $|\gamma| = 1.05$.

3.4 Conclusion

In this chapter, we have presented the results of our work. In the first part, we firstly studied numerically and experimentally the self-sustaining Colpitts oscillator. This allowed us to determine some characteristics of this oscillator (output voltage, its frequency) and to show that it can exhibit dynamic behaviors such as limit-cycle oscillations, mixed-modes, and bursting oscillations depending on the value of the potentiometer contained in the circuit. We noticed a good agreement between our results on the Multisim software, our numerical simulations, and the experimental results. Secondly, we inserted this self-sustaining Colpitts oscillator into the electrical part of the *OEO*. We put into competition three parameters of the system, namely the power of the laser diode, the potentiometer of the Colpitts oscillator, and the delay across the length of the optical fiber. It is shown that a wide variety of periodic and chaotic states can be excited and also that there is an amplification of the signal frequencies. In particular, bursting, chaotic bursting, and chaotic pulse package oscillations with slow-fast temporal dynamics are experimentally observed in the system. This study has shown that coupling a non-linear self-sustaining oscillator to a photonic oscillator provides dynamic behaviors that open the door to new applications such as neuromorphic computing. In the second part, we have done a power spectrum analysis of timed-delayed optoelectronics oscillators with wide and narrow band nonlinear filters. We have mainly focused on the

frequency characterization of the cubic-nonlinear optoelectronic oscillator (*CN-OEO*). The effects of two main parameters have been investigated: the high cut-off time through the coil *L* and the cubic-nonlinear term ρ. It has appeared that these terms affect the system from the dynamical and spectral points of view. Firstly, when the value of the coil has been fixed at *10 μH* (wideband *CN-OEO*), the results have shown that the presence and the increase of the cubic-nonlinear term do not affect the threshold value of the effective normalized gain (always equal to 1), but chaotic dynamics occurs at earlier values of the effective normalized gain when the nonlinear parameter increases ($|\gamma| = 2.5$, $|\gamma| = 2.35$, and $|\gamma| = 2.15$ for $\rho = 0$, $\rho = 6.4 \times 10^4$, and $\rho = 6.4 \times 10^6$, respectively). The bifurcation diagram has also shown that the dynamics of the *CN-OEO* are essentially dominated by limit-cycle oscillations and chaotic states. Also, we have observed a very large increase in the fundamental frequency (300 *kHz* for $\rho = 0$, 2.1 *MHz* for $\rho = 6.4 \times 10^4$, and 5.8 *MHz* for $\rho = 6.4 \times 10^6$ when $\gamma = 1.05$ for the three cases) and the increase of the cubic-nonlinear term reduces the number of admitted oscillation modes in the system. Same for this case, the presence of the cubic-nonlinear term makes the *CN-OEO* like a high (in the range of *MHz*) frequency combs generator with a free spectral range equal to 303 *kHz* corresponding to the value of the inverse of the time-delay $1/T_D$. Secondly, when the value of the coil has been increased and fixed at *10 mH* (narrow band *CN-OEO*), it was observed that the cubic-nonlinear term, however, influences the threshold value of the effective normalized gain (1 for $\rho = 0$, 3.36 for $\rho = 6.4 \times 10^4$, and 1.3 for $\rho = 6.4 \times 10^6$). Then, from the dynamical point of view, chaotic dynamics occurs a little far ($|\gamma| = 5.85$ for $\rho = 0$, $|\gamma| = 9.2$ for $\rho = 6.4 \times 10^4$, and $|\gamma| = 12.3$ for $\rho = 6.4 \times 10^6$). In this case (*L=10 mH*), we have also noted an increase in the fundamental frequency for the values of the effective normalized gain taken just above each threshold (9.5 *kHz* for $\rho = 0$ when $|\gamma| = 1.05$, 245 *kHz* for $\rho = 6.4 \times 10^4$ when $|\gamma| = 3.45$, and 265 *kHz* for $\rho = 6.4 \times 10^6$ when $\gamma = 1.5$).

General conclusion

1-Main results

The work we presented in this thesis focused on the study of optoelectronic oscillators cascaded by nonlinear electronic components. For this purpose, two approaches have been considered, namely the theoretical and the experimental ones.

In the first chapter, we have reviewed the literature on some nonlinear electronic components (nonlinear capacitor, Colpitts oscillator), optical components (laser and applications, Mach-Zehnder modulator) through their characteristics and properties as well as the different models of optoelectronic oscillators (in the field of science and technology). In the same way, the presentation of the modulation of the electric signals allows us to understand that the *OOE* presents internal as well as external modulations. We have also explored frequency combs by listing their characteristics, equations, and some of their applications in everyday life. To conclude this chapter, we have outlined the problems to be solved in this manuscript.

In chapter 2 on methodology, our two systems were presented nemaly the *OEO-Colpitts* and *CN-OEO* system. Then we presented the components of the electrical and optical part of the *OEO*. In these sections, the frequency and the equations of the Colpitts oscillator have been found, as also that of the cubic nonlinear band pass filter (*CNBPF*) and we have listed the optical components used in this thesis. The threshold voltage of the laser diode used was obtained experimentally. The *RK4* methods for solving ordinary differential equations and delay differential equations applied to our equations previously determined as well as the method for spectral analysis of a system were presented. In other words, the whole experimental scheme was presented.

The last chapter (chapter 3) was dedicated to the presentation of the results obtained for the theoretical and experimental study of optoelectronic oscillators cascaded by nonlinear electronic components. In the first part of this chapter, the theoretical and experimental study of the Colpitts self-sustaining oscillator were done. The bifurcation diagram shows us three states namely the steady-state, the limit-cycle oscillation state, and finally the bursting or mixed-mode oscillations state controlled by the only variable parameter of the circuit which is a potentiometer. This bifurcation diagram is confirmed by the time traces thus indicating some characteristics of this self-sustained oscillator such as the amplitudes and frequencies of each dynamic. Very good agreement has been observed between the methods used.

Afterward, these dynamical states of the Colpitts oscillator (limit cycle and bursting oscillation) have been used to emulate complex fast regular, multi-periodic, bursting, and chaotic bursting oscillations in a simplified optoelectronic oscillator. Two principal cases have been developed: the case where the delay line has been considered and the case where it is removed. The results have shown that this latter case offers higher frequencies of bursting oscillations but, might be with slightly lower amplitude compared to the other case. This phenomenon is certainly inherent from the effect of the delay line in the same order as other phenomena such as chaos, amplitude death, and so on observed in delay systems [136]. Moreover, it is noteworthy that small noises occur in the experimental records mainly in the time intervals within two packages of bursting oscillations (see **figures 3.15-3.18**). We admit that such noises are due to both electronic and optoelectronic components of our *OEO-Colpitts* oscillator. On the other hand, comparing both the amplitudes and the frequencies of the solitary Colpitts oscillator and those of the *OEO-Colpitts* oscillator, it can be noticed that the *OEO-Colpitts* oscillator displays signals with higher amplitudes and frequencies. Such results could be important in photonic devices requiring the multiplication of amplitude and frequency. Moreover, mixed-mode oscillations of engineering systems include lasers, photonic microwave mixing, or neuromorphic computing using electro-optical systems with feedback could also benefit from the bursting capability.

The second part was devoted to the power spectrum analysis of time-delayed optoelectronic oscillators with wide and narrow band filters. To have the wide and narrow band non-linear filters we just need to control the value of the single coil contained in this non-linear filter since it could not affect other parameters according to the equations governing the dynamics of the system. By doing so, reducing the value of the coil L decreases τ while increasing L increases τ. First, when the value of the coil has been fixed at *10 µH* which corresponds to a wideband *CN-OEO*, the results have shown that the presence and the increase of the cubic nonlinear term do not affect the threshold value of the effective normalized gain which always equal to 1, but chaotic dynamics occurs at earlier values of the effective normalized gain when the nonlinear parameter increases ($|\gamma| = 2.5$, $|\gamma| = 2.35$, and $|\gamma| = 2.15$ for $\rho = 0$, $\rho = 6.4 \times 10^4$, and $\rho = 6.4 \times 10^6$, respectively). We have observed a very large increase in the fundamental frequency (300 *kHz* for $\rho = 0$, 2.1 *MHz* for $\rho = 6.4 \times 10^4$, and 5.8 *MHz* for $\rho = 6.4 \times 10^6$ when $\gamma = 1.05$ for the three cases). If we calculate the frequency ratio between the $\rho = 0$ case and the $\rho = 6.4 \times 10^6$ case when $\gamma = 1.05$, we see an increase of almost twenty times (**5.8/0.3=19.3**) in the frequency, which is an interesting result. Same for this

case, the presence of the cubic nonlinear term makes the *CN-OEO* like a high (in the range of *MHz*) frequency combs generator with a free spectral range equal to 303 *kHz* corresponding to the value of the inverse of the time-delay $1/T_D$. Thus, depending on the desired application, the length of the optical fiber can be increased or decreased to give a wider or narrower free spectral range. Then, when the coil value was increased and set to *10 mH* which corresponds to narrowband *CN-OEO*, and unlike the case of broadband *CN-OEO*, the cubic-nonlinear term influences the threshold value of the normalized effective gain (1 for $\rho = 0$, 3.36 for $\rho = 6.4 \times 10^4$, and 1.3 for $\rho = 6.4 \times 10^6$). Then, dynamically, the chaotic dynamics occurs a little far ($|\gamma| = 5.85$ for $\rho = 0$, $|\gamma| = 9.2$ for $\rho = 6.4 \times 10^4$, and $|\gamma| = 12.3$ for $\rho = 6.4 \times 10^6$). In this case (*L=10 mH*), we also noted a small increase in the fundamental frequency for the values of the normalized effective gain taken just above each threshold (9.5 *kHz* for $\rho = 0$ when $|\gamma| = 1.05$, 245 *kHz* for $\rho = 6.4 \times 10^4$ when $\gamma| = 3.45$, and 265 *kHz* for $\rho = 6.4 \times 10^6$ when $\gamma| = 1.5$). It is important to emphasize here that this case gives equally interesting dynamics but requires high-power laser diodes for its realization because the range of the gain which is a function of the laser diode power is very small. The results obtained by the two parts of this thesis show that each system is the seat of complex dynamic behavior.

2-Outlook

This work leaves open several issues, the main ones being the following:

❖A major challenge is to recover the mathematical equations of the *OEO- Colpitts* system to confront the numerical results with those obtained experimentally in this thesis. Subsequently, to redo numerically and experimentally the studies of the *OEO-Colpitts* system by further inserting another nonlinearity through an external modulator.

❖Further research investigations will be devoted to the exploration of multi-loop architectures of the *OEO-Colpitts* system which would provide extra degrees of freedom and therefore, a wider variety of dynamical behaviors [137]-[139].

❖It would also be very interesting to devote more research investigations to the exploration of the phase noise in *OEO- Colpitts* and *CN-OEO* systems and potential applications in radar[140,141]

❖A look will be taken at potential applications, especially when each of these two systems is synchronized.

Bibliography

[1]- Muhibul, H. B.: History of electronics, researgate.net, (2016).

[2]- Cheney, M. and R. Uth, Tesla, Master of Lightning, MetroBooks, New York, (1999).

[3]- KUZLE, I. Hrvoje, P., Darjan, B.: The true inventor of the radio communications. IEEE, pp. 20-23, (2008).

[4]-Colpitts, E.H.: Oscillation generator. U.S. Patent, 1 624 537, pp. 1-4, (1927).

[5]- Dodi, G., Ary, S., Setiyo, B.: A Novel Op-Amp Based LC Oscillator for Wireless Communications. *IECON*. The 46 th Annual Conference of the IEEE Industrial Electronics Society. (2020).

[6]- Van der Bijl, H. J.: The thermionic Vacuum Tube and Its Applications. New York: McGraw-Hill, (1920).

[7]- Cummings, B. R.: Recent developments in vacuum tube transmitters. Proc. Inst. Radio Eng., vol :13, pp. 49–108, (1925).

[8]- Llewellyn, F. B.: Constant frequency oscillators. Proc. Inst. Radio Eng., vol :19, pp. 2061–2094, (1931).

[9]-McArthur, E. D. and Spitzer, E. E.: Vacuum tubes as high-frequency oscillators. Proc. Inst. Radio Eng., vol :19, pp. 1971–1982, (1931).

[10]- Heising, R. A.: The audion oscillator. J. Amer. Inst. Elect. Eng., vol :39, pp. 365–376, (1920).

[11]-Jen, C. K.: A new treatment of electron tube oscillators with feedback coupling. Proc. Inst. Radio Eng., vol :19, pp. 2109–2144, (1931).

[12]- Amir, G., Hodjat, H., Bayram, B., and Ekmel, O.: Strong Light−Matter Interaction in Lithography-Free Planar Metamaterial Perfect Absorbers. American Chemical Society photonics, vol :5, pp. 4203–4221, (2018).

[13]- Rico, G., Manish, G., Klaus K., and Kern, K.: Light–matter interaction at atomic scales. Nature Reviews Physics. vol :3, pp. 441–453, (2021).

[14]- Paolo, P., Alessandro, M., Maria, A., Francesco, P., Rosalba, S., Cristian, D. E. B., Maria, G.D., Pietro, G.G., Philip, H.J., Giovanni,V., Onofrio, M.M. : Optical tweezers and their applications. Journal of Quantitative Spectroscopy and Radiative Transfer. vol :19, pp. 131-150, (2018).

[15]- Carlos, F. G., Rajib, A., Alexandra, P. M., Rui, L. R., Utkan, D.: Engineering Hydrogel-Based Biomedical Photonics: Design, Fabrication, and Applications advanced materials. vol :33, p. 2006582, (2021).

[16]- Arumugam, M.: Optical fiber communication -- An overview. Pramana - Journal of physics, vol :57, pp. 849-869, (2001).

[17]- Rashed, A.N.Z., Mohamed, A.E.A., Tabbour, M.S.F., Ismail, A.M.: Performance improvement for 16×40 Gb/s DWDM system using Non Return to Zero (NRZ), Return-to Zero (RZ) and Modified Duo Binary RZ (MD-RZ) modulation formats. Int J Adv Res Comput Sci Electron Eng. vol :6, p. 11, (2017).

[18]- Wahab, F.A., Leong, T.K., Zulkifili, H., Ibrahim, M.I.B., Talib, M.A.B, Zamri, N.A., et al.: Multiple transmitters & receivers for free space optical communication link performance analysis. J Telecommun Electron Comput Eng. vol :8, pp. 29–32, (2016).

[19]- Rashed, A.N.Z., Tabbour, M.S.F.: Suitable optical fiber communication channel for optical nonlinearity signal processing in high optical data rate systems. Wireless Pers Commun J. Springer Publisher. vol :97, pp. 397–416, (2017).

[20]- Maiman, T.H.: Stimulated emission of radiation in ruby. Nature. vol :187, pp. 493-494, (1960).

[21]- Kao, K. C., Hockman, G. A.: Dielectric Fiber Surface Waveguides for Optical Frequencies. Proc. IEEE, vol :113, pp. 1151–1158, (1966).

[22]- Argyris, A., *et al.*: Chaos-based communications at high bit rates using commercial fibre optic links. Nature. vol :438, pp. 343–346, (2005).

[23]- Ge, Z.-M., Hsiao, C.-L., Chen,Y.-S.: Nonlinear dynamics and chaos control for a time delay Duffing system. Int. J. Nonlin. Sci. Num. vol :6, pp. 187–199, (2005).

[24]- Li, T.-H. S., Tsai, S.-H., Hsia, M.-Y.: Robust H-infinity Fuzzy control for a class of time delay Fuzzy bilinear systems with an additive Disturbance. Int. J. Nonlin. Sci. Num. vol :10, pp. 315–322, (2009).

[25]- Erneux, T.: Applied delay differential equations. Book, Springer (2009).

[26]- Uchida, A.: Optical communication with chaotic lasers : Applications of nonlinear dynamics and synchronization. Book, Wiley, (2012).

[27]- Neyer, A., Voges, E.: Dynamics of electrooptic bistable devices with delayed feedback. IEEE J. Quantum Electron. vol :18, pp. 2009–2015, (1982).

[28]- Valle, R., Delisle, C.: Periodicity windows in a dynamical system with a delayed feedback. Phys. Rev. A. vol :34, p. 309, (1986).

[29]- Yao, X. S., and Maleki, L.: High frequency optical subcarrier generator. Elect. Letters vol :30, pp. 1525-1526, (1994).

[30]- Khugin, J. B., Kang, J.U., Ding, Y.J.: Ultrabroad-bandwidth electo-optic modulator based on a cascaded Bragg grating. Optics Letters, vol :25, pp. 70-72, (2000).

[31]- Yao, X.S., Maleki, L.: Optoelectronic microwave oscillator. J. Opt. Soc. Am. B Opt. Phys. vol :13, pp. 1725–1735, (1996).

[32]- Hao, T., et *al*.: Recent advances in OEOs. Adv. Photonics. vol :2, p. 044001-20, (2020).

[33]- Chembo, Y.K., Brunner, P., Jacquot, M., Larger, L.: Optoelectronic oscillators with time-delayed feedback. Rev. Mod. Phys. vol :91, 035006(1) – 035006(51), (2019).

[34]- Maleki, L.: The optoelectronic oscillator. Nat. Photon. vol :5, pp. 728–730, (2011).

[35]: Zou, X., *et al.*: OptoElectronic Oscillators (OEOs) to sensing, measurement, and detection. *IEEE J.* Quantum Electron. vol :52, pp.1–16, (2016).

[36]- Yao, J.: Optoelectronic oscillators for high speed and high resolution optical sensing. J. Lightw. Technol. vol :35, pp. 3489–3497, (2017).

[37]- Zhang, Y., Hou, D., Zhao, J.: Long-term frequency stabilization of an optoelectronic oscillator using phase-locked loop. IEEE J. Lightw. Technol. vol :32, pp. 2408–2414, (2014).

[38]- Saleh, K., Lin, G., Chembo, Y. K.: Effect of laser coupling and active stabilization on the phase noise performance of optoelectronic microwave oscillators based on whispering gallery-mode resonators. IEEE Photon. J. vol :7, pp. 1–11, (2014).

[39]- Lasri, J., *et al.*: A self-starting hybrid optoelectronic oscillator generating ultra low jitter 10-GHz optical pulses and low phase noise electrical signals. IEEE Photon. Technol. Lett. vol :14, pp. 1004–1006, (2020).

[40]- Jia, S., *et al.*: A novel highly stable dual-wavelength short optical pulse source based on a dual-loop optoelectronic oscillator with two wavelengths. IEEE Photon. J. vol :7, pp. 1–11, (2015).

[41]- Chembo, Y. K., et *al*.: Chaotic breathers in delayed electrooptical systems. Phys. Rev.Lett. vol :95, p. 203903, (2005).

[42]- Weicker, L.,*et al.*: Slow-fast dynamics of a time-delayed electro-optic oscillator. Phil. Trans. R. Soc. A. vol :371, p. 20120459, (2013).

[43]- Chengui, G. R. G., Talla, A. F., Talla Mbé, J. H., Coillet, A., Saleh, K., Larger, L., Woafo, P., Chembo, Y. K. C. : Theoretical and experimental study of slow-scale Hopf limit-cycles in laser-based wideband optoelectronic oscillators. J. Opt. Soc. Am. B. vol :31, pp. 2310–2316, (2014).

[44]- Sciamanna, M., Shore, K. A.: Physics and applications of laser diode chaos. Nat. Photonics. vol :9, pp. 151–162, (2015).

[45]- Zhang, L., Pan, B., Chen, G., Guo, L., Lu, D., Zhao, L., Wang, W.: 640-Gbit/s fast physical random number generation using a broadband chaotic semiconductor laser. Sci. Rep. vol :7, pp. 1-8, (2017).

[46]- Larger, L., *et al.*: Photonic information processing beyond Turing: An optoelectronic implementation of reservoir computing. Opt. Express. vol :20, pp. 3241–3249, (2012).

[47]- Martinenghi, R., Rybalko, S., Jacquot, M., Chembo, Y. K., Larger, L.: Photonic nonlinear transient computing with multiple-delay wave length dynamics. Phys. Rev. Lett. vol :108, p. 244101, (2012).

[48]- Chembo, Y.K., Larger, L., Tavernier, H., Bendoula, R., Rubiola, E., Colet, P.: Dynamic in stabilities generated with optoelectronic oscillators. Opt. Lett. vol :32, pp. 2571–2573, (2007).

[49]- Talla Mbé, J. H., Kamaha, J. S. D., Chembo, Y. K., Woafo, P.: Dynamics of wideband time-delayed optoelectronic oscillators with nonlinear flters. IEEE J. Quantum Electron. vol :55, p. 5000106(1)–5000106(6), (2019a).

[50]- Romeira, B., Kong, F., Figueiredo, J. M. L., Javaloyes, J., Yao, J.: High-speed spiking and bursting oscillations in a long-delayed broadband optoelectronic oscillator. IEEE J. Lightw. Technol. vol :33, pp. 503–510, (2015).

[51]- Hargrove, L. E., Fork, R .L. , Pollack, M. A.: Locking of He-Ne laser mo des induced by synchronous intracavity modulation. App. Phys. Lett. vol :5, pp. 4–5, (1964).

[52]- Chan, S. C., Xia, G. Q., and Liu, J. M.: Optical generation of a precise microwave frequency comb by harmonic frequency locking. Opt. Lett. vol :32, pp. 1917–1919, (2007).

[53]- Juan, Y. S., Lin, F. Y.: Ultra broadband microwave frequency combs generated by an optical pulse-injected semiconductor laser. Opt. Lett. vol :17, pp. 18596–18605, (2009).

[54]- Zhao, M. R., Wu, Z.M., Deng, T., Zhou, L., Xia G.Q.:Tunable and broadband microwave frequency combs based on a semiconductor laser with incoherent optical feedback. Chin.Phys. B. vol :24, p. 054207, (2015).

[55]- Xu, Y., Peng, H., Guo, R., Du, H., Yin, Q., Hu, G., He, J., Chen, Z.: Injection-Locked Millimeter Wave Frequency Divider Utilizing Optoelectronic Oscillator Based Optical Frequency Comb. IEEE Photon. J. vol :11, pp. 1-8, (2019).

[56]- Cheng, Y., Yan,J., Zhao,S. : Flat Self-Oscillating Parametric Optical Frequency Comb Based On A Dual-Mode Microcavity Laser. IEEE Photon. Techno. Lettres. vol :34, pp. 325-328, (2022).

[57]- Savchenkov, A. A., Motsko, A. B., Maleki, L.: On Frequency Combs in monolithic resonators. Nanophotonics. vol :5, pp. 363-391, (2016).

[58]- Chembo, Y. K.,: Kerr optical frequency Combs : Theory, applications and perspectives. Nanophotonics. vol :5, pp. 214–230, (2016).

[59]- Yokoyama, S., Nakamura, R., Nose, M., Araki, T., Yasui, T.: Terahertz spectrum analyzer based on a terahertz frequency comb. Opt. Express. vol :16, pp. 13052–13061, (2008).

[60]- Hale, P.D., Williams, D.F. Dienstfrey,A. :Waveform metrology : signal measurements in a modulated world. Metrologia. vol :55, S135–S151, (2018).

[61]- Williams, D.F., *et al.*: Comparing LSNA calibration : Large-signal network analyzer round robin. IEEE Microw. Mag. vol :17, pp. 59–64, (2016).

[62]- Cho, C., Koo, H., Kwon, J. Y., Lee, J. G.: Phase calibration and uncertainty evaluation for RF comb generator. Control. vol :53, pp. 698–703, (2020).

[63]- Coddington, I., Newbury, N., wann, W.: Dual-comb spectroscopy. Optica. vol :3, pp. 414–426, (2016).

[64]- Gill, G. S., Chiang, H. F., Hall, J.: Waveform synthesis for ultra wideband radar. in Proceedings of 1994 IEEE National Radar Conference. pp. 240–245, (1994).

[65]- Chengui, G. R. G., Talla Mbé, J. H., Talla, A. F., Woafo, P., Chembo, Y.K.: Dynamics of optoelectronic oscillators with electronic and laser nonlinearities. IEEE J. Quantum Electron. vol :54, pp. 1-7, (2017).

[66]- Chengui, G. R. G., Woafo, P., Chembo, Y. K.: The simplest laser based optoelectronic oscillator: an experimental and theoretical study. J. Light. Technol. vol :34, pp. 873–878, (2016).

[67]- Talla Mbé, J. H., Kamaha, J. S. D., Woafo, P., Chembo, Y. K.: Dynamics of wideband time-delayed optoelectronic oscillators with nonlinear filters. IEEE J. Quantum Electron. vol :55, pp. 1–6, (2019).

[68]- Kamaha, J. S. D., Talla Mbé, J. H., and Woafo, P.: Routes to chaos and characterization of limit-cycle oscillations in wideband time-delayed optoelectronic oscillators with nonlinear filters. J. Optical Society of America B. vol :37, A75–A82, (2020).

[69]- Kamaha, J. S. D., Talla Mbé, J. H., Noubissie, S., Fotsin, H. B., Woafo, P.: Dynamics of optoelectronic oscillators with band pass filter and laser nonlinearities: theory and experiment. Opt. Quantum Electron. vol :54, pp. 1–15, (2022).

[70]- Colpitts, E. H.: Oscillation generator. U.S. Patent 1 624 537, Feb. 1, (1927).

[71]- https://www.electrical4u.com/colpitts-oscillator/ February 21, (2021).

[72]- Horowitz, P., Hill, W.: The art of electronics. 2nd ed. New York, USA: Cambridge University Press; (1994).

[73]- Kennedy, M. P.: Chaos in the Colpitts oscillator. IEEE Trans Circ Syst-I. vol :41, pp. 771–774. (1994).

[74]- Maggio, G. M., De Feo, O., Kennedy, M. P.: Nonlinear analysis of the Colpitts oscillator and application to design. IEEE Trans Circ Syst. vol :46, pp. 1118–1130, (1999).

[75]- Mykolaitis, G., Tamasevicius, A., Bumeliene, S.: Experimental demonstration of chaos from the Colpitts oscillator in the VHF and the UHF ranges. Electron Lett. vol :40, pp. 91–2, (2004).

[76]- Chua, L.O., Wu, C. W., Huang, A., Zhong, G. Q.: A universal circuit for studying and generating chaos-Part I: Routes to chaos. IEEE Trans. Circ. Syst. vol :40, pp. 731–44, (1993).

[77]- Silva, C. P, Young, A. M.: Introduction to chaos-based communications and signal processing. In: IEEE Aerospace conference reprint. vol :1, pp. 279–299, (2000).

[78]-https://www.elprocus.com/colpitts-oscillator-circuit-working-and-applications/ consulté le 01.Nov. (2022).

[79]- Kwuimy, C. A. K., and Woafo, P.: Experimental realization and simulations a self-sustained macro electromechanical system. Mech. Res. Commun., vol :37, pp. 106–110, (2010).

[80]- Fregien, G., and Van Wyk, J. D.: Nonlinear capacitors in snubber circuits for GTO thyristors. IEEE Trans. Power Electron., vol :8, pp. 425–429, (1992).

[81]- Kitio, K. C. A.: Thèse de Doctorat de l'Université de Yaoundé I. (2008).

[82]- Hayashi, C. : Nonlinear Oscillations in Physical Systems. New York, NY, USA: McGraw-Hill, p. 101 (1964).

[83]- Keang-Po Ho,: Advanced Topics in Lightwave Communications Generation of Optical Signals. pp. 1-20, February 24, (2005).

[84]- Kingni, S. T.: Thèse de Doctorat/PhD de l'Universite de Yaounde 1. (2014).

[85]- Ogasawara, N., Ito, R.: Lasers, Semiconductor. The optics Encyclopedia : Basic Foundations and practical Applications. First published: 15 September (2007).

[86]- Niloy K. D., Govind P. A.: Quantum Well Semiconductor Lasers. Van Nostrand Reinhold, 2e edition, (1993).

[87]- Varon, G. M Durant, these de doctorat de l'Université de Toulouse. (2008).

[88]-Talla Mbé, J.H., Woafo, P., Fotsin, H.B. : Experimental direct modulation of a laser diode with a Van der Pol circuit and applications. Opt. Eng. vol :58, p. 066114 (2019).

[89]- Yupeng, L:, Yangan Z., and Yongqing H.: Any Bias Point Control Technique for Mach–Zehnder Modulator. IEEE Photonics Technology Letters, vol :25, pp. 2412 – 2415, (2013).

[90]- Pawela, Y.: Thèse de Doctorat de l'Université de Franche-Comté, Besançon, (2012).

[91]- Chuang, S. L.: Physics of Optoelectronic Devices, *Wiley*, New York, (1995).

104

[92]- Mochida, Y., Yamaguchi, N., and Ishikawa, G.: Technology-Oriented Review and Vision of 40-Gb/s-Based Optical Transport Networks. IEEE J. of Lightwave Technol, vol :20, pp. 2272-2281, (2002).

[93]- Huszaník, T., Ovseník, Ľ., Turán, J.: Performance Analysis of Optical Modulation Formats for 10 Gbit/s DWDM System. Carpathian Journal of Electronic and Computer Engineering, vol :10, pp. 15-20, (2017).

[94]- Ovseník, L., Turán, J. , Ivaniga, T. , Ivaniga, P.: Deployment of the PON with an optical fiber G-652.B. IEEE 14th International Scientific Conference on Informatics, Proceedings, pp. 289-292, (2017).

[95]- Kurbatska, I. Spolitis, S., Bobrovs, V., Alsevska, A., Ivanovs, G.: Performance Comparison of Modulation Formats for 10 Gbit/s WDMPON Systems. Advances in Wireless and Optical Communications, pp. 51-54, (2016).

[96]- Chrostowski, J., Vallee, R., and Delisle, C.: Self-pulsing and chaos in acoustooptic bistability. Can. J. Phys., vol :61, pp. 1143-1148, (1983).

[97]- Chembo, Y. K., et *al*,: Optoelectronic oscillators with time-delayed feedback. Reviews of Modern Physics, vol :91,, p. 035006, (2019).

[98]- Yao, X. S., and Maleki, L.: High frequency optical subcarrier generator. , Electronics Letters, vol :30, pp. 1525–1526, (1994).

[99]- Neyer, A. and Voges, E.: Dynamics of electrooptic bistable devices with delayed feedback. IEEE J. Quantum Electron. vol :18, pp. 2009–2015, (1982).

[100]- Ji, Y., Yao, X. S. and Malekii, L.: Compact optoelectronic oscillator with ultra-low phase noise performance. Electronics Letters, vol :35, pp. 1554–1555, (1999).

[101]- Correa-Mena, A. G., et al.: Performance Evaluation of an Optoelectronic Oscillator Based on a Band-pass Microwave Photonic Filter Architecture. Radioengineering. vol :26, pp. 642-646, (2017).

[102]- Ikeda, K.: Multiple-valued stationary state and its instability of the transmitted light by a ring cavity system. Optical Commun. vol :30, pp. 257-261, (1979).

[103]- Chembo, Y. K., Colet, P., Larger, L., and Gastaud, N.: Chaotic Breathers in Delayed Electro-Optical Systems. Phys. Rev. Lett. vol :95, p. 203903, (2005).

[104]- Peil, M., Jacquot, M., Chembo, Y. K., Larger, L., and Erneux, T. : Routes to chaos and multiple time scale dynamics in broadband bandpass nonlinear delay electro-optic oscillators. Phys. Rev. E. vol :79, **p.** 026208, (2009).

[105]- Talla A. F.: Thèse de Doctorat de l'Université de Yaoundé 1. (2016).

[106]- Nguimdo, R. M. : Thèse de Doctorat de l'Université de Balearic Islands, Palma de Mallorca, (2011).

[107]- Martinenghi, R.: Thèse de Doctorat de l'Université de Franche-Comté, Besançon, (2013).

[108]- Nguimdo, R. M., Lavrov, R., Colet, P., Jacquot, M., Chembo, Y. K., and Larger, L.: Effet of fiber on broadband chaos communication implemented by electro-optic nonlinear delay phase dynamic. IEEE. J. Lightwave Technol. vol :28, pp. 2688-2696, (2010).

[109]- Goune. R. G. C.: Thèse de Doctorat de l'Université de Yaoundé 1, (2016).

[110]- Ginoux, J.-M., and Letellier, C.: Van der Pol and the history of relaxation oscillations : Toward the emergence of a concept. Chaos, vol :22, p. 023120, (2012).

[111]- Kyprianidis, I. M., Papachristou, V., Stouboulos, I. N., Volos, Ch. K.: Dynamics of Coupled Chaotic Bonhoeffer–van der Pol Oscillators. WSEAS TRANSACTIONS on SYSTEMS, vol :11, pp. 516-526, (2012).

[112]- Talla, A.F., Martinenghi, R., Woafo, P., Chembo, Y. K.: Breather and Pulse-Package Dynamics in Multinonlinear Electrooptical Systems With Delayed Feedback. IEEE Photonics Journal. vol :8, pp. 1-8, (2016).

[113]- Kouomou, Y.C., and Woafo, P.: Transitions from spatiotemporal chaos to cluster and complete synchronization states in a shift-invariant set of coupled nonlinear oscillators. Phys. Rev. E, Stat. Phys. Plasmas Fluids Relat. Interdiscip. Top, vol :67, p. 046205. (2003).

[114]- Kouomou, Y. C., and Woafo, P.: Cluster synchronization in coupled chaotic semiconductor lasers and application to switching in chaos secured communication networks. Opt. Commun., vol :223, pp. 283–293, (2003).

[115]- Talla Mbé, J.H., Atchoffo, W.N., Tchitnga, R., and Woafo, P.: Dynamics of Time-Delayed Optoelectronic Oscillators With Nonlinear Amplifiers and Its Potential Application to Random Numbers Generation. I.E.E.E J. of Quant. Elect., vol :57, p. 5000507 (2021).

[116]- Larger, L., and Dudley, J. M.: Optoelectronic chaos. Nature (London), vol :465, pp. 41-42. (2010).

[117]- Arecchi, F. T., Giacomelli, G., Lapucci, A., and Meucci, R.: Two-dimensional representation of a delayed dynamical system. Phys. Rev. A. vol :45, R4225 –R4228, (1992).

[118]- Tchuissa, K.K.M., Talla Mbé, J.H., Tamo , T.T.: Efficient sensings of temperature, refractive index, and distance measurement using the cubic-nonlinear optoelectronic oscillators. Opt. and Quant. Elect. vol :54, p. 311 (2022).

[119]- Scott, A. D., Kerry, V., Thomas, U.: Optical frequency combs: Coherently uniting the electromagnetic spectrum. Science, vol :369, p.3676, (2020).

[120]- Tara, F., and Esther, B.: 20 years of developments in optical frequency comb technology and applications. Communication Physics. vol :2, p. 153, (2020).

[121]- Eckstein, J. N.: High resolution spectroscopy using multiple coherent interactions, Ph.D. thesis, Stanford University, (1978).

[122]- Ferguson, A. I., Eckstein, J. N., Hänsch, T. W.: Polarization spectroscopy with ultrashort light pulses. Appl. Phys. Berl., vol :18, pp. 257–260, (1979).

[123]- Udem, T., Holzwarth, R., Hänsch, T. W.: Optical frequency metrology. Nature. vol :416, pp. 233–237, (2002).

[124]- Kasdin, N. J.: Runge-Kutta Algorithm for the Numerical Integration of Stochastic Differential Equations, J. Guid. Control. Dyn., vol :18, pp. 114–120, (1995).

[125]- Teschl, G.: Ordinary differential equations and dynamical systems, Baylor.Edu, (140), (2012).

[126]- Press, W. H., Teukolsky, S. A., Vetterling, W. T., and Flannery, B. P.: Cambridge University Press, Cambridge UK, (2007).

[127]- Bellen, A. and Zennaro, M.: Numerical Method for delay differential equations. Oxford University, Press, (2003).

[128]- Faure, F.: Systèmes dynamiques, Chaos et Applications. cours de Master I de l'Université de Joseph Fourier, Grenoble, France. (2015).

[129]- Amphenol Socapex, www.amphenol-socapex.com, comprendre la fibre optique DOC

[130]- Thorlabs.: PDA10CF InGaAs Amplified Detector, User Guide.

[131]- Kengne, J., Chedjou, J. C., Kenne, G., Kyamakya, K.: Dynamical properties and chaos synchronization of improved Colpitts oscillators. Commun. Nonlinear Sci. Numer. Simul. vol :17, pp. 2914–2923, (2012).

[132]- Chembo, Y. K., Colet, P., Larger, L., and Gastaud, N.: Chaotic breathers in delayed electro-optical systems. Phys. Rev. Lett., vol :95, p. 203903, (2005).

[133]- Talla Mbé, J. H., Talla, A. F., Chengui, G. R. G., Coillet, A., Larger, L., Woafo, P., and Chembo, Y. K.: Mixed-mode oscillations in slow-fast delayed optoelectronic systems. Phys. Rev. E, vol :91, p. 012902, (2015).

[134]- Chembo, Y. K., Larger, L., Tavernier, H., Bendoula, R., Rubiola, E., and Colet, P.: Dynamic instabilities of microwaves generated with optoelectronic oscillators. Opt. Lett., vol :32, pp. 2571–2573, (2007).

[135]- Udem, Th., Holzwarth, R., Hansch, T. W.: Optical frequency metrology. Nature, vol :416, pp. 233–237, (2002).

[136]- Lakshmanan, M., Senthilkumar, D.V.: Dynamics of Nonlinear Time–Delay Systems. Springer, Science and Business Media. (2011).

[137]- Shumakher, E., Eisenstein, G.: A novel multiloop optoelectronic oscillator. IEEE Photon. Technol. Lett., vol :20, pp. 1881–1883, (2008).

[138]- Levy, E.C., Okusaga, O., Horowitz, M., Menyuk, C.R., Zhou, W., Gary, M.C.: Comprehensive computational model of single-and dual-loop optoelectronic oscillators with experimental verifcation. Opt. Express, vol :18, pp. 21461–21476, (2010).

[139]- Nguimdo, R.M., Chembo, Y.K., Colet, P., Larger, L.: On the phase noise performance of nonlinear double-loop optoelectronic microwave oscillators. IEEE J. Quantum Electron. vol :48, pp. 1415–1423, (2012).

[140]- Xu, H., Li, L., Li, Y., Zhang, J., Han, H., Liu, L., and Li, J.: Chaos-Based Through-Wall Life-Detection Radar. Int. J. Bifurcation and Chaos, vol :29, p. 1930020, (2019).

[141]- Xu, H., Li, Y., Zhang, J., Han, H., Bing, Z., Wang, L., Wang, Y., and Wang, A.: Ultra-Wideband Chaos Life-Detection Radar with Sinusoidal Wave Modulation. Int. J. Bifurcation and Chaos,. vol :27, p. 1730046, (2017).

List of publications

1- **René Mboyo Kouayep**, Alain Francis Talla, Jimmi Hervé Talla Mbé, Paul Woafo : Bursting oscillations in Colpitts oscillator and application in optoelectronics for the generation of complex optical signals. Optical and Quantum Electronics **52**,291 (2020).

2- **René Mboyo Kouayep**, Jimmi Hervé Talla Mbé, Paul Woafo : Power spectrum analysis of time-delayed optoelectronic oscillators with wide and narrow band nonlinear filters. Optical and Quantum Electronics **55**, 62 (2022).

Check for
updates

Bursting oscillations in Colpitts oscillator and application in optoelectronics for the generation of complex optical signals

Rene Mboyo Kouayep[1] · Alain Francis Talla[1,2] · Jimmi Hervé Talla Mbé[1,3] · Paul Woafo[1]

Abstract

We are exploring an optoelectronic oscillator featuring a Colpitts oscillator in its electrical path. The Colpitts oscillator generates high frequency electrical signals and exhibits dynamical behaviors such as periodic and bursting oscillations which can be easily monitored using a potentiometer. Inserting the Colpitts oscillator in the optoelectronic oscillator, we put forward the interaction between optical nonlinearity and electronic nonlinearity to obtain also complex dynamical behaviors. The temporal dynamics of the system with and without delayed feedback is investigated experimentally. It is shown that a wide variety of periodic and chaotic states can be excited and that there is an amplification of the signal frequencies. In particular, bursting, chaotic bursting and chaotic pulse-package oscillations with slow-fast temporal dynamics are experimentally observed in the system.

Keywords Optoelectronic oscillator · Colpitts oscillator · Bursting oscillation · Chaotic pulse-package oscillations

1 Introduction

Oscillators of the Colpitts-type are well-known since they are commonly used as electronic oscillators for generating limit-cycle oscillations at radio frequencies and present some interesting advantages such as the relative simplicity of their electronic circuits (Horowitz and Hill 1994; Kengne et al. 2012; Effa et al. 2009). It was shown that, with an appropriate setting of these circuit parameters, they can exhibit rich and complex dynamical behaviors (chaos) at various operating frequencies which potential applications are in

✉ Jimmi Hervé Talla Mbé
  jhtallam@yahoo.fr

1   Laboratory of Modeling and Simulation in Engineering, Biomimetics and Prototypes, Department of Physics, University of Yaoundé I, P. O. Box 812, Yaoundé, Cameroon

2   Department of Mechanical, Petroleum and Gas Engineering, Faculty of Mines and Petroleum Industries, University of Maroua, P.O. Box 08, Kaele, Cameroon

3   Laboratory of Condensed Matter, Electronics and Signal Processing, Department of Physics, University of Dschang, P.O. Box 67, Dschang, Cameroon

🦋 Springer

communication, radar systems, and so on (Kennedy 1994; Maggio et al. 1999; Mykolaitis et al. 2004; Tamasevicius et al. 2006; Uchida et al. 2003; Lindberg et al. 2007). These attractive properties justify our choice focused on this class of oscillators. In this paper, we are proposing a Colpitts oscillator which, in addition to limit-cycle, can also display bursting oscillations. It is important to highlight that bursting oscillations are observed in many practical systems and found a multitude of applications in areas such as electro-mechanics (Hunter et al. 1997; Simo and Woafo 2011), electronics (Kingni et al. 2013), biology (Sherman et al. 1988; Izhikevich 2000), bio-engineering of artificial organs (Jerrelind and Stensson 2000; Plant and Kim 1976; Nash and Hunter 2000), to name just a few.

Besides complex oscillators, the optoelectronic oscillators (OEOs) offer the advantage of generating both electrical and optical signals for a more wide range of applications. Indeed, they are nonlinear and autonomous systems characterized by a closed feedback loop that is formed with two concatenated optical and electronic branches (Yao and Maleki 1996; Maleki 2011; Chembo et al. 2019). These systems with delayed feedback have been the focus of intense research activities in recent years and were shown to be excellent platforms to investigate the interaction between the complexity induced by nonlinearity and the infinite dimensionality inherent to the time-delay (Chembo et al. 2005, 2007; Talla Mbé et al. 2015, 2019a; Romeira et al. 2015). The OEOs have found various applications such as ultra-stable microwave generation (Yao and Maleki 1996; Okusaga et al. 2011; Nguimdo et al. 2012; Zhang et al. 2014; Lelièvre et al. 2017; Ly et al. 2018), chaos communications (Argyris et al. 2005; Cohen et al. 2008; Ai et al. 2017), neuromorphic computing (Paquot et al. 2012; Soriano et al. 2013; Larger et al. 2017), detection, measurement and sensing (Zou et al. 2016; Yao 2017; Wu et al. 2018), time–frequency metrology (Chang et al. 2016; Huang et al. 2018), pulse generation in optical fiber networks (Yao et al. 2000; Lasri et al. 2002; Chembo et al. 2009; Huang et al. 2014; Jia et al. 2015; Romeira et al. 2015; Talla et al. 2016), among other technological aims. These applications were recently reviewed by Chembo et al. 2019. In the architectures of OEOs used for most applications cited above, the nonlinear conversion between the electrical and the optical signals is performed by a phase or an intensity modulator with a sinusoidal transfer function. On the other hand, it was demonstrated that other electro-optic components can be used to achieve such nonlinear conversion (Chengui et al. 2016, 2018). These authors exploited the seeding laser diode (LD) itself as an electrical-to-optical converter through its power-intensity transfer function which offers an advantage in congestion. For instance, such an idea was carried out with a Van der Pol oscillator in the electrical path (Chengui et al. 2018). Chaotic and limit-cycle oscillations were generated experimentally, but at frequencies up to some kHz imposed by the Van der Pol oscillator. Moreover, recently, it was demonstrated that the insertion of a nonlinear device in the electrical path of a classical OEO increases both the amplitude and the frequency of limit-cycle oscillation (Talla Mbé et al. 2019b).

In this article, we are investigating a Colpitts oscillator capable of displaying bursting and limit-cycle oscillations at higher frequencies (in the range of MHz). Such characteristics of the Colpitts oscillator is used to emulate high-frequency complex dynamics in a simplified OEO where the feedback loop is closed on the laser diode and featuring that Colpitts oscillator in its electrical path.

The work is organized as follows. Section 2 deals with the study of the solitary Colpitts oscillator. The electronic structure of this oscillator is addressed and the appropriate mathematical model is derived to describe its dynamical behaviors. Section 3 presents an OEO featuring the Colpitts oscillator in the feedback loop (OEO-Colpitts oscillator). Firstly, the circuit description of the OEO-Colpitts oscillator is designed and secondly, the complex dynamical behaviors of the whole system are studied. A conclusion is given in Sect. 4.

2 The Colpitts oscillator

2.1 Circuit and equation

The design of the Colpitts oscillator is shown in Fig. 1a when the switches K_{in} and K_{out} are off. Figure 1b depicts its experimental set-up. The following electronic components are used: four resistors (R_1, R_2, R_3, and R_4); five capacitors (C_1, C_2, C_3, C_4, and C_5), one coil (L), and one transistor of type 2N2222 which is polarized with $V_0 = 5$ V. The values of these electronic components are given as follows: $R_1 = R_2 = 10$ kΩ, $R_3 = 100\,\Omega$, and R_4 is a potentiometer of maximum value $220\,\Omega$; $C_1 = C_2 = 10$ nF, $C_3 = C_4 = C_5 = 1$ nF, and $L = 5\,\mu$H.

The expression of the eigen frequency of this oscillator is estimated by Eq. (1) and by considering the values of the previous components, its theoretical value is equal to 3.2 MHz

$$f = \frac{1}{2\pi}\sqrt{\frac{C_4 + C_5}{LC_4C_5}} \tag{1}$$

Applying the Kirchhoff's law at the circuit of Fig. 1, one obtains the following set of equations:

$$\begin{cases} L\frac{dI_L}{dt} = V_{C_4} - V_{C_5} \\ R_1C_1\frac{dV_{C_1}}{dt} = 2V_{BE} + 2V_{C_2} - V_0 + R_1I_b \\ R_3C_2\frac{dV_{C_2}}{dt} = R_3I_E - V_{C_2} \\ R_4C_3\frac{dV_{C_3}}{dt} = V_0 - V_{C_3} - V_{C_4} - R_4I_C \\ R_4C_4\frac{dV_{C_4}}{dt} = V_0 - V_{C_3} - V_{C_4} - R_4I_C - R_4I_L \\ R_1C_5\frac{dV_{C_3}}{dt} = R_1I_L - 2V_{BE} - 2V_{C_2} - R_1I_b + V_0 \end{cases} \tag{2}$$

where $V_{C_i} (i = 1, 2, \ldots, 5)$ represent the voltages across the capacitors C_i. $V_{BE} = V_{C_5} - V_{C_2} - V_{C_1}$ is the emitter–base voltage, $I_E = f(V_{BE}) = I_S\left[\exp\left(\frac{V_{BE}}{V_T}\right) - 1\right]$ the emitter current, I_C is the collector current, I_b is the base current ($I_C = \beta I_b$). V_T and I_S are the thermal voltage and the saturation current of the emitter–base of the bipolar junction
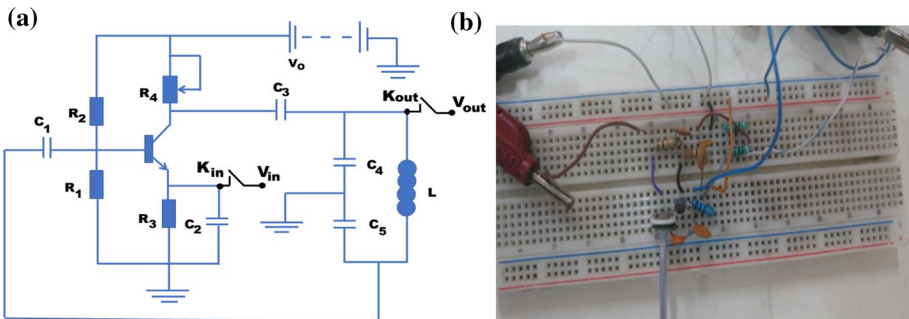

Fig. 1 **a** Electronic circuit of the Colpitts oscillator. **b** A picture of the Colpitts circuit in the laboratory

transistor, respectively. For a convenient numerical analysis, let us introduce the following set of dimensionless variables and parameters as

$$x_1 = \frac{V_{C_2}}{V_T}, \quad x_2 = \frac{V_{C_3}}{V_T}, \quad x_3 = \frac{V_{C_4}}{V_T}, \quad x_4 = \frac{\rho I_L}{V_T}, \quad x_5 = \frac{V_{C_5}}{V_T},$$

$$x_6 = \frac{V_{C_1}}{V_T}, \quad \rho = \sqrt{\frac{L}{C_3}}, \quad a = \frac{V_0}{V_T}, \quad \nu_1 = \frac{V_{BE}}{V_T} = x_5 - x_6 - x_1$$

$$v = \frac{2\sqrt{LC_3}}{R_1 C_1}, \quad \gamma_2 = \frac{\sqrt{LC_3}}{C_1(\beta+1)V_T} I_S, \quad a_1 = \frac{\sqrt{LC_3}}{C_2 V_T} I_S, \quad b_1 = \frac{\sqrt{LC_3}}{R_3 C_2}$$

$$a_2 = \frac{\beta\sqrt{LC_3}}{C_3(\beta+1)V_T} I_S, \quad a_3 = \frac{\sqrt{LC_3}}{R_4 C_4}, \quad g = \frac{\beta\sqrt{LC_3}}{C_4(\beta+1)V_T} I_S, \quad b_3 = \frac{C_3}{C_4}$$

$$a_3 = \frac{C_3}{C_5}, \quad \gamma = \frac{2\sqrt{LC_3}}{R_1 C_5}, \quad \varepsilon = \frac{\sqrt{LC_3}}{C_5(\beta+1)V_T} I_S, \quad a_4 = \frac{\sqrt{LC_3}}{R_4 C_3}.$$

The normalized time t' is such that $t' = \frac{t}{\tau}$, with $\tau = \sqrt{LC_3}$

Therefore, the above equations are rewritten in the dimensionless form as

$$\begin{cases} \dot{x}_1 = a_1 e^{\nu_1} - b_1 x_1 \\ \dot{x}_2 = a_4 \left[a - x_2 - x_3 \right] - a_2 e^{\nu_1} \\ \dot{x}_3 = a_3 \left[a - x_2 - x_3 \right] - g e^{\nu_1} - b_3 x_4 \\ \dot{x}_4 = x_3 - x_5 \\ \dot{x}_5 = a_5 x_4 + \gamma \left[x_6 - x_5 + \frac{a}{2} \right] - \varepsilon e^{\nu_1} \\ \qquad \dot{x}_6 = v \left[x_5 - x_6 - \frac{a}{2} \right] + \gamma_2 e^{\nu_1} \end{cases} \qquad (3)$$

In the Sect 2.2, the experimental records will be compared to the numerical results obtained with the set of Eq. (3).

2.2 Dynamics of the Colpitts oscillator

Experimentally, when tuning the potentiometer (R_4), different time-traces have been recorded (Fig. 2) and compared to the numerical ones obtained from Eq. (3). It appears that the Colpitts oscillator exhibits limit-cycle and bursting oscillations depending on the value of the potentiometer. An interesting agreement is found between the numerical and experimental results.

Figure 2a, b present the case where $R_4 = 50\,\Omega$. The Colpitts oscillator displays limit-cycle oscillation having a frequency of 4.5 MHz and a maximum amplitude of 264 mV. As R_4 is further increased, the limit-cycle changes to the bursting oscillations (Fig. 2c, d for $R_4 = 105\,\Omega$).

Indeed, when R_4 is equal to $R_4 = 105\,\Omega$, the bursting oscillation appears as it can be seen in Fig. 2c, d. These bursting oscillations are characterized by the alternation of two phases: silent and active phases. The silent phase (interval between two packages of oscillations) is characterized by a sort of dead zone where the voltage output is always constant to zero. The active phase (packages of oscillations) consists of the transient apparition of fast oscillations of a short period compared to the period of the package which is referred
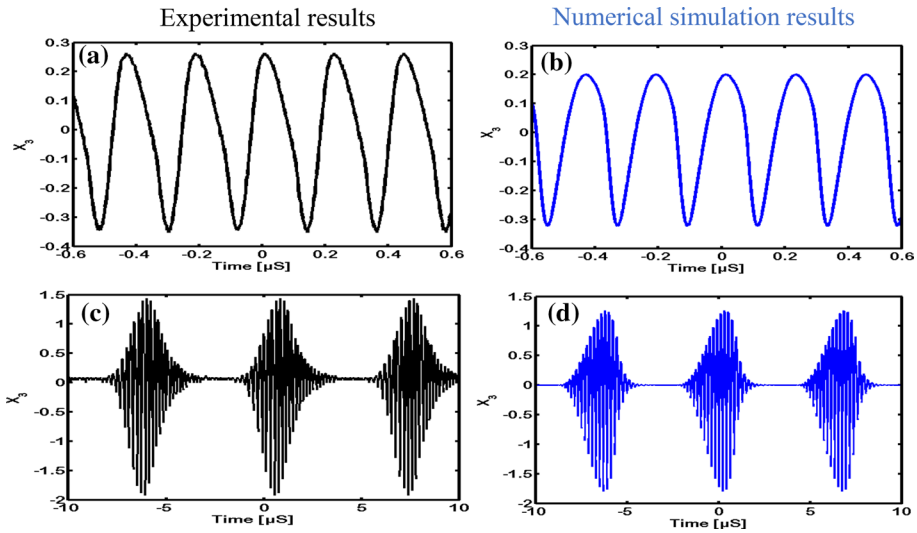
Fig. 2 Sinusoidal and bursting oscillations in the solitary Colpitts oscillator. **a**, **c** are the experimental results. **b**, **d** are numerical simulation results

to as slow. The frequency of the slow oscillation is equal to 2.5 MHz with a maximum amplitude of 1.44 MHz. These bursting oscillations similar to the conventional heart sound signals (Kingni et al. 2013) are quite raised in amplitude and frequency and could also be used in telecommunication as the amplitude modulator (AM), and for radar systems.

It is also important to note that the minimum and maximum frequencies of limit-cycle obtained with this oscillator are of 3.5 MHz (which is appreciably close to the theoretical frequency of 3.2 MHz) with a maximum amplitude equal to 8.2 V and 4.76 MHz with a maximum amplitude of 320 mV, respectively given by Fig. 3a, b for different values of R_4.

To better appreciate the frontiers between the different dynamical regimes of the Colpitts oscillator, its numerical bifurcation diagram is plotted in Fig. 4. It appears that limit-cycle arises in the system from $R_4 = 37\,\Omega$ and dwells up to $R_4 = 97\,\Omega$. This death of limit-cycle oscillations results in the sudden appearance of bursting oscillations through an almost crisis phenomenon. Thereafter, we will use both form of signals (limit-cycle and bursting) for the excitability in an optoelectronic oscillator.
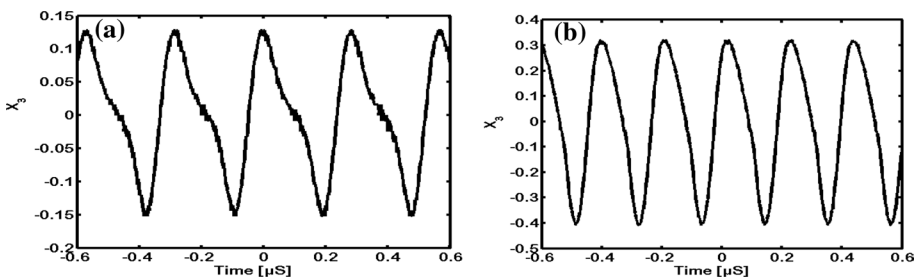
Fig. 3 Other experimental limit-cycles of the Colpitts oscillator. **a** Limit-cycle with the lowest frequency of 3.5 MHz ($R_4 = 40\,\Omega$) and **b** limit-cycle with the highest frequency of 4.76 MHz ($R_4 = 80\,\Omega$)

Fig. 4 Numerical plot of the
bifurcation diagram of the
Colpitts oscillator showing its
different dynamical regimes
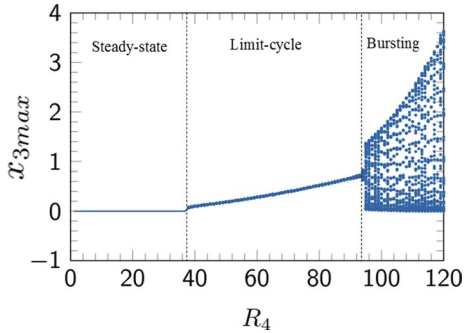
3 Generation of complex optical signals in an optoelectronic oscillator with a Colpitts oscillator

3.1 Circuit description

The proposed OEO with a Colpitts oscillator in its electrical path is referred to as OEO-Colpitts which schematic representation is shown in Fig. 5. This corresponds to the state where K_{in} and K_{out} are on in Fig. 1. The optical signal in the feedback loop is provided by a continuous-wave Distributed Feedback (DFB) laser diode. It delivers power up to 12 mV at the telecom wavelength $\lambda = 1.55\,\mu m$ and is also used to perform the electrical-to-optical conversion via its pump voltage electrode. The threshold of this laser diode is obtained for a pump voltage measured at $V_{th} = 1.02\,V$. The light at the exit of the laser diode is delayed by an optical delay line of time-delay T_D. The delayed optical signal is detected by a fast photodiode with an optical/electrical conversion factor $S = 0.95\,A/W$. When the switch K_{in} is on, this electrical signal feeds the Colpitts oscillator at a particular point of the circuit (V_{in}) and the output is probed at V_{out} (see Fig. 1.a) for the switch K_{out} on and then added to the polarization voltage (V_{pol}) before fed back to the electrode of the laser diode.
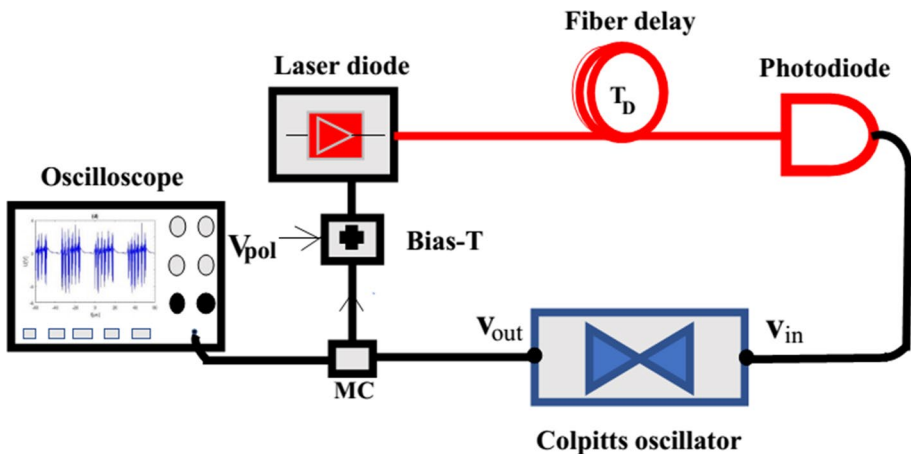
Fig. 5 Experimental set-up of the OEO-Colpitts oscillator. *MC* microwave coupler

A microwave coupler (MC) is used to visualize the signal of the OEO-Colpitts oscillator thanks to a digital oscilloscope.

The different dynamical states of the Colpitts oscillator found in Sect. 2.2 necessarily affect the dynamics of the system as developed hereafter.

3.2 Dynamics of the OEO-Colpitts

The goal here is to study the interaction between the nonlinearity due to the solitary Colpitts oscillator and that of the OEO. We then focus on three parameters of the system to analyze its dynamics: the potentiometer of the Colpitts oscillator, the power of the laser and the length of the optical fiber. In order to analyze the dynamics of the OEO-Colpitts oscillator, two major cases are considered. Firstly, the case where the Colpitts oscillator generates a limit-cycle (potentiometer $R_4 = 50\,\Omega$) and secondly when it emits a bursting oscillation (potentiometer $R_4 = 105\,\Omega$). The question is to see what happens in the optoelectronic systems in these states.

3.2.1 Case with the limit-cycle of the Colpitts oscillator ($R_4 = 50\,\Omega$)

The principal tunable parameter of the OEO-Colpitts oscillator is the polarization voltage V_{pol}. In order to explore experimentally the complex dynamics of the oscillator, we first consider the case where the time-delay is set to zero (the delay line is removed: $T_D = 0$). When the polarization voltage is increased beyond the threshold, a regime of multi-periodic oscillations is observed as displayed in Fig. 6a. This signal oscillates with a maximum frequency equal to $f = 18.18\,\text{MHz}$ and a maximum amplitude of 4.72 V, which are large compared to the oscillation frequency and the maximum amplitude of the solitary Colpitts oscillator found equal to 4.5 MHz and 264 mV, respectively (see Sect. 2.2). Precisely, this frequency is four times the one of the solitary Colpitts oscillator (18.18/4.5 = 4.04).
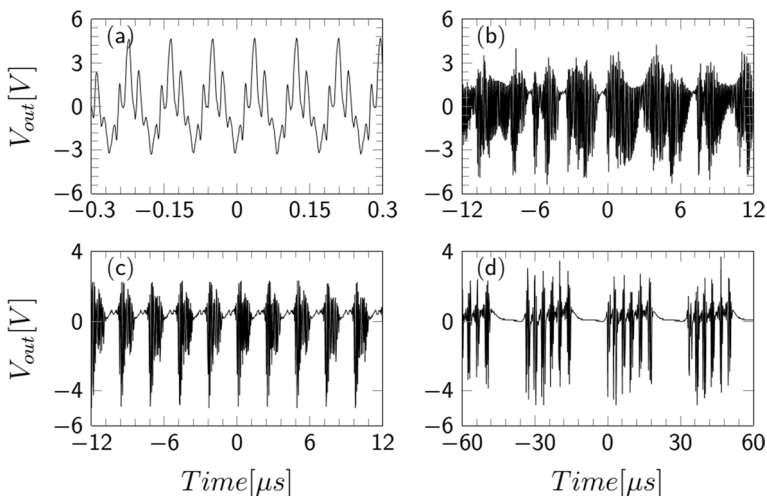
Fig. 6 **a** Multiperiodic, **b** chaotic bursting, **c** periodic bursting, and **d** pulse-package oscillation in the time domain as the polarization voltage is increased beyond the threshold ($T_D = 0$) **a** $V_{pol} = 1.29\,V_{th}$; **b** $V_{pol} = 1.34\,V_{th}$; **c** $V_{pol} = 1.4\,V_{th}$; **d** $V_{pol} = 1.6\,V_{th}$

As the polarization voltage is increased, it appears a chaotic bursting oscillation (see Fig. 6b) and thereafter these bursting become periodic characterized by the fast-scale dynamics superimposed onto a slow-scale, as displayed in Fig. 6c. The frequency of the slow oscillation is equal to 438.6 kHz (frequency of the package) and with a maximum amplitude equal to 2.32 V. The interval between two packages is characterized by a sort of a single oscillation and at the inner of each slow-scale dynamics (package), the chaotic fast-scale dynamics are observed. Thereafter, higher polarization voltage leads the system in a dynamical state corresponding to chaotic pulse-package oscillations observed in Fig. 6d, and the system continues to exhibit these chaotic oscillations until the signal extinguishes (not shown).

In the second consideration and still in the case with the limit-cycle oscillation of the solitary Colpitts oscillator, the time-delay is accounted for (insertion of the optical fiber of length 43 m : $T_D = 0.2\,\mu s$). The system becomes infinite-dimensional. For a value of polarization voltage just beyond the threshold, a multi-periodic dynamics is observed (see Fig. 7a) with a maximum amplitude equal to 6.8 V and with the maximum frequency of the system rather equal to 16.67 MHz. This maximum frequency has slightly decreased (16.67 MHz) compared to the case where the delay line is removed (18.18 MHz) but the maximum amplitude has increased (from 4.7 to 6.8 V). However, when the polarization voltage increases, the system generates other types of multi-periodic states characterized by a fast-scale dynamics alternated by slow-scale dynamics as observed in Fig. 7b with a maximum frequency equal to 13.89 MHz and a maximum amplitude equal to 5.36 V.

Figure 7c shows the enlargement of one package of Fig. 7b unveiling the fast-scale dynamics. This enlargement allows observing that the system has several amplitudes in its dynamics. We find that further increase of the polarization voltage finally drives the system in a regime of chaotic bursting oscillations given in Fig. 7d. Here, the maximum frequency is reached when the polarization voltage is increased just beyond the threshold before gradually drops. Therefore, the insertion of the optical fiber delay line in the system increases the maximum amplitude but also slightly decreases the maximum frequency.
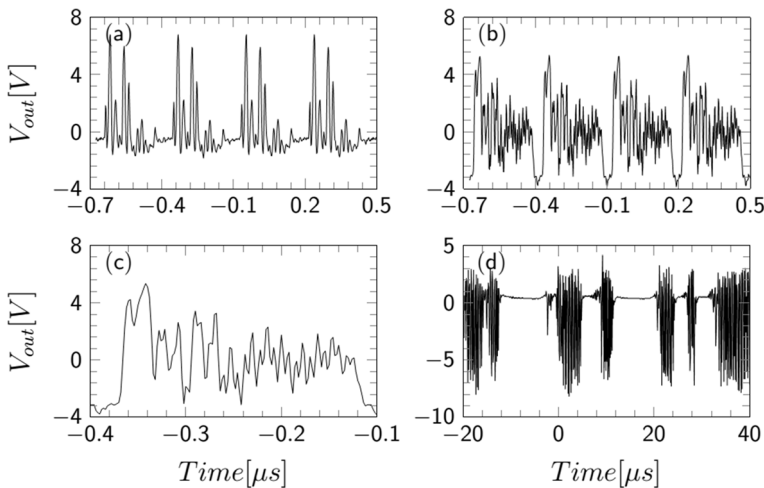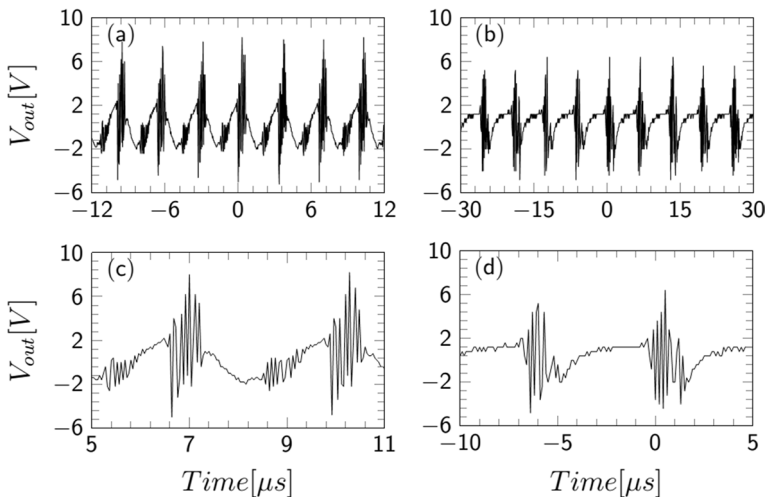

Fig. 7 **a** Multi-periodic, **b** slow-fast dynamics, and **d** chaotic bursting oscillation in the time domain as the polarization voltage is increased beyond the threshold ($T_D = 0.2\,\mu s$). **a** $V_{pol} = 1.09\,V_{th}$; **b** $V_{pol} = 1.24\,V_{th}$; **d** $V_{pol} = 1.54\,V_{th}$; **c** is the enlargement of one package of **b**

3.2.2 Case with the bursting oscillation of the Colpitts oscillator ($R_4 = 105\,\Omega$)

In this case, the similar work is done as in Sect. 3.2.1 but, at the only difference that the solitary Colpitts oscillator is configured to emit bursting oscillations. For the case where the time-delay is set to zero ($T_D = 0\,\mu$s), firstly for the value of the polarization voltage just beyond the threshold, the bursting oscillations are observed (Fig. 8a) with the oscillation frequency corresponding to the one of bursting oscillations of the solitary Colpitts oscillator (2.5 MHz). In this case, one can observe that the maximum amplitude of the system is equal to 8.2 V. These bursting oscillations are characterized by an alternation of two different oscillation packages separated each by some fast-scale dynamics. Furthermore, chaotic bursting oscillations (see Fig. 8b) are obtained when the polarization voltage increases. The enlargements observed in Fig. 8c, d display the inner structures of each package of bursting and chaotic bursting oscillations of Fig. 8a, b, respectively.

Besides, when the delay line is added ($T_D = 0.2\,\mu$s) in the system, the dynamical behavior which is initially chaotic (see Fig. 9a) migrates towards multi-periodic oscillation (Fig. 9b). The maximum frequency corresponding to this multi-periodicity is equal to 195 kHz with a maximum amplitude of 1.4 V. Finally, the system returns to a chaotic state (chaotic bursting) (Fig. 9c, d) when the polarization voltage is increased.

The main difference between the cases without and with the delay line is that one has only bursting oscillation with a maximum amplitude equal to 8.2 V and chaotic bursting oscillation in the first case; but, the multi-periodic oscillation with a maximum amplitude equal to 1.4 V is also observed in the second case.

Fig. 8 Experimental time-traces of the OEO-Colpitts oscillator for $T_D = 0\,\mu$s. **a** Bursting, and **b** chaotic bursting oscillations are observed when the polarization voltage is increased beyond the threshold. **a** $V_{pol} = 1.14\,V_{th}$; **b** $V_{pol} = 1.52\,V_{th}$. **c**, **d** are the enlargements of **a**, **b**, respectively
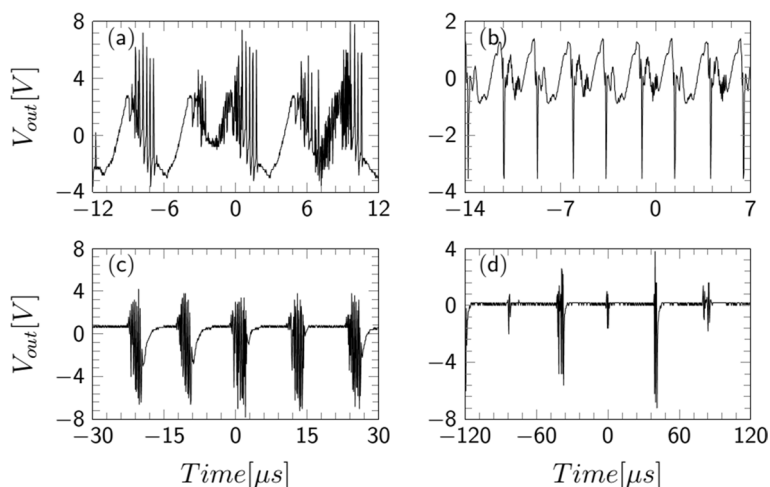
Fig. 9 From chaos to chaotic bursting oscillations. The laser pump voltage is increased beyond the threshold ($T_D = 0.2\,\mu s$); **a** chaos for $V_{pol} = 1.12\,V_{th}$; **b** bursting for $V_{pol} = 1.4\,V_{th}$; **c** beginning of the chaotic bursting for $V_{pol} = 1.6\,V_{th}$; **d** full chaotic bursting for $V_{pol} = 1.74\,V_{th}$

4 Conclusion

In this paper, we have presented a solitary Colpitts oscillator which generates both high frequencies limit-cycle and bursting oscillations when a potentiometer of its circuit evolves. These dynamical states of the Colpitts oscillator have been used to emulate complex fast regular, multiperiodic, bursting, and chaotic bursting oscillations in a simplified optoelectronic oscillator. Two principal cases have been developed: the case where the delay line has been considered and the case where it is removed. The results have shown that this latter case offers higher frequencies bursting oscillations but, might be with slightly lower amplitude compared to the other case. This phenomenon is certainly inherent from the effect of the delay line in the same order as other phenomena such as chaos, amplitude death, and so on observed in delay systems (Lakshmanan and Senthilkumar 2011). Moreover, it is noteworthy that small noises occur in the experimental records mainly in the time intervals within two packages of bursting oscillations (see Figs. 6, 7, 8, 9). We admit that such noises are due to both electronic and optoelectronic components of our OEO-Colpitts oscillator.

On the other hand, comparing both the amplitudes and the frequencies of the solitary Colpitts oscillator and those of the OEO-Colpitts oscillator, it can be noticed that the OEO-Colpitts oscillator displays signals with higher amplitudes and frequencies. Such results could be important in photonic devices requiring the multiplication of amplitude and frequency. Moreover, mixed-mode oscillations of engineering systems including lasers, photonic microwave mixing, or neuromorphic computing using electro-optical systems with feedback could also benefit from the bursting capability. Further research investigations will be devoted to the exploration of multi-loop architectures which would provide extra-degrees of freedom and therefore, a wider variety of dynamical behaviors (Shumakher and Eisenstein 2008; Levy et al. 2010; Nguimdo et al. 2012; Liu et al. 2012).

References

Ai, J., Wang, L., Wang, J.: Secure communications of CAP and OOK signals over MMF based on electro-optic chaos. Opt. Lett. **42**(18), 3662–3665 (2017)

Argyris, A., Syvridis, D., Larger, L., Valerio, A.-L., Colet, P., Fischer, I., Jordi, G.-O., Mirasso, C.R., Luis, P., Shore, K.A.: Chaos-based communications at high bit rates using commercial fiber-optic links. Nature **438**(7066), 343–346 (2005)

Chang, C.Y., Choi, D., Locquet, A., Wishon, M.J., Merghem, K., Ramdane, A., Lelarge, F., Martinez, A., Citrin, D.S.: A multi-GHz chaotic optoelectronic oscillator based on laser terminal voltage. Appl. Phys. Lett. **108**(19), 191109 (2016)

Chembo, Y.K., Hmima, A., Lacourt, P.-A., Larger, L., Dudley, J.M.: Generation of ultralow jitter optical pulses using optoelectronic oscillators with time-lens soliton-assisted compression. IEEE J. Lightw. Technol. **27**(22), 5160–5167 (2009)

Chembo, Y.K., Colet, P., Larger, L., Gastaud, N.: Chaotic breathers in delayed electro-optical systems. Phys. Rev. Lett. **95**(20), 203903(1)–203903(4) (2005)

Chembo, Y.K., Larger, L., Tavernier, H., Bendoula, R., Rubiola, E., Colet, P.: Dynamic in stabilities generated with optoelectronic oscillators. Opt. Lett. **32**(17), 2571–2573 (2007)

Chembo, Y.K., Brunner, P., Jacquot, M., Larger, L.: Optoelectronic oscillators with time-delayed feedback". Rev. Mod. Phys. **91**(3), 035006(51) (2019)

Chengui, G.R.G., Talla Mbé, J.H., Talla, A.F., Woafo, P., Chembo, Y.K.: Dynamics of optoelectronic oscillators with electronic and laser nonlinearities. IEEE J. Quantum Electron. **54**(1), 5000207 (2018)

Chengui, G.R.G., Woafo, P., Chembo, Y.K.: The simplest laser based optoelectronic oscillator: an experimental and theoretical study. J. Light. Technol. **34**(3), 873–878 (2016)

Cohen, A.B., Ravoori, B., Murphy, T.E., Roy, R.: Using synchronization for prediction of high-dimensional chaotic dynamics. Phys. Rev. Lett. **101**(15), 154102 (2008)

Effa, J.Y., Essimbi, B.Z., Mucho, N.J.: Synchronization of Colpitts oscillators with different orders. Commun. Nonlinear Sci. Numer. Simul. **14**(4), 1590–1597 (2009)

Horowitz, P., Hill, W.: The Art of Electronics, 2nd edn. Cambridge University Press, New York (1994)

Huang, N., Li, M., Deng, Y., Zhu, N.H.: Optical pulse generation based on an optoelectronic oscillator with cascaded nonlinear semiconductor optical amplifiers. IEEE Photon. J. **6**(1), 5500208 (2014)

Huang, L., Deng, L., Fu, S., Tang, M., Cheng, M., Zhang, M., Liu, D.: Stable and compact dual-loop optoelectronic oscillator using self-polarization–stabilization technique and multicore fiber. J. Lightw. Technol. **36**(22), 5196–5202 (2018)

Hunter, P.J., Nash, M.P., Sands, G.B.: Computational electromechanics of the heart. In: Panfilov, A.V., Holden, A.V. (eds.) Computational Biology of the Heart, vol. 12, pp. 347–407. Wiley, West Sussex (1997)

Izhikevich, E.M.: Neural excitability, spiking and bursting. Int. J Bifur. Chaos **10**(6), 1171–12660 (2000)

Jerrelind, J., Stensson, A.: Nonlinear dynamics of parts in engineering systems. Chaos Solitons Fract. **11**(15), 2413–2428 (2000)

Jia, S., Yu, J., Wang, Z., Wang, J., Wang, W., Bin, C., Yu, Y.: A novel highly stable dual-wavelengh short optical pulse source based on a dual-loop optoelectronic oscillator with two wavelength. IEEE Photon. J. **7**(4), 1502611 (2015)

Kengne, J., Chedjou, J.C., Kenne, G., Kyamakya, K.: Dynamical properties and chaos synchronization of improved Colpitts oscillators. Commun. Nonlinear Sci. Numer. Simul. **17**(7), 2917–2923 (2012)

Kennedy, M.P.: Chaos in the Colpitts oscillator. IEEE Trans. Circ. Syst. I **41**(11), 771–773 (1994)

Kingni, S.T., Keuninckx, L., Woafo, P., der Sande, G.V., Danckaert, J.: Dissipative chaos, Shilnikov chaos and bursting oscillations in a three-dimensional autonomous system: theory and electronic implementation. Nonlinear Dyn. **73**, 1111–1123 (2013)

Lakshmanan, M., Senthilkumar, D.V.: Dynamics of Nonlinear Time–Delay Systems. Springer, Berlin (2011)

Larger, L., Baylón-Fuentes, A., Martinenghi, R., Udaltsov, V.S., Chembo, Y.K., Jacquot, M.: High-speed photonic reservoir computing using a time-delay-based architecture: million words per second classification. Phys. Rev. X **7**(1), 011015(1)–011015(14) (2017)

Lasri, J., Bilenca, A., Dahan, D., Sidorov, V., Eisenstein, G., Ritter, D., Yvind, K.: A self-starting hybrid optoelectronic oscillator generating ultra-low jitter 10-GHz optical pulses and low phase noise electrical signals. IEEE Photon. Technol. Lett. **14**(7), 1004–1006 (2002)

Lelièvre, O., Crozatier, V., Berger, P., Ghaya, B., Llopis, O., Dolfi, D., Nouchi, P., Fabienne, G., Bretenaker, F., Morvan, L., Pillet, G.: A model for designing ultralow noise single and dual-loop 10-GHz optoelectronic oscillators. J. Lightw. Technol. **35**(20), 4366–4374 (2017)

Levy, E.C., Okusaga, O., Horowitz, M., Menyuk, C.R., Zhou, W., Gary, M.C.: Comprehensive computational model of single-and dual-loop optoelectronic oscillators with experimental verification. Opt. Express **18**(20), 21461–21476 (2010)

Lindberg, E., Tamasevicius, A., Mykolaitis, G., Bumeliene, S.: Approaching threshold frequency in chaotic Colpitts oscillator. Int. J. Bifur. Chaos. **17**(10), 3449–3453 (2007)

Liu, X., Pan, W., Zou, X., Luo, B., Yan, L., Lu, B.: A reconfigurable optoelectronic oscillator based on cascaded coherence-controllable recirculating delay lines. Opt. Express **20**(12), 13296–13301 (2012)

Ly, A., Auroux, V., Zadeh, R.K., Gutierrez, N., Fernandez, A., Llopis, O.: Highly spectrally pure 90-GHz signal synthesis using a coupled optoelectronic oscillator. IEEE Photon. Technol. Lett. **30**(14), 1313–1316 (2018)

Maggio, G.M., De Feo, O., Kennedy, M.P.: Nonlinear analysis of the Colpitts oscillator and application to design. IEEE Trans. Circ. Syst. **46**(9), 1118–1130 (1999)

Maleki, L.: The optoelectronic oscillator. Nat. Photon. **5**(12), 728–730 (2011)

Mykolaitis, G., Tamasevicius, A., Bumeliene, S.: Experimental demonstration of chaos from the Colpitts oscillator in the VHF and the UHF ranges. Electron. Lett. **40**(2), 91–92 (2004)

Nash, P., Hunter, P.J.: Computational mechanics of the heart. J. Elast. **61**(1/3), 112–141 (2000)

Nguimdo, R.M., Chembo, Y.K., Colet, P., Larger, L.: On the phase noise performance of nonlinear double-loop optoelectronic microwave oscillators. IEEE J. Quantum Electron. **48**(11), 1415–1423 (2012)

Okusaga, O., Adles, E.J., Levy, E.C., Zhou, W., Carter, G.M., Menyuk, C.R., Horowitz, M.: Spurious mode reduction in dual injection-locked optoelectronic oscillators. Opt. Express **19**(7), 5839–5854 (2011)

Paquot, Y., Duport, F., Smerieri, A., Dambre, J., Schrauwen, B., Haelterman, M., Massar, S.: Optoelectronic reservoir computing. Sci. Rep. **2**(1), 287(1)–287(6) (2012)

Plant, R.E., Kim, M.: Mathematical description of a bursting pacemaker neuron by a modification of the Hodgkin–Huxley equations. Biophys. J. **16**(3), 227–244 (1976)

Romeira, B., Kong, F., Figueiredo, J.M.L., Javaloyes, J., Yao, J.: High-speed spiking and bursting oscillations in a long-delayed broadband optoelectronic oscillator. IEEE J. Lightw. Technol. **33**(2), 503–510 (2015)

Sherman, A., Rinzel, J., Keizer, J.: Emergence of organized bursting in cluster of pancreatic-cells by channel sharing. J. Biophys. **54**(3), 411–425 (1988)

Shumakher, E., Eisenstein, G.: A novel multiloop optoelectronic oscillator. IEEE Photon. Technol. Lett. **22**(22), 1881–1883 (2008)

Simo, H., Woafo, P.: Bursting oscillations in electromechanical systems. Mech. Res. Commun. **38**(8), 537–541 (2011)

Soriano, M.C., Ortin, S., Brunner, D., Larger, L., Mirasso, C.R., Fisher, I., Pesquera, L.: Optoelectronic reservoir computing: tackling noise-induced performance degradation. Opt. Express **21**(1), 12–20 (2013)

Tamasevicius, A., Mykolaitis, G., Bumeliene, S., Baziliauskas, A., Krivickas, R., Lindberg, E.: Chaotic Colpitts oscillator for the ultrahigh frequency range. Nonlinear Dyn. **44**(1), 159–165 (2006)

Talla, A.F., Martinenghi, R., Woafo, P., Chembo, Y.K.: Breather and pulse-package dynamics in multinonlinear electrooptical systems with delayed feedback. IEEE Photon. J. **8**(4), 7803608 (2016)

Talla Mbé, J.H., Talla, A.F., Chengui, G.R.G., Coillet, A., Larger, L., Woafo, P., Chembo, Y.K.: Mixedmode oscillations in slow-fast delayed optoelectronic systems. Phys. Rev. E **91**(1), 012902-6 (2015)

Talla Mbé, J.H., Kamaha, J.S.D., Chembo, Y.K., Woafo, P.: Dynamics of wideband time-delayed optoelectronic oscillators with nonlinear filters. IEEE J. Quantum Electron. **55**(4), 5000106(1)–5000106(6) (2019a)

Talla Mbé, J.H., Woafo, P., Chembo, Y.K.: A normal form method for the determination of oscillations characteristics near the primary Hopf bifurcation in bandpass optoelectronic oscillators: theory and experiment. Chaos. **29**(3), 033104(1)–033104(7) (2019b)

Uchida, A., Kawano, M., Yoshomori, S.: Dual synchronization of chaos in Colpitts electronic oscillators and its applications for communications. Phys. Rev. E **68**(5), 056207–056211 (2003)

Wu, B., Wang, M., Yue, D., Yu, T., Hongqian, M., Haisu, L., Bin, Y., Yan, F., Zhen, H.: Magnetic field sensor based on a dual-frequency optoelectronic oscillator using cascaded magnetostrictive alloy-fiber Bragg grating–Fabry Perot and fiber Bragg grating Fabry Perot filters. Opt. Express **26**(21), 27628–27638 (2018)

Yao, X.S., Maleki, L.: Optoelectronic microwave oscillator. J. Opt. Soc. Am. B Opt. Phys. **13**(8), 1725–1735 (1996)

Yao, X.S., Davis, L., Maleki, L.: Coupled optoelectronic oscillators for generating both RF signal and optical pulses. IEEE J. Lightw. Technol. **18**(1), 73–78 (2000)

Yao, J.: Optoelectronic oscillators for high speed and high-resolution optical sensing. J. Lightw. Technol. **35**(16), 3489–3497 (2017)

Zhang, Y., Hou, D., Zhao, J.: Long-term frequency stabilization of an optoelectronic oscillator using phase-locked loop. J. Lightw. Technol. **32**(13), 2408–2414 (2014)

Zou, X., Liu, X., Li, W., Li, P., Pan, W., Yan, L., Shao, L.: Optoelectronic oscillators (OEOs) to sensing, measurement, and detection. IEEE J. Quantum Electron. **52**(1), 0601116 (2016)

Power spectrum analysis of time-delayed optoelectronic oscillators with wide and narrow band nonlinear filters

René Mboyo Kouayep[1] · Jimmi Hervé Talla Mbé[2] · Paul Woafo[1]

Abstract

In this paper, we use the fourth-order Runge–Kutta and fast Fourier transform-based spectral analysis to study the power spectrum of the phenomena of multi-periodicity, crenelated, mixed-mode oscillations, and chaos when the values of the bandwidth and the cubic-nonlinear term (CNT) of the filter vary in the cubic-nonlinear optoelectronic oscillator (CN-OEO). On the one hand, when the high and low cut-off frequencies are sufficiently far apart, it is numerically proved that the presence of the CNT reveals the frequency combs generation with a free spectral range equal to the inverse of the time-delay. Likewise, the width of the central peak narrows with the increase of the CNT, showing that the system becomes more and more selective in terms of oscillation frequencies. On the other hand, when the cut-off frequencies are sufficiently close, harmonic and sub-harmonic frequencies are recorded. In either case, CN-OEO displays oscillations whose frequencies remain greater than those of a standard optoelectronic oscillator.

1 Introduction

Delay differential systems are ubiquitous since they are encountered in relevant fundamental and applied fields such as chemical kinetics, fluid dynamics, electronics, biology, optics and photonics, and so on (Argyris et al. 2005; Ge et al. 2005; Li et al. 2009; Emeux 2009; Uchida 2012; Larger et al. 2013; Wang et al. 2017; Huang and Zhang 2019). Particularly in the optical domain, a wide variety of time delayed electro-optical systems was modeled using the so-called Ikeda's equation (Neyer and Voges 1982; Vallée and Delisle 1986). Examples are optoelectronic oscillators (OEOs).

✉ Jimmi Hervé Talla Mbé
    jhtallam@yahoo.fr

1   Laboratory of Modeling and Simulation in Engineering, Biomimetics and Prototypes, Department of Physics, University of Yaoundé I, P.O. Box 812, Yaoundé, Cameroon

2   Research unit of Condensed Matter, Electronics and Signal Processing, Department of Physics, University of Dschang, P.O. Box 67, Dschang, Cameroon

✷ Springer

OEOs are autonomous systems in which a signal is alternatively converted into the optical and electrical domains in a closed-loop configuration (Talla et al. 2016; Chembo et al. 2019). In their standard configuration, OEOs have two sub-families depending on the bandwidth of the electrical path in the feedback loop. On the one hand, when the filter is narrow, the system displays ultra-stable microwave signals (Yao and Maleki 1996; Chembo et al. 2008) with applications in the fields such as aerospace engineering (Maleki 2011), sensing (Zou et al. 2016; Yao 2017; Koualong et al. 2022), time-frequency metrology (Zhang et al. 2014; Saleh et al. 2014), and pulse generation in optical fiber networks (Lasri et al. 2002; Jia et al. 2015). On the other hand, when the filter is broad, OEOs can output other complex optical microwave signals such as breathers, bursting, chaos (Chembo et al. 2005; Weicker et al. 2013) that are applied in optical chaos communications (Argyris et al. 2005; Chengui et al. 2014), random bit generation (Sciamanna and Shore 2015; Zhang et al. 2017; Talla Mbe et al. 2021), and neuromorphic computing (Larger et al. 2012; Martinenghi et al. 2012).

From the discovery of frequency combs with the construction of the first mode-blocked laser (Hargrove et al. 1964), various configurations, including optoelectronic feedback (Chan et al. 2007), optical injection (Juan and Lin 2009), and optical feedback (Zhao et al. 2015) have been developed and analyzed for the generation of microwave frequency combs (MFCs). It is important to clarify that OEOs were also used to display microwave frequency combs (MFCs) (Chembo et al. 2019; Xu et al. 2019; Cheng et al. 2020). Microwave frequency combs (MFCs) (Savchenkov et al. 2016; Chembo 2016) are spectral structures characterized by a discrete and regularly spaced succession of lines and found a multitude of applications in a wide range of fields such as metrology (Yokoyama et al. 2008; Hale et al. 2018), modern instrumentation (Barmuta et al. 2016; Cho et al. 2020), spectroscopy (Coddington et al. 2016), and radar (Gill et al. 1994), to name just a few.

In general, in OEOs, the nonlinearity of the system comes from the optical path, while the electrical path is considered to be linear. However, some recent studies have shown that the insertion of electrical nonlinearities such as the nonlinear capacitor, the Van der Pol, and Colpitts oscillators increase the scope of dynamical behaviors such as a wide variety of periodic, quasiperiodic, chaotic states, and the increase of the frequency of the signal (Talla et al. 2016; Talla Mbé et al. 2019; Kouayep et al. 2020; Kamaha et al. 2020). Among these novel architectures of OEOs, the one with the nonlinear capacitor and called the cubic-nonlinear OEO (CN-OEO) was investigated both theoretically and experimentally with and without Mach-Zehnder modulator (Talla Mbé et al. 2019; Kamaha et al. 2020, 2022). It came out that compared to a standard OEO (that is the one with a standard band-pass filter in the electrical path), the CN-OEO can display chaos for lower feedback gain. Moreover, it routes to chaos through a large region of limit-cycle oscillations of higher frequencies followed by a narrow window of crenelated oscillations instead of breathers as is usually the case. However, the power spectrum analysis of the system was not addressed. Power spectrum analysis is one of the main tools to explore the characteristics of oscillation properties of CN-OEO, notably when some parameters evolve such as the bandwidth of the electrical filter and the characteristic parameter of the nonlinear capacitor.

In this article, we are investigating the power spectral and the dynamical behaviors when the values of the bandwidth and the CNT of the filter vary in the CN-OEO. From the frequency point of view, sub-harmonics, harmonics, and frequency combs generation with a free spectral range (FSR) of 303 kHz are recovered depending on the two cut-off frequencies and the cubic-nonlinear term (CNT).

This paper is organized as follows: The next section (Sect. 2) presents the system and the model. In Sect. 3, the effects of the coil and the CNT on the dynamics and the frequency of

CN-OEO are studied. The case where $L = 10$ µH and $L = 10$ mH are considered. Section 4 presents the influence of the cubic-nonlinear term on the selectivity of characteristic peaks in the power spectrum and the last section (Sect. 5) concludes the article.

2 System and model

The experimental setup of the CN-OEO is presented in Fig. 1 (Talla Mbé et al. 2019; Kamaha et al. 2020). A telecommunication continuous-wave laser diode with wavelength $\lambda_L = 1.55$ µm and power P_{in} seeds a Mach–Zehnder modulator (MZM) characterized by a radio-frequency (RF) and direct-current (DC) half-wave voltages $V_{\pi rf}$ and $V_{\pi dc}$, respectively. The modulated light is retarded by an optical delay line resulting in a time-delay T_D, before being converted to an electrical signal with a photodiode (PD) of responsivity S. The electrical signal generated by the photodiode V_{in} passes through a cubic-nonlinear band-pass filter (CNBPF) that outputs V_{out} and in turn is subjected to an amplification before being re-injected into the RF electrode of the MZM. We notice that the CNBPF is made of a resistor R, a coil L, and a nonlinear capacitor (NC). The nonlinear capacitor is constructed with an operational amplifier U (type LF356), two capacitors $C_{1,2}$, one resistor r, and a mixed assembly of eight simple junction diodes (type IN400X) and whose characteristics are the thermal voltage V_T, the inverse saturation current I_S (Fig. 1b). The number of junction diodes in series is $n = 4$. Combining both Kirchhoff's laws and the general modeling of the wideband OEO, the whole system of Fig. 1 is ruled by the integro-differential delayed equation (Talla Mbé et al. 2019):

$$x + \tau \frac{dx}{dt} + \frac{1}{\theta} \int_0^t x(s)ds + \eta \left(\int_0^t x(s)ds \right)^3 = \beta \cos^2(x(t - T_D) + \phi) \tag{1}$$

where $x = \pi V_{out}/2V_{\pi RF}$ is the dimensionless dynamical variable of the system. Contrary to other OEOs, the particularities of CN-OEO come from the fact that it has the cubic-nonlinear band-pass filter and four timescales which are: the high cut-off time $\tau = L/R$, the low cut-off time $\theta = R/((\frac{1}{C_1}) - \frac{nV_T}{2rI_SC_2})$, the nonlinearity timescale $\sqrt[3]{1/\eta}$ with $\eta = nV_T V_{\pi RF}^2/(12(rRI_SC_2)^3(\pi G)^2)$ representing the cubic-nonlinear coefficient, and the last
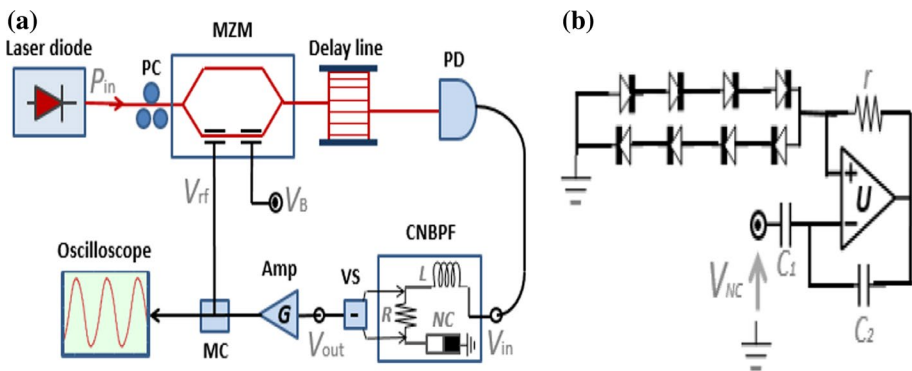
Fig. 1 **a** Set-up of the cubic-nonlinear optoelectronic oscillator. **b** Nonlinear capacitor (NC). PC: Polarization controller. MZM: Mach–Zehnder Modulator. V_B is the offset phase control voltage. PD: Photodiode. CNBPF: Cubic-nonlinear band-pass filter. *VS*: Voltage subtractor. Amp: RF amplifier. MC: Microwave coupler

timescale is the time-delay T_D. The normalized feedback gain and the offset phase are respectively $\beta = \pi SGP_{in}/2V_{\pi RF}$ and $\phi = \pi V_B/2V_{\pi DC}$. Throughout this article, except for the tunable parameters G, L, and P_{in}, we consider the following experimental values of the key parameters (Talla Mbé et al. 2019; Kamaha et al. 2020): $R = 2.5\,k\Omega$, $r = 300\,\Omega$, $C_1 = 270\,pF$, $V_{\pi rf} = 3.9\,V$, $V_{\pi dc} = 5\,V$, $T_D = 3.28\,\mu s$, $S = 0.95\,A/W$, $I_S = 5\,\mu A$, $V_T = 25\,mV$, and $C_2 = 9.15\,nF$.

For mathematical convenience and without loss of generality, the following rescalings are done $v = t/\theta$, $\sigma = T_D/\theta$, $x_\sigma = x(v - \sigma)$, $y = -\frac{1}{\theta}\int_0^t x(s)ds$, $\rho = \eta\theta^3$, and $\varepsilon = \tau/\theta$, so that Eq. (1) can be rewritten in the form of the following flow:

$$\varepsilon\dot{x} = -x + y + \rho y^3 + \beta\cos^2(x_\sigma + \phi) \tag{2}$$

$$\dot{y} = -x \tag{3}$$

The fixed point (x_0, y_0) of Eqs. (2) and (3) yields $x_0 = 0$ and y_0 satisfying the third-order polynomial $\rho y_0^3 + y_0 + \beta\cos^2\phi = 0$. As the gain evolves, Hopf bifurcation can occur at $\gamma_H = \beta_H\sin(2\phi)$ and the system exhibits limit-cycle oscillations with frequency ω_H such that (Kamaha et al. 2020):

$$\omega_H = \sqrt{\frac{\frac{3\delta}{2}\left(-1 + \sqrt{1 + \frac{4\sigma^3\xi}{3\delta^2}}\right)}{\sigma^3}}, \tag{4}$$

at the effective normalized gain

$$\gamma_H = -1 - \frac{(\omega_H\sigma)^2}{2} + \frac{(\omega_H\sigma)^4}{24}, \tag{5}$$

where $\delta = \varepsilon + \sigma = \frac{1}{\theta}\left(\frac{L}{R} + T_D\right)$ and $\xi = (1 + 3\rho y_0^2)$.

To investigate the effect of the bandwidth of the filter, it is possible to tune either the high or the low cut-off time. It is preferable to deal with the high cut-off time by monitoring the coil since it could not affect other parameters of the system. By doing so, reducing the value of the coil L decreases τ while increasing L increases τ. Typically, a filter is considered as wideband (narrowband) filter if the bandwidth spans more than (less than or equal) a decade in frequency (Chembo et al. 2019).

The following sections deal with the dynamical behavior as well as the corresponding spectrum for different values of the coil. The results presented are obtained from the numerical simulations of the set of Eqs. (2) and (3) using the fourth-order Runge–Kutta method for delay differential equations (Lakshmanan and Senthilkumar 2011). Time series and phase portraits are displayed, and the fast Fourier transform is utilized to compute the power spectra.

3 Effect of the coil on the dynamics of CN-OEO

According to Eq. (1), changing the coil L modifies the value of the high cut-off time τ and then changes the width of the band-pass filter.

3.1 Case where $L = 10\,\mu H$ (wideband nonlinear filter)

In this subsection, the value of the coil is fixed at $L = 10\,\mu H$, corresponding to a high cut-off time $\tau = 4\,ns$ that is $f_H = 39.8$ MHz. Besides, the low cut-off time is $\theta = 41\,\mu s$ (i.e $f_L = 3.9$ kHz). Then, the bandwidth is four decades corresponding to a wideband configuration. The Sects. 3.1.1 and 3.1.2 respectively address the different dynamical behaviors through the bifurcation diagrams and their corresponding power spectra for some values of the CNT ρ.

3.1.1 Dynamical behaviors

The full bifurcation diagrams and the maximum Lyapunov exponents of the system without (Fig. 2a, d) and with (Fig 2b, e, and c, f) the CNT present the various dynamical states that can be obtained as the effective normalized gain $\gamma = \beta sin(2\phi)$ is varied.

The bifurcation diagram (Fig 2a) and the Lyapunov exponent (Fig 2d) of the standard OEO (the case with $\rho = 0$) depicts the usual sequence: Fixed point for $|\gamma| \leq 1$; limit-cycles for γ above 1 which frequency decreasing as γ increases; mixed-mode oscillations from $|\gamma| \geq 1.57$. Mixed-mode oscillations also known as breathers are trajectories of a dynamical system in which there is an alternation between oscillations of distinct large and small amplitudes (Chembo et al. 2005; Talla Mbé et al. 2015). The multiple lines of the bifurcation diagram mark an increase of small amplitude oscillations of these mixed-mode oscillations as the effective normalized gain γ evolves routing to chaos from $|\gamma| \geq 2.5$.
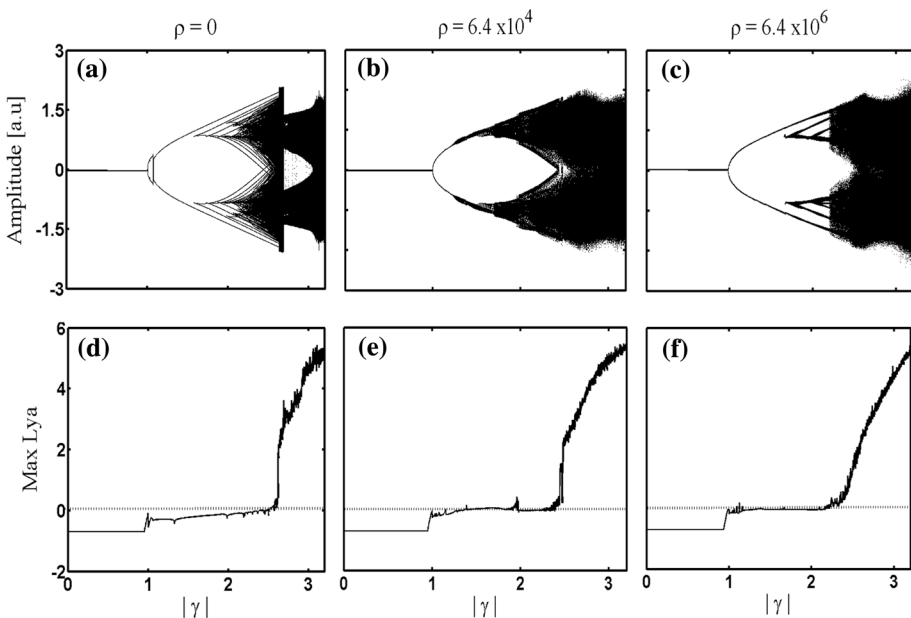
Fig. 2 Bifurcation diagrams and maximum Lyapunov exponents of: **a** and **d**, the standard OEO ($\rho = 0$) [i.e. without the cubic-nonlinear term in Eq. (2)]; (**b** and **e**) and (**c** and **f**) for the CN-OEO (i.e. with cubic-non-linear term in Eq. (2) corresponding to $\rho = 6.4 \times 10^4$ and $\rho = 6.4 \times 10^6$, respectively). $\phi = -\pi/4$

Figure 2b, e show the evolution of the amplitude as the effective normalized gain increases when the CNT $\rho = 6.4 \times 10^4$ is considered in Eq. (2). Periodic oscillation dominates until $|\gamma|$ is close to 2.35. Just above this value, chaotic behavior appears in the system. Compared to the case of Fig. 2a, one first observes that the threshold of the effective normalized gain is not considerably affected by the CNT ($|\gamma_{th}| = 1$). Secondly, one notes that the region in form of a circular arc observed in the case of standard OEO just after the threshold value no longer exists. Thirdly, the chaotic dynamics appears a little earlier; that is $|\gamma| = 2.35$ for $\rho = 6.4 \times 10^4$ whereas it was $|\gamma| = 2.5$ for $\rho = 0$. When the CNT is increased ($\rho = 6.4 \times 10^6$), the threshold value of γ remains at $|\gamma_{th}| = 1$. However, the value of γ from which chaos emerges in the system has reduced again; it is now equal to 2.15 (see Fig. 2c, f).

The following subsubsection analyses the spectra of the signals at different levels of the bifurcation diagrams.

3.1.2 Spectral response

Figure 3 shows the times series, the power spectra, and the phase portraits of the standard OEO ($\rho = 0$) for different values of the effective normalized gain chosen above the threshold. For instance, $|\gamma| = 1.05$ (Fig. 3a1–a3), the time series is a relaxation oscillation whose fundamental frequency is about 300 kHz corresponding to a region in the form of a circular arc (see Fig. 2a) confirmed by a phase portrait showing a slow-fast dynamical limit-cycle. For $|\gamma| = 1.1$ (Fig. 3b1–b3), another limit-cycle oscillation similar to sinusoid (Fig. 3b1) is observed in the time series, with a fundamental frequency of about 13.75 kHz and two harmonic frequencies of 27.5 and 41.25 kHz revealed by the power spectrum. Limit-cycle oscillation turns into relaxation oscillation having a lower fundamental frequency (12 kHz) and more harmonics, but with a form different from that obtained when $|\gamma| = 1.05$ (Fig. 3c1–c3) for $|\gamma| = 1.5$. The fundamental frequency is continuously decreasing with the increase of γ as well as the number of harmonics of these fundamental frequencies. Such growth precedes mixed-mode oscillations (see Fig. 3d1–d3 for $|\gamma| = 2.3$). The fundamental frequency of large amplitudes showed in the power spectrum has also reduced to 8 kHz, and the phase portrait reveals that the breathers are symmetrical. Chaotic behavior dominates the dynamics at higher values of $|\gamma|$; for instance, $|\gamma| = 2.65$ (Fig. 3e1–e3), one has a flat broaden power spectrum and a phase portrait exhibiting a strange attractor.

Figure 4 displays the time series, the power spectrum, and the phase portraits of this system for different values of the effective normalized gain above the threshold when the CNT is different from zero ($\rho = 6.4 \times 10^4$). For $|\gamma| = 1.05$ (Fig. 4a1–a3), the time series exhibit a limit-cycle oscillation where the fundamental frequency f_0 is about 2.1 MHz corresponding to the peak of larger amplitude. The two other peaks of the spectrum are equally distant from the fundamental frequency with a spacing equal to the inverse of the time-delay ($1/T_D = 303$ kHz). Furthermore, we can also observe side lobes that appear periodically indicating multiples of the combs spacing frequency $\kappa \cdot 1/T_D$ where κ being a strictly positive integer. This frequency $\Omega_{FSR}/2\pi = 1/T_D = 303$ kHz is also called the free spectral range (Chembo et al. 2007). The single-phase portrait loop confirms the time series. As in the case of the standard OEO, the value of $|\gamma| = 1.5$ emulates relaxation oscillation with a reduced fundamental frequency of about $f_0 = 1.2$ MHz, but having different amplitudes (Fig. 4b1) as confirmed by the phase portrait of Fig. 4b3. Compared to the case of $|\gamma| = 1.05$, the frequency combs are more important (Fig. 4b2). When $|\gamma| = 2$ (Fig. 4c1–c3), in the time series, one can note that the system displays mixed-mode
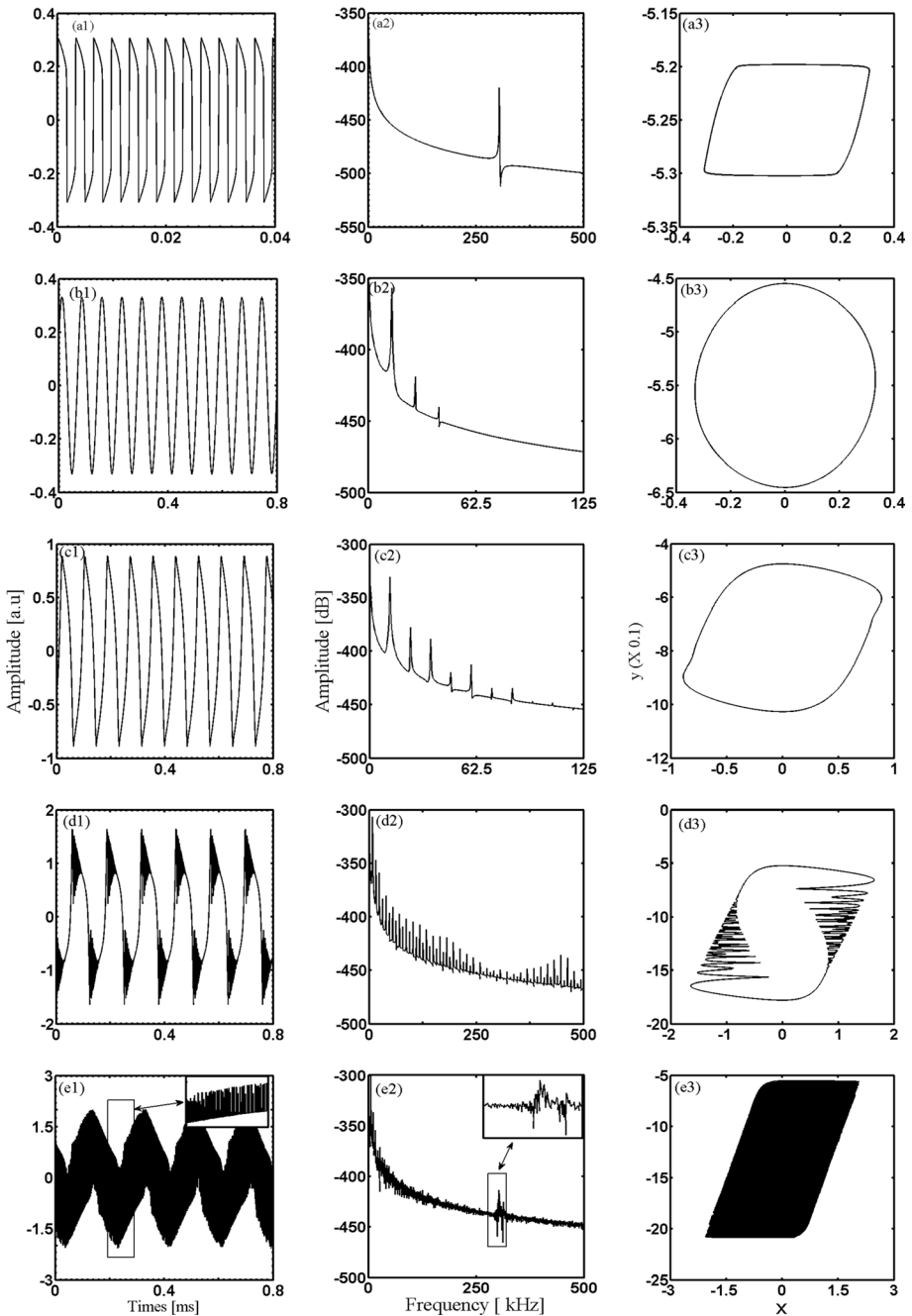
Fig. 3 Time series (first column), power spectra (second column), and phase portraits (third column) for the standard OEO ($\rho = 0$) at different values of γ. $|\gamma| = 1.05$ (**a1–a3**), $|\gamma| = 1.1$ (**b1–b3**), $|\gamma| = 1.5$ (**c1–c3**), $|\gamma| = 2.3$ (**d1–d3**), and $|\gamma| = 2.65$ (**e1–e3**)
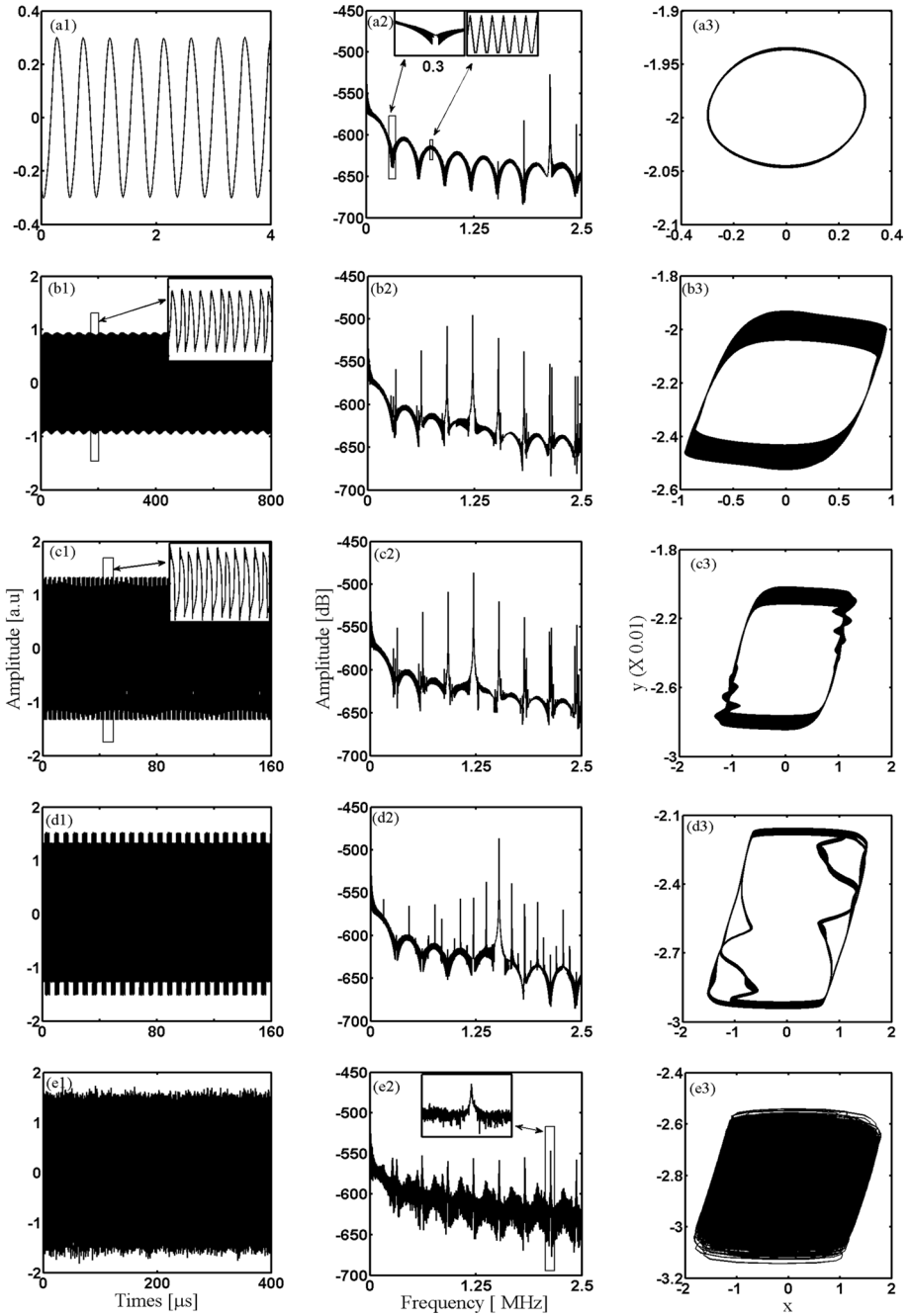
Fig. 4 Time series (first column), power spectra (second column), and phase portraits (third column) for the CN-OEO ($\rho = 6.4 \times 10^4$) at different values of γ. $|\gamma| = 1.05$ (**a1–a3**), $|\gamma| = 1.5$ (**b1–b3**), $|\gamma| = 2$ (**c1–c3**), $|\gamma| = 2.3$ (**d1–d3**), and $|\gamma| = 3.1$ (**e1–e3**)

oscillations with modulated amplitude. The power spectrum shows a curve similar to the previous case, with the same fundamental frequency but, a slightly larger amplitude is observed. These mixed-mode oscillations with modulated amplitude become important and crenelated oscillations occur at large value of the normalized gain $|\gamma| = 2.3$ (Fig. 4d1–d3). Crenelated oscillation displays two types of dynamics: the slow dynamics characterized by square-oscillations of the plateau and the fast dynamics representing the oscillations inside the plateau. The power spectrum indicates the fundamental frequency at a value of 1.5 MHz but with multiple peaks. The phase portrait shows the form of oscillations contained in each dynamics. For higher values of γ, the system exhibits a chaotic behavior (Fig. 4e1–e3 for $|\gamma| = 3.1$).

For the following case, we increase the value of the CNT to $\rho = 6.4 \times 10^6$. The results are displays in Fig. 5. Topologically, one can witness that as γ grows, the system exhibits dynamic features similar to the case where $\rho = 6.4 \times 10^4$ (see Fig. 4). That is the evolution from limit-cycle oscillation at an early value of γ ($|\gamma| = 1.05$ and $|\gamma| = 1.5$ for Fig. 5a1–a3 and b1–b3, respectively) then, mixed-mode oscillations ($|\gamma| = 2$ for Fig. 5c1–c3), crenelated oscillations ($|\gamma| = 2.5$ for Fig. 5d1–d3), and finally chaotic behavior ($|\gamma| = 3.1$ for Fig. 5e1–e3). Moreover, limit-cycle oscillations present packages of frequency combs with the same combs spacing ($303\ kHz \simeq 1/T_D$ and see Fig. 5b2 and c2) i.e same free spectral range as in the case where $\rho = 6.4 \times 10^4$. Nevertheless, it is important to notice that the differences are at the level of the fundamental oscillation frequencies ($f_0 = 5.8$ MHz, $f_0 = 4.3$ MHz, and $f_0 = 3.7$ MHz for $\rho = 6.4 \times 10^6$ against $f_0 = 2.1\ MHz$, $f_0 = 1.2$ MHz, and $f_0 = 1.2$ MHz for $\rho = 6.4 \times 10^4$ when $|\gamma| = 1.05$, $|\gamma| = 1.5$, and $|\gamma| = 2$, taken respectively for the two cases) and the spectrum envelope (when the value of γ increases, the envelope of the spectrum keeps the same shape in the limit-cycle oscillations and whose fundamental frequency remains the only peak of great amplitude for the case $\rho = 6.4 \times 10^6$).

In either case, the frequency combs are observed in the presence of the CNT and are characterized mainly by their k-th frequency components f_k given by $f_k = f_0 + k \cdot 1/T_D$, where f_0 is the fundamental frequency corresponding to the frequency associated with the phase shift between two successive laser pulses, $1/T_D = \Omega_{FSR}/2\pi = 303$ kHz is the free spectral range (Udem et al. 2002).

The following section consists of increasing the value of the coil. This increase brings the two cut-off times closer.

## 3.2 Case where $L = 10$ mH (Narrowband nonlinear filter)

In this part, the procedure is similar to that done in Sect. 3.1 with the difference that only the value of the coil is modified and is taken equal to $L = 10$ mH. It results that, the value of the high cut-off time is $\tau = 4$ μs and the low cut-off time $\theta = 41$ μs corresponding to respective frequencies $f_H = 39.8$ kHz and $f_L = 3.9$ kHz. Thus, the bandwidth is one decade indicating a narrowband configuration. Several other phenomena and dynamical behaviors might occur in the system.

3.2.1 Dynamical behaviors

To better appreciate the frontiers between the different dynamical regimes of the standard OEO and CN-OEO, numerical bifurcation diagrams, and their corresponding maximum Lyapunov exponents are plotted in Fig. 6. For three cases $\rho = 0$, $\rho = 6.4 \times 10^4$,
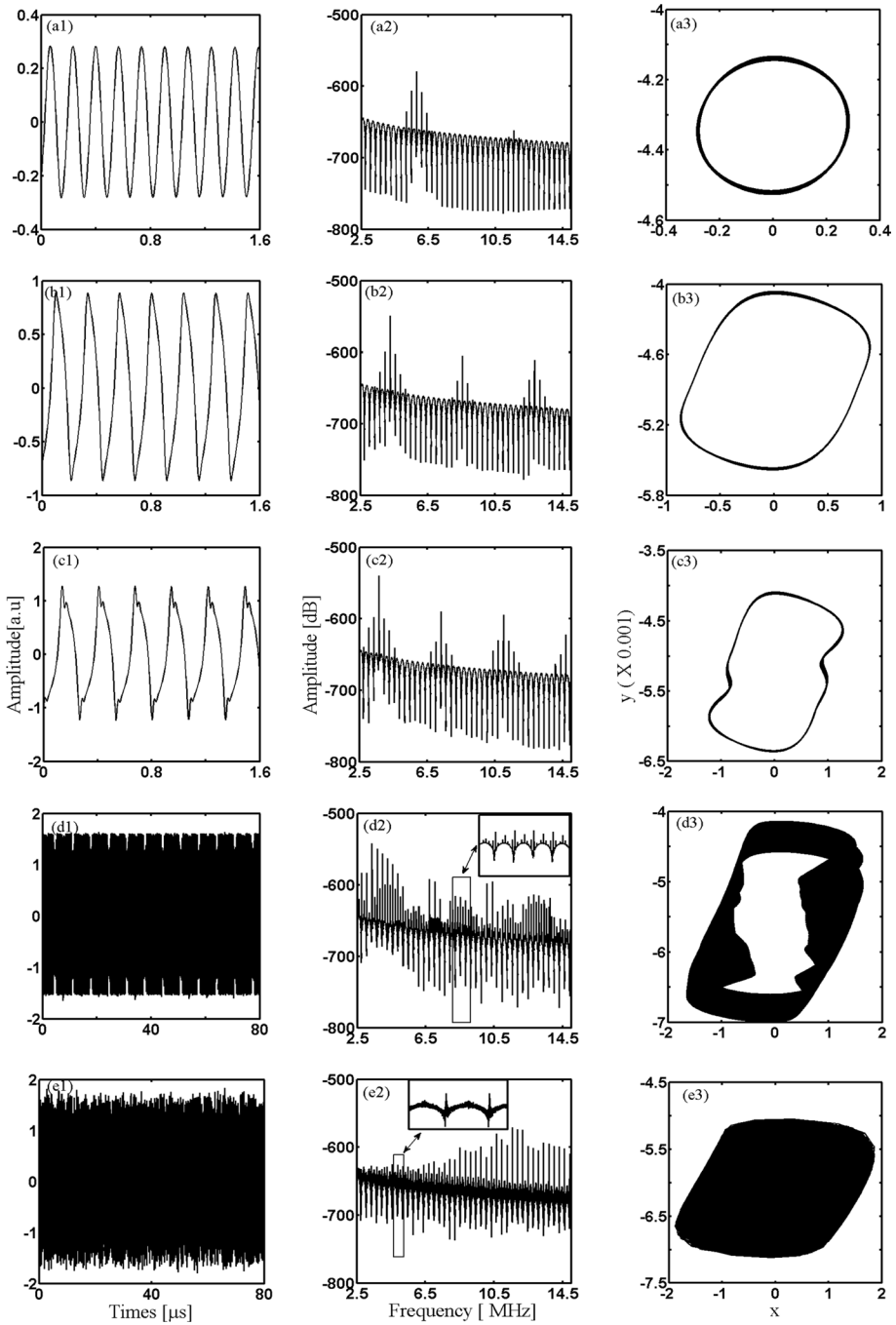
Fig. 5 Time series (first column), power spectra (second column), and phase portraits (third column) for the CN-OEO ($\rho = 6.4 \times 10^6$) at different values of γ. $|\gamma| = 1.05$ (**a1–a3**), $|\gamma| = 1.5$ (**b1–b3**), $|\gamma| = 2$ (**c1–c3**), $|\gamma| = 2.5$ (**d1–d3**), and $|\gamma| = 3.1$ (**e1–e3**)
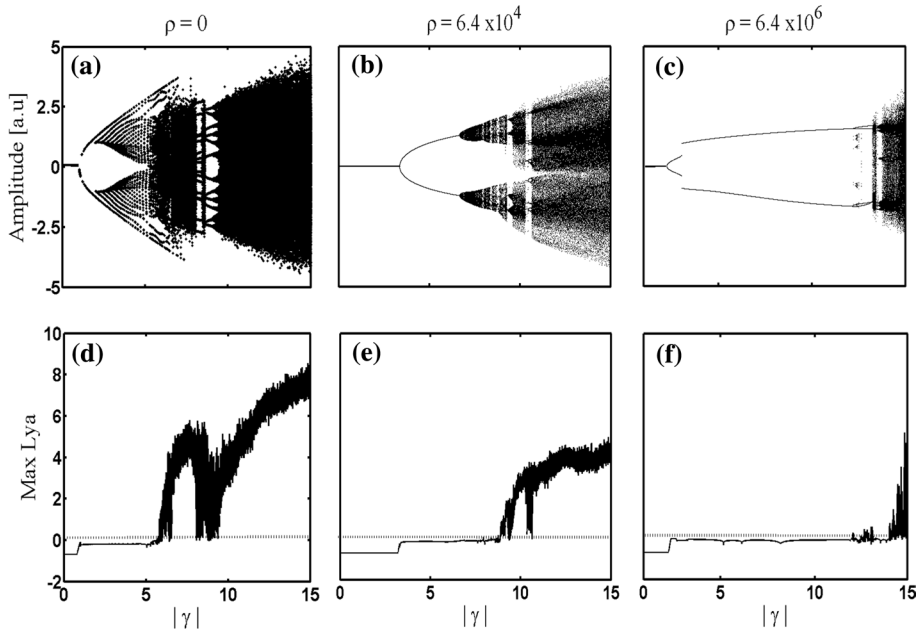
Fig. 6 Bifurcation diagrams and maximum Lyapunov exponents of: **a** and **d**, the standard OEO ($\rho = 0$) [i.e. without cubic-term in Eq. (2)]; (**b** and **e**) and (**c** and **f**), the CN-OEO (i.e. with cubic-term in Eq. (2) corresponding to $\rho = 6.4 \times 10^4$ and $\rho = 6.4 \times 10^6$, respectively). $\phi = -\pi/4$

and $\rho = 6.4 \times 10^6$, these bifurcation diagrams and Lyapunov exponents qualitatively display similar results. That is the dynamics globally commences with fixed-point followed by a Hopf-bifurcation characterized by limit-cycle oscillations which dwell until a certain value of the bifurcation parameter, where mixed-mode oscillations and period-doubling take place; the further increase of the bifurcation parameter leads the system into chaotic motions (see Figs. 6 and 2 for some value of ρ, respectively). However, there are several important differences that merit being underlined. The first one is about the order of the values of γ in the bifurcation diagram. The order of γ in the bifurcation diagram for $L = 10$ mH is higher compared to the case of $L = 10$ µH for the same value of the CNT. Consequently, the threshold value for the Hopf bifurcation is larger. When $L = 10$ µH, $|\gamma_{th}|$ conserved the same value of the threshold ($|\gamma_{th}| = 1$) no matter the value of ρ (see Fig. 2). But, Fig. 6 shows that $|\gamma_{th}| = 1$ for $\rho = 0$, $|\gamma_{th}| = 3.36$ for $\rho = 6.4 \times 10^4$, and $|\gamma_{th}| = 1.3$ for $\rho = 6.4 \times 10^6$. Besides, the CNT makes the chaotic dynamics occurring a little later (in Fig. 6, $|\gamma| = 5.85$ for $\rho = 0$, $|\gamma| = 9.2$ for $\rho = 6.4 \times 10^4$ and $|\gamma| = 12.3$ for $\rho = 6.4 \times 10^6$). The second thing to underline concerns the case where $\rho = 6.4 \times 10^6$. Comparing Figs. 2c, f and 6c, f, it is remarkable that the routes to chaos are different. Mixed-mode oscillations are not pronounced for Fig. 6c and chaos arise almost abruptly through a crisis phenomenon.

The next section consists of taking some values of the effective normalized gain above the threshold value and observing the response of the system from the spectral point of view.

3.2.2 Spectral response

For the first case where the coefficient of the CNT is zero (standard OEO), our simulation shows some spectral states corresponding to each dynamical behavior that we can observe in Fig. 7. Thus, taking a value of γ just above the threshold $|\gamma| = 1.05$ (Fig. 7a1–a3), a limit-cycle oscillation occurs in the time series and whose fundamental frequency is equal to 9.5 kHz and its harmonic (19 and 28.5 kHz) as can be seen in the Fourier spectrum. The trajectories of the phase portrait show a clear limit-cycle. The system can also exhibit relaxation oscillation whose fundamental frequency is equal to 8.25 kHz and several other harmonics appearing in the power spectrum whose intensity decreases until completely attenuates (Fig. 7b1–b3 for $|\gamma| = 1.5$). Such relaxation oscillation transforms into symmetric mixed-mode oscillation whose maximum amplitude of oscillations is equal to 2.7 (Fig. 7c1 and c3 for $|\gamma| = 4.8$) and the power spectrum indicates their fundamental frequency at a value equal to 3.5 kHz (Fig. 7c2). Small amplitude oscillations are symmetrical as shown in the phase portrait (Fig. 7c3). Mixed-mode oscillations progressively grows with the effective normalized gain and chaotic mixed-mode oscillation is recorded (Fig. 7d1–d3 for $|\gamma| = 6.3$). Chaos does not dwell for higher values of $|\gamma|$. For instance, at $|\gamma| = 9.1$, the system behaves with a multi-periodic oscillation whose fundamental frequency is about 42.5 kHz. However, the system returns into a full chaotic state from $|\gamma| = 9.5$ (see Fig. 6a, d).

Figure 8 shows the dynamic behavior and the corresponding power spectra for some values of the effective normalized gain when the CNT is $\rho = 6.4 \times 10^4$. For this case, the threshold value of the effective normalized gain is obtained for a value equal to 3.36. Taking the value of the effective normalized gain equal to 3.45 (Fig. 8a1–a3), the almost sinusoidal oscillation is produced. The related power spectrum indicates that the fundamental frequency is about 245 kHz and a harmonic equal to 490 kHz. For $|\gamma| = 8.8$ (Fig. 8b1–b3), the periodic waveform with fourteen distinct peak intensities are shown in the time series, the sub-harmonic frequency appears in the power spectrum whose the first is about 17.5 kHz i.e the fundamental frequency (245 kHz) divided by fourteen and the corresponding phase portrait shows also fourteen loops that are intertwined together. This can lead to irregular fluctuation in the peak intensities of the time series characterized by a broader power spectrum and a strange attractor (Fig. 8c1–c3 for $|\gamma| = 9.7$). The windows displayed by the bifurcation diagram of Fig. 6b demonstrates the presence of periodic oscillations as witnessed by the 3-T period oscillation of Fig. 8d1–d3 for $|\gamma| = 10.5$. Three peaks with different intensities emerge in the time series (Fig. 8d1), the sub-harmonic frequency appears in the power spectrum (Fig. 8d2) whose the first is about 84 kHz (the fundamental frequency divided by three). The corresponding phase portrait shows three loops. As the effective normalized gain is increased ($|\gamma| = 12$ for Fig. 8e1–e3), chaotic dynamics are definitely observed.

Now, we increase the value of the CNT to $\rho = 6.4 \times 10^6$ and the results are shown in Fig. 9. Compared to the case where $\rho = 6.4 \times 10^4$ (Fig. 8), the system presents different ranges of the effective normalized gain but one can attest a similarity, namely that the route to chaos is made only through the period-doubling (of different periods). However, it is more interesting to notice some differences summarized in Table 1. Indeed, Table 1 reveals that for a value just above the threshold value of γ ($\gamma = 3.45$ for $\rho = 6.4 \times 10^4$ and $\gamma = 1.5$ for $\rho = 6.4 \times 10^6$), one notice a period-1 dynamics for both cases (see lines 2 and 7). On the other hand, while one observes changes in the fundamental frequency, harmonics, and sub-harmonics frequencies for $\rho = 6.4 \times 10^4$ when γ
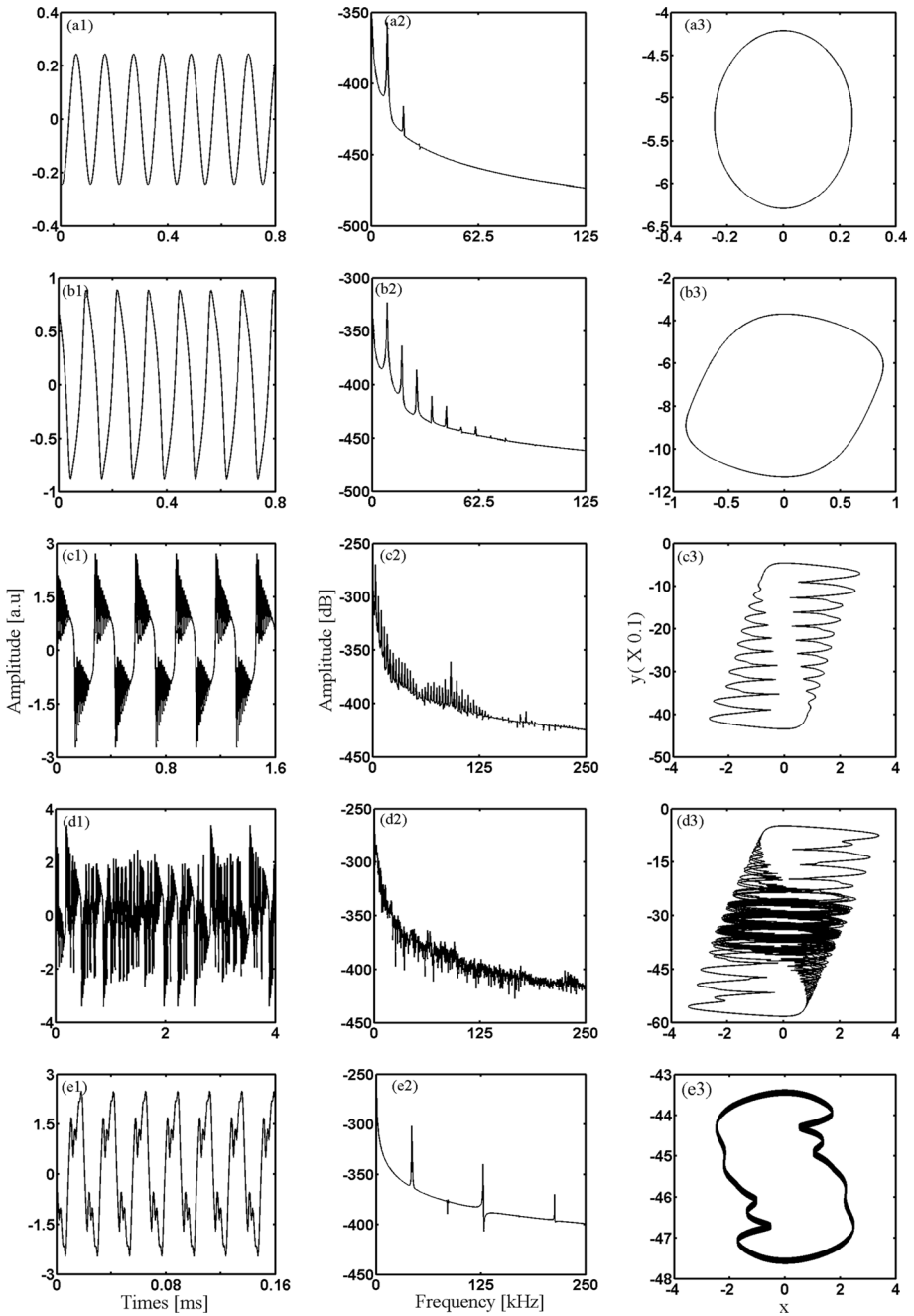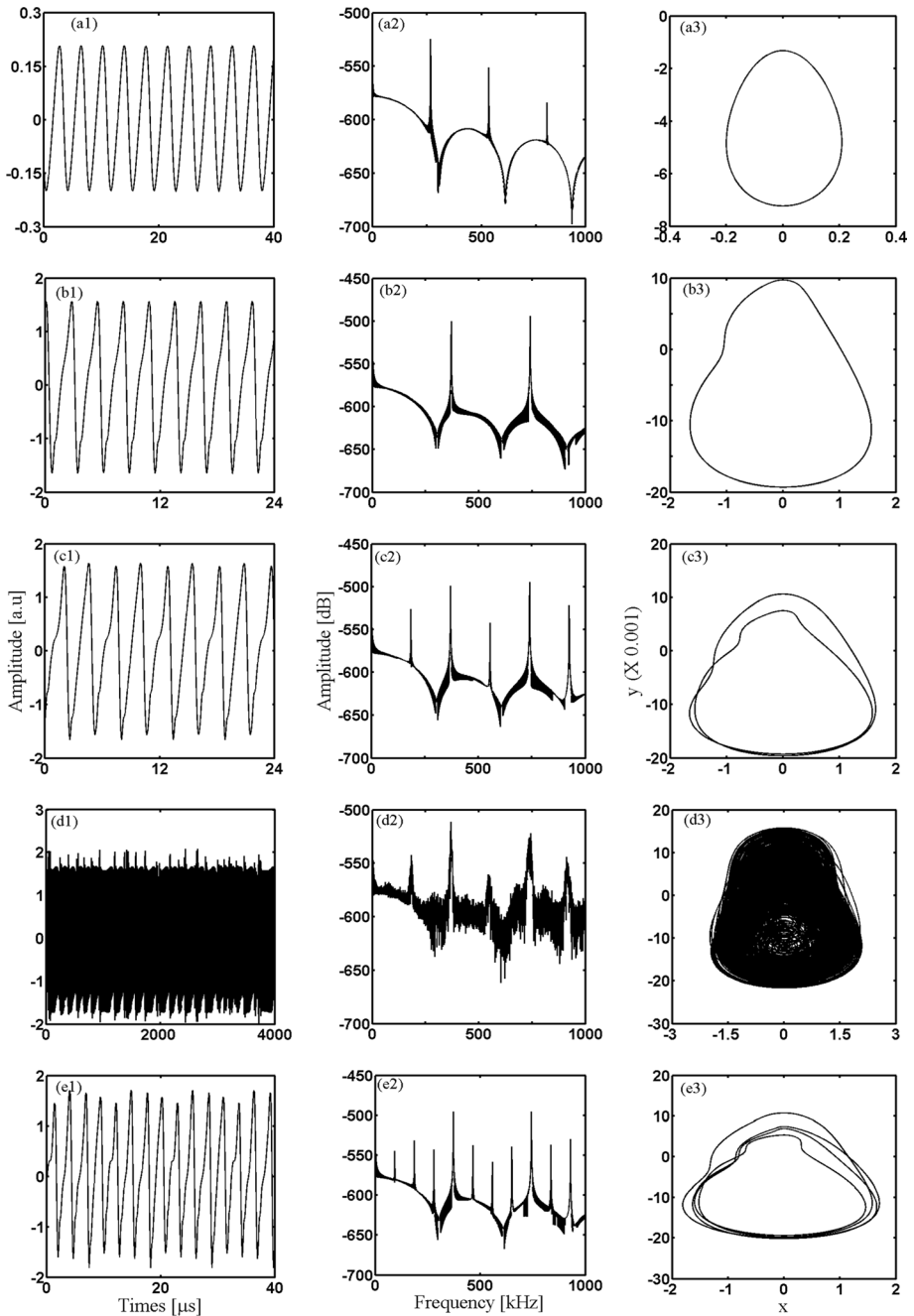
Fig. 7 Time series (first column), power spectra (second column), and phase portraits (third column) for the standard OEO ($\rho = 0$) at different values of γ. $|\gamma| = 1.05$ (**a1–a3**), $|\gamma| = 1.5$ (**b1–b3**), $|\gamma| = 4.8$ (**c1–c3**), $|\gamma| = 6.3$ (**d1–d3**), and $|\gamma| = 9.1$ (**e1–e3**)
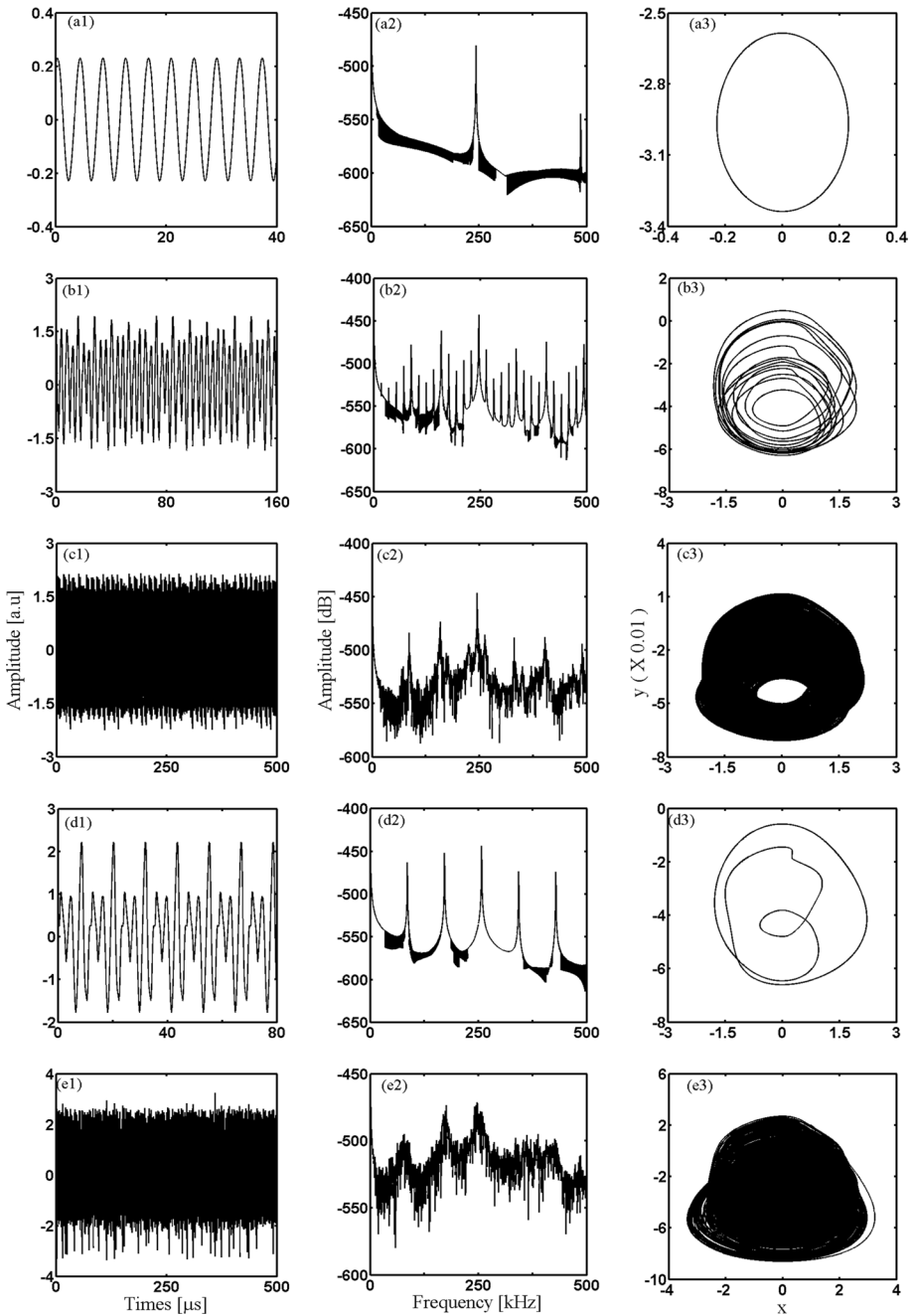
Fig. 8 Time series (first column), power spectra (second column), and phase portraits (third column) for the CN-OEO ($\rho = 6.4 \times 10^4$) at different values of γ. $|\gamma| = 3.45$ (**a1**–**a3**), $|\gamma| = 8.8$ (**b1**–**b3**), $|\gamma| = 9.7$ (**c1**–**c3**), $|\gamma| = 10.5$ (**d1**–**d3**), and $|\gamma| = 12$ (**e1**–**e3**)

Fig. 9 Time series (first column), power spectra (second column), and phase portraits (third column) for the CN-OEO ($\rho = 6.4 \times 10^6$) at different values of γ. $|\gamma| = 1.5$ (**a1–a3**), $|\gamma| = 10.8$ (**b1–b3**), $|\gamma| = 11.8$ (**c1–c3**), $|\gamma| = 12.5$ (**d1–d3**), and $|\gamma| = 13.5$ (**e1–e3**)

Table 1 Some differences with the increase of the effective normalized gain in presence of the cubic-non-linear term when $L = 10$ mH. (F.F: Fundamental Frequency; F.S.H.: First Sub-Harmonic; F.H.: First Harmonic)

| $|\gamma|$	ρ	Dynamics (number of periods)	F.F (kHz)	F.S.H (kHz)	F.H (kHz)	Figures
3.45	6.4×10^4	Periodic (One)	245	None	490	8a1–a3
8.8	6.4×10^4	Periodic (Fourteen)	245	17.5	262.5	8b1–b3
9.7	6.4×10^4	Chaos	None	None	None	8c1–c3
10.5	6.4×10^4	Periodic (Three)	252	84	336	8d1–d3
12	6.4×10^4	Chaos	None	None	None	8e1–e3
1.5	6.4×10^6	Periodic (One)	265	None	530	9a1–a3
10.8	6.4×10^6	Periodic (One)	370	None	740	9b1–b3
11.8	6.4×10^6	Periodic (Two)	370	185	555	9c1–c3
12.5	6.4×10^6	Chaos	None	None	None	9d1–d3
13.5	6.4×10^6	Periodic (Four)	360	90	450	9e1–e3

varies from 3.45 to 10.5 (see lines 2, 3, 4, 5 and Fig. 6b), the dynamic behavior for the case where $\rho = 6.4 \times 10^6$ remains at one period for practically the same range of the variation of γ (1.5 to 10.8: see lines 7, 8 and Fig. 6c). The chaotic dynamics occurs a little far when the value of the CNT ρ passes from 6.4×10^4 to 6.4×10^6 (see lines 4, 6, and 10). Another difference is that when the CNT passes from $\rho = 6.4 \times 10^4$ to $\rho = 6.4 \times 10^6$, the side lobes appear in the power spectrum.

4 Influence of the cubic-nonlinear coefficient on the selectivity of characteristic peaks

This section shows the influence of the CNT on the central peak when the value of the coil and that of the effective normalized gain taken just above the threshold value are maintained fixed.

From this figure, when ρ increases (black to the blue of Fig. 10), the appearance of low-intensity peaks around the central peak shows a kind of translation towards the smaller intensities. Besides, that reduction in intensity is accompanied by a narrowing in the width of the central peak. The fact that the width of the central peak narrows with the increase of ρ demonstrates that the system becomes more and more selective in terms of oscillation frequencies. (Color figure online)

Fig. 10 Power spectra: black for $\rho = 0$, blue for $\rho = 6.4 \times 10^4$, and—red when the value of the cubic-nonlinear term increases ($\rho = 6.4 \times 10^6$). For these three cases, $L = 10$ μH and the value of the effective normalized gain remains the same $|\gamma| = 1.05$
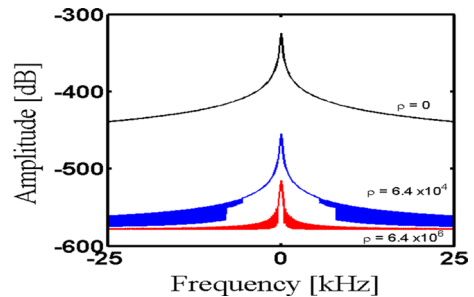
5 Conclusion

In this work, we have mainly focused on the frequency characterization of the cubic-nonlinear optoelectronic oscillator (CN-OEO). The effects of two main parameters have been investigated: the high cut-off time through the coil L and the cubic-nonlinear term ρ. It has appeared that these terms affect the system from the dynamical and spectral points of view.

First, when the value of the coil has been fixed at 10 μH (wideband CN-OEO), the results have shown that the presence and the increase of the cubic-nonlinear term do not affect the threshold value of the effective normalized gain (always equal to 1), but chaotic dynamics occurs at earlier values of the effective normalized gain when the nonlinear parameter increases ($|\gamma| = 2.5$, $|\gamma| = 2.35$, and $|\gamma| = 2.15$ for $\rho = 0$, $\rho = 6.4 \times 10^4$, and $\rho = 6.4 \times 10^6$, respectively). The bifurcation diagram has also shown that the dynamics of the CN-OEO is essentially dominated by limit-cycle oscillations and chaotic states. Also, we have observed a very large increase in the fundamental frequency (300 kHz for $\rho = 0$, 2.1 MHz for $\rho = 6.4 \times 10^4$, and 5.8 MHz for $\rho = 6.4 \times 10^6$ when $\gamma = 1.05$ for the three cases) and the increase of the cubic-nonlinear term reduces the number of admitted oscillation modes in the system. Same for this case, the presence of the cubic-nonlinear term makes the CN-OEO like a high (in the range of MHz) frequency combs generator with a free spectral range equal to 303 kHz corresponding to the value of the inverse of the time-delay $1/T_D$.

Secondly, when the value of the coil has been increased and fixed at 10 *mH* (narrowband CN-OEO), it was observed that the cubic-nonlinear term, however, influences the threshold value of the effective normalized gain (1 for $\rho = 0$, 3.36 for $\rho = 6.4 \times 10^4$, and 1.3 for $\rho = 6.4 \times 10^6$). Then, from the dynamical point of view, chaotic dynamics occurs a little far ($|\gamma| = 5.85$ for $\rho = 0$, $|\gamma| = 9.2$ for $\rho = 6.4 \times 10^4$, and $|\gamma| = 12.3$ for $\rho = 6.4 \times 10^6$). In this case ($L = 10$ mH), we have also noted an increase in the fundamental frequency for the values of the effective normalized gain taken just above each threshold (9.5 kHz for $\rho = 0$ when $|\gamma| = 1.05$, 245 kHz for $\rho = 6.4 \times 10^4$ when $|\gamma| = 3.45$, and 265 kHz for $\rho = 6.4 \times 10^6$ when $\gamma = 1.5$).

Further research investigations will be devoted to the exploration of the phase noise in high-frequency CN-OEO with potential applications in radar (Xu et al. 2019, 2017).

Declarations

References

Argyris, A., Syvridis, D., Larger, L., Annovazzi-Lodi, V., Colet, P., Fischer, I., Jordi, G.-O., Mirasso, C.R., Pesquera, L., Share, K.A.: Chaos-based communications at high bit rates using commercial fibre-optic links. Nature. **438**, 343–346 (2005)

Barmuta, P., Ribeiro, D., Wang, K., Avolio, G., Rajabi, M., Lewandowski, A., Gibiino, G.P., Szatkowski, J., Schreurs, D., Hale, P., Remley, K., Williams, D.: Comparing LSNA calibration: large-signal network analyzer round robin. IEEE Microw. Mag. **17**, 59–64 (2016)

Chan, S.C., Xia, G.Q., Liu, J.M.: Optical generation of a precise microwave frequency comb by harmonic frequency locking. Opt. Lett. **32**, 1917–1919 (2007)

Chembo, Y.K.: Kerr optical frequency combs: theory, applications and perspectives. Nanophotonics **5**, 214–230 (2016)

Chembo, Y.K., Colet, P., Larger, L., Gastaud, N.: Chaotic breathers in delayed electro-optical systems. Phys. Rev. Lett. **95**, 1–4 (2005)

Chembo, Y.K., Larger, L., Tavernier, H., Bendoula, R., Rubiola, E., Colet, P.: Dynamic instabilities of microwaves generated with optoelectronic oscillators. Opt. Lett. **32**, 2571–2573 (2007)

Chembo, Y.K., Larger, L., Colet, P.: Nonlinear dynamics and spectral stability of optoelectronic microwave oscillators. IEEE J. Quantum Electron. **44**, 858–866 (2008)

Chembo, Y.K., Brunner, P., Jacquot, M., Larger, L.: Optoelectronic oscillators with time-delayed feedback. Rev. Mod. Phys. **91**, 1–51 (2019)

Cheng, Y., Yan, J., Zhao, S.: 20-GHz Self-oscillating parametric optical frequency comb generation using an electroabsorption modulated laser-based optoelectronic oscillator. IEEE Photon. J. **14**, 417–421 (2020)

Chengui, G.R.G., Talla, A.F., Talla Mbé, J.H., Coillet, A., Saleh, K., Larger, L., Woafo, P., Chembo, Y.K.: Theoretical and experimental study of slow-scale Hopf limit-cycles in laser-based wideband optoelectronic oscillators. J. Opt. Soc. Am. B **31**, 2310–2316 (2014)

Cho, C., Koo, H., Kwon, J.Y., Lee, J.G.: Phase calibration and uncertainty evaluation for RF comb generator. Control **53**, 698–703 (2020)

Coddington, I., Newbury, N., Wann, W.: Dual-comb spectroscopy. Optica **3**, 414–426 (2016)

Emeux, T.: Applied Delay Differential Equations. Springer, Berlin (2009)

Ge, Z.-M., Hsiao, C.-L., Chen, Y.-S.: Nonlinear dynamics and chaos control for a time delay Duffing system. Int. J. Nonlinear Sci. Num. **6**, 187–199 (2005)

Gill, G.S., Chiang, H.F., Hall, J.: Waveform synthesis for ultra wideband radar. In: Proceedings of 1994 IEEE National Radar Conference, pp. 240–245, (1994)

Hale, P.D., Williams, D.F., Dienstfrey, A.: Waveform metrology: signal measurements in a modulated world. Metrologia **55**, S135–S151 (2018)

Hargrove, L.E., Fork, R.L., Pollack, M.A.: Locking of He–Ne laser modes induced by synchronous intracavity modulation. Appl. Phys. Lett. **5**, 4–5 (1964)

Huang, C., Zhang, H.: Stability and Hopf bifurcation of a delayed prey–predator model with disease in the predator. Int. J. Bifur. Chaos. **2**(9), 1–23 (2019)

Jia, S., Yu, J., Wang, Z., Wang, J., Wang, W., Chen, B., Yu, Y.: A novel highly stable dual-wavelength short optical pulse source based on a dual-loop optoelectronic oscillator with two wavelengths. IEEE Photon. J. **7**, 1–11 (2015)

Juan, Y.S., Lin, F.Y.: Ultra broadband microwave frequency combs generated by an optical pulse-injected semiconductor laser. Opt. Lett. **17**, 18596–18605 (2009)

Kamaha, J.S.D., Talla Mbe, J.H., Woafo, P.: Routes to chaos and characterization of limit-cycle oscillations in wideband time-delayed optoelectronic oscillators with nonlinear filters. Opt. Soc. Am. **37**, 75–82 (2020)

Kamaha, J.S.D., Talla Mbé, J.H., Noubissie, S., Fotsin, H.B., Woafo, P.: Dynamics of optoelectronic oscillators with band pass filter and laser nonlinearities: theory and experiment. Opt. Quantum Electron. **54**, 1–15 (2022)

Koualong, K.M.T., Talla Mbé, J.H., Tatietse, T.T.: Efficient sensings of temperature, refractive index, and distance measurement using the cubic nonlinear optoelectronic oscillators. Opt. Quantum Electron. **54**, 1–5 (2022)

Kouayep, R.M., Talla, A.F., Talla Mbé, J.H., Woafo, P.: Bursting oscillations in Colpitts oscillator and application in optoelectronics for the generation of complex optical signals. Opt. Quantum Electron. **52**, 1–13 (2020)

Lakshmanan, M., Senthilkumar, D.V.: Dynamics of Nonlinear Time-Delay Systems. Springer, Berlin (2011)

Larger, L., Soriano, M.C., Brunner, D., Appeltant, L., Gutierrez, J.M., Pesquera, L., Mirasso, C.R., Fischer, I.: Photonic information processing beyond Turing: An optoelectronic implementation of reservoir computing. Opt. Express **20**, 3241–3249 (2012)

Larger, L., Penkovsky, B., Maistrenko, Y.: Virtual chimera states for delayed feedback systems. Phys. Rev. Lett. **111**, 1–5 (2013)

Lasri, J., Bilenca, A., Dahan, D., Sidorov, V., Eisenstein, G., Ritter, D., Yvind, K.: A self-starting hybrid optoelectronic oscillator generating ultra low jitter 10-GHz optical pulses and low phase noise electrical signals. IEEE Photon. Technol. Lett. **14**, 1004–1006 (2002)

Li, T.-H.S., Tsai, S.-H., Hsia, M.-Y.: Robust H-infinity fuzzy control for a class of time-delay fuzzy bilinear systems with an additive disturbance. Int. J. Nonlinear Sci. Num. **3**, 315–322 (2009)

Maleki, L.: The optoelectronic oscillator. Nature Photon. **57**, 28–30 (2011)

Martinenghi, R., Rybalko, S., Jacquot, M., Chembo, Y.K., Larger, L.: Photonic nonlinear transient computing with multiple-delay wavelength dynamics. Phys. Rev. Lett. **108**, 1–4 (2012)

Neyer, A., Voges, E.: Dynamics of electrooptic bistable devices with delayed feedback. IEEE J. Quantum Electron. **18**, 2009–2015 (1982)

Saleh, K., Lin, G., Chembo, Y.K.: Effect of laser coupling and active stabilization on the phase noise performance of optoelectronic microwave oscillators based on whispering-gallery-mode resonators. IEEE Photon. J. **7**, 1–11 (2014)

Savchenkov, A.A., Motsko, A.B., Maleki, L.: On frequency combs in monolithic resonators. Nanophotonics **5**, 363–391 (2016)

Sciamanna, M., Shore, K.A.: Physics and applications of laser diode chaos. Nat. Photonics **9**, 151–162 (2015)

Talla Mbé, J.H., Talla, A.F., Chengui, G.R.G., Coillet, A., Larger, L., Woafo, P., Chembo, Y.K.: Mixed-mode oscillations in slow-fast delayed optoelectronic systems. Phys. Rev. E **91**, 1–6 (2015)

Talla Mbé, J.H., Kamaha, J.S.D., Woafo, P., Chembo, Y.K.: Dynamics of wideband time-delayed optoelectronic oscillators with nonlinear filters. IEEE J. Quantum Electron. **55**, 1–6 (2019)

Talla Mbe, J.H., Atchoffo, W.N., Tchitnga, R., Woafo, P.: Dynamics of time-delayed optoelectronic oscillators with nonlinear amplifiers and its potential application to random numbers generation. IEEE J. Quantum Electron. **57**, 1–7 (2021)

Talla, A.F., Martinenghi, R., Woafo, P., Chembo, Y.K.: Breather and pulse-package dynamics in multinonlinear electrooptical systems with delayed feedback. IEEE Photon. J. **8**, 1–8 (2016)

Uchida, A.: Optical Communication with Chaotic Lasers: Applications of Nonlinear Dynamics and Synchronization. Wiley, New York (2012)

Udem, Th., Holzwarth, R., Hansch, T.W.: Optical frequency metrology. Nature **416**, 233–237 (2002)

Vallée, R., Delisle, C.: Periodicity windows in a dynmical system with a delayed feedback. Phys. Rev. A **34**, 309–318 (1986)

Wang, Z., Wang, X., Li, Y., Huang, X.: Stability and Hopf bifurcation of fractional-order complex-valued single neuron model with time delay. Int. J. Bifur. Chaos. **2**(7), 1–13 (2017)

Weicker, L., Erneux, T., Otti, D., Danckaert, J., Jacquot, M., Chembo, Y.K., Larger, L.: Slow-fast dynamics of a time-delayed electro-optic oscillator. Phil. Trans. R. Soc. A **371**, 1–14 (2013)

Xu, H., Li, Y., Zhang, J., Han, H., Bing, Z., Wang, L., Wang, Y., Wang, A.: Ultra-wideband chaos life-detection radar with sinusoidal wave modulation. Int. J. Bifur. Chaos **27**, 1–12 (2017)

Xu, Y., Peng, H., Guo, R., Du, H., Yin, Q., Hu, G., He, J., Chen, Z.: Injection-locked millimeter wave frequency divider utilizing optoelectronic oscillator based optical frequency Comb. IEEE Photon. J. **11**, 1–9 (2019)

Xu, H., Li, L., Li, Y., Zhang, J., Han, H., Liu, L., Li, J.: Chaos-based through-wall life-detection radar. Int. J. Bifur. Chaos **29**, 1–12 (2019)

Yao, J.: Optoelectronic oscillators for high speed and high resolution optical sensing. J. Lightw. Technol. **35**, 3489–3497 (2017)

Yao, X.S., Maleki, L.: Optoelectronic microwave oscillator. J. Opt. Soc. Am. B Opt. Phys. **13**, 725–1735 (1996)

Yokoyama, S., Nakamura, R., Nose, M., Araki, T., Yasui, T.: Terahertz spectrum analyzer based on a terahertz frequency comb. Opt. Express **16**, 13052–13061 (2008)

Zhang, Y., Hou, D., Zhao, J.: Long-term frequency stabilization of an optoelectronic oscillator using phase-locked loop. IEEE J. Lightw. Technol. **32**, 2408–2414 (2014)

Zhang, L., Pan, B., Chen, G., Guo, L., Lu, D., Zhao, L., Wang, W.: 640-Gbit/s fast physical random number generation using a broadband chaotic semiconductor laser. Sci. Rep. **7**, 1–8 (2017)

Zhao, M.R., Wu, Z.M., Deng, T., Zhou, L., Xia, G.Q.: Tunable and broadband microwave frequency combs based on a semiconductor laser with incoherent optical feedback. Chin. Phys. B **24**, 1–6 (2015)

Zou, X., Liu, X., Li, W., Li, P., Pan, W., Yan, L., Shao, L.: OptoElectronic Oscillators (OEOs) to sensing, measurement, and detection. IEEE J. Quantum Electron. **52**, 1–16 (2016)